이학박사학위논문

Study of Quasi-Elastic Scattering on Nuclei: Experimental Verification of the Coulomb Sum Rule

핵의 준탄성 충돌에 대한 연구
-쿨롱 합 법칙의 실험적 검증-

2013년 2월

서울대학교 대학원

물리천문학부

오 유 민

Study of Quasi-Elastic Scattering on Nuclei: Experimental Verification of the Coulomb Sum Rule

by
Yoomin Oh

Supervised by
Seonho Choi

A Dissertation Submitted to the Faculty of
Seoul National University
in Partial Fulfillment of the Requirements for
the Degree of Doctor of Philosophy

February 2013

Department of Physics and Astronomy
Graduate School
Seoul National University

Abstract

Study of Quasi-Elastic Scattering on Nuclei: Experimental Verification of the Coulomb Sum Rule

Yoomin Oh
Physics Department
The Graduate School
Seoul National University

Inclusive electron scattering cross section data from Jefferson Lab Coulomb Sum Rule experiment have been analyzed. The measurement was performed at four scattering angles of 15, 60, 90 and 120 degrees and with various incident energies ranging 0.4 to 4 GeV. The three momentum transfer range covers 0.55 to 0.95 GeV/c, which has never been explored in the previous experiments. A Rosenbluth separation at constant three momentum transfer was performed to verify the Coulomb Sum Rule, by which the medium modification of the nucleon form factor inside the nucleus can be tested. Coulomb distortion effect was corrected using Effective Momentum Approximation. Results of ^{12}C and ^{56}Fe data are presented with detailed analysis procedure. Comparison with existing data was performed at low momentum transfers. The possible "quenching" of the Coulomb Sum was found at the lowest 3-momentum transfers. However, the Coulomb Sum at higher momentum transfer shows interesting features which requires further study.

Keywords : Quasi-elastic scattering, Rosenbluth separation, Response functions, Coulomb Sum Rule, Jefferson Lab
Student number : 2007-30114

Contents

List of Figures

List of Tables

Chapter 1

INTRODUCTION

The question of the possible medium modifications of the nucleon form factor inside the nucleus is of great interest in nuclear physics and yet still unresolved [1]. One of the most intuitive method to investigate the properties of nucleons inside nuclei is quasi-elastic electron scattering off nuclei. Since the charge and magnetic responses of a single nucleon are quite well studied from elastic scattering experiments, measuring the same response from quasi-elastic scattering off nuclei and comparing with a single nucleon are likely to shed a light on the question. Especially, a Rosenbluth separation of the charge and magnetic responses of a nucleus can be used to test the Coulomb Sum Rule (CSR). This sum rule states that the integration of the charge reponse of a nucleus over the full range of energy loss ($\omega = E - E'$) should be equal to the total charge of the nucleus. However, this simple picture becomes more complicated due to various effects inside nucleus. First of all, at very small momentum transfer ($|\mathbf{q}|$), considering only Pauli blocking on a system of freely moving nucleons will produce a quenching of the CSR, leading it not to reach the full value of Z. As the momentum transfer increases, the long range correlations and then the short range correlations between nucleons play similar role. However, at sufficiently high momentum transfer, only shoft range correlation effects remain. They have been estimated by various theoretical calculations using different $N - N$ forces and found to be responsible for at most 10% quenching of the CSR integral. As a result, any further quenching of this quantity at sufficiently high momentum transfer may indicate the possibility of modified properties of the nucleon inside the nucleus.

Starting from this quite simple idea, for the past several decades, various laboratories in the world performed experiments in diverse conditions, but

the final conclusion is still controversial. The limitations on the past accelerators made the kinematic conditions not so favorable to test the CSR. For example, the kinematic coverage in $|\mathbf{q}|$ and ω or the lever arm for Rosenbluth separation has been somewhat limited. However, these previous experiments have raised issues, such as controlling systematic errors, to be considered for a better test and also provided valuable experience on how to address them.

To test the CSR in the sufficiently large momentum transfer range, a new experiment was performed at the experimental Hall A in Jefferson Lab from October 2007 to January 2008. The experiment has covered the momentum transfer range from 550 MeV/c to 950 MeV/c where no previous experiments have reached. Helium-4, carbon-12, iron-56, and Pb-208 were used as target nuclei to varify the medium effect on nuclear responses.

In this chapter, electron-nuclues scattering process and nuclear response will be briefly introduced, and the existing data from various experiments will be reviewed.

1.1 Electron-Nucleus Scattering and Nuclear Response

Let us consider an election with incident energy E is scattered by a nucleus target at rest in the laboratory frame (Fig.1.1a). A single virtual photon is assumed to be exchanged, with energy-momentum transfer $q(\omega = E - E',\ \mathbf{q})$. And the electron is detected in the direction of scattering angle θ with energy E'. A review of Benhar *et al* [2] is a good reference describing this inclusive electron-nucleus scattering. The following is quoted from the reference:

At low energy loss(ω), peaks due to elastic scattering and inelastic excitation of discrete nuclear states appears (see Fig.1.2)*; a measurement of the correspoinding form factors as a function of momentum transfer $|\mathbf{q}|$ gives access to the form factors. At larger energy loss, a broad peak due to quasi-elastic electron-nucleon scattering appears; this peak–very wide due to nuclear Fermi motion–corresponds to processes by which the electron scatters from an individual, moving nucleon, which, after interaction with other nucleons, is ejected from the target. At even larger ω, peaks that correspond to excitation of the nucleon to distinct resonances are visible. At very large ω, a structureless continuum due to deep inelastic scattering (DIS) on quarks bound in nucleons appears. At momentum transfers above approximately 500 MeV/c, the dominant feature of the spectrum is the quasielastic peak.*

A number of questions have been investigated using quasi elastic scatter-

ing:

- *The quasi-elastic cross section intergrated over electon energy loss is proportional to the sum of electron-nucleon cross sections. Historically, this has been exploited in order to measure the neutron charge and magnetic form factors using mainly light($A < 4$) nuclear targets.* ***Today the emphasis has shifted to exposing possible medium modifications of the nucleon form factors.***

- *Another integral property of the quasielastic peak, its width, provides a direct measure of the average momentum of nucleons in nuclei, and has been used to determine nuclear fermi momenta; contrary to other observables such as densities, quasielastic scattering provides a* ***direct*** *determination via an observable sensitive to the momenta of nucleons.*

- *The* ***shape*** *of the quasielastic peak depends on the distribution in energy E and momentum $\mathbf{k}$ of the initially bound nucleons. Precise measurements give indirect access to (integrated properties of) the nuclear spectral function $S(\mathbf{k}, E)$ describing this distribution. In particular, the tail of the quasielastic peak at large $|\mathbf{q}|$ and low ω is sensitive to the tail of the spectral function at large $|\mathbf{k}|$.*

- *Processes more complicated than one-nucleon knockout, in particular those related to non-nucleonic degrees of freedom and meson exchange currents (MEC), also play a role. They can be investigated by separating the quasielastic response into the longitudinal (charge) and transverse (magnetic plus convection) pieces, the latter being preferentially affected by MEC.*

- ***Scaling*** *is one of the unique features of quasielastic scattering. This refers to the fact that the inclusive cross section, which* ***a priori*** *is a function of two independent variables $|\mathbf{q}|$ and ω, depends on a single variable $y(q, \omega)$. This scaling property, a consequence of the kinematics of the underlying electron-nucleon elastic scattering process, provides a strong handle on the reaction mechanism. Further, the scaling violations that are observed reveal how the dynamics go beyond the impulse approximation (IA) picture of quasielastic scattering.* $\cdots$

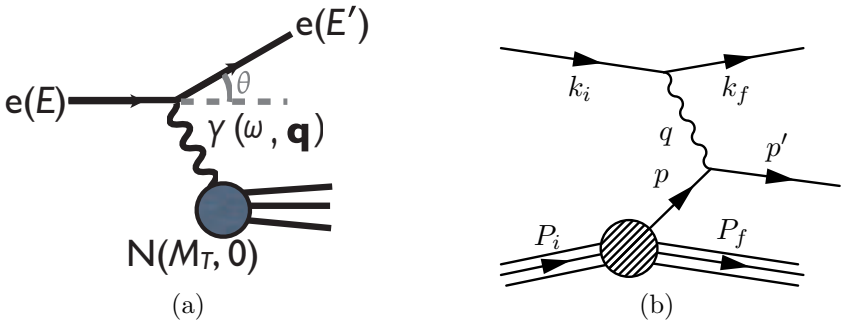

(a) (b)

Figure 1.1: (a) Illustration of electron-nucleus scattering process, (b) Diagram for quasi-elastic scattering in the plane wave impulse approximation.

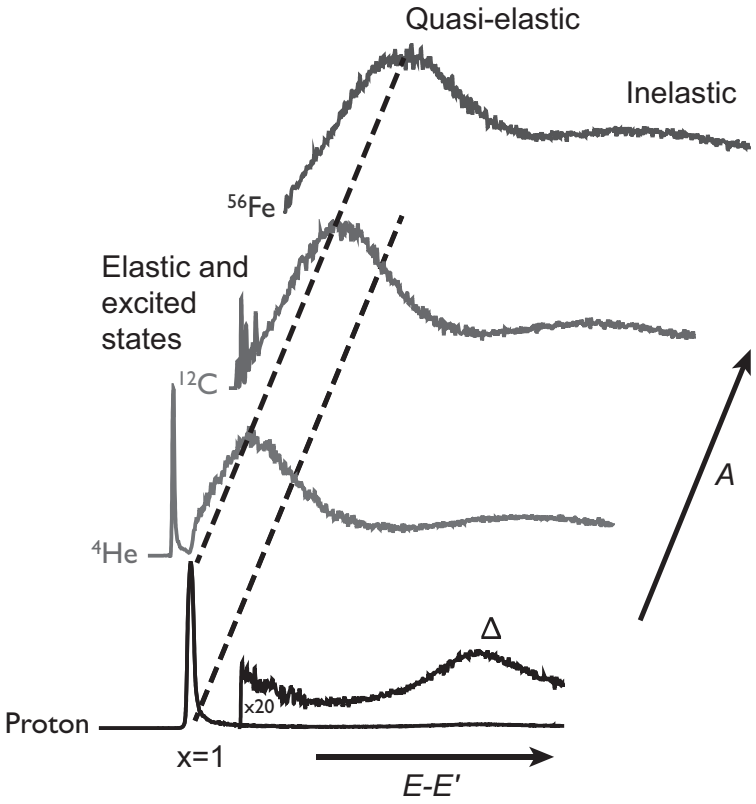

Figure 1.2: Nuclear responses to electron scattering, taken from $E = 1646$ MeV, θ=15° data. Description is in the text.

Figure 1.2 shows the shapes of differential cross sections($d\sigma/d\Omega d\omega$) of various nucleus used in this experiment. Several peaks corresponding to the inelastic nuclear excited states can be observed in the low energy loss region. The broad quasi-elastic peaks are observed at $x \sim 1 = -q^2/2M\omega$ (M is the nucleon mass), where the sharp electron-proton elastic scattering peak is located. And it is observed that the width of the quasielastic peak gets larger as nuclear mass A grows.

Rosenbluth formula and Coulomb Sum Rule

The differential cross section of the inclusive unpolarized electron scattering described above can be written as:

$$\sigma \equiv \frac{d\sigma}{d\Omega d\omega} = \sigma_{\rm M} \left[\frac{Q^4}{\mathbf{q}^4} R_L(|\mathbf{q}|, \omega) + \frac{Q^2}{2\mathbf{q}^2} \frac{R_T(|\mathbf{q}|, \omega)}{\varepsilon} \right], \tag{1.1}$$

where

$$\varepsilon(|\mathbf{q}|, \omega, \theta) = \left[1 + \frac{2\mathbf{q}^2}{Q^2} \tan^2 \frac{\theta}{2} \right]^{-1} \tag{1.2}$$

is the polarization parameter of the exchanged virtual photon,

$$\sigma_{\rm M} = \frac{4\alpha^2 E'^2 \cos^2(\theta/2)}{Q^4} \tag{1.3}$$

is the Mott cross section, $Q^2 = -q^2 = \mathbf{q}^2 - \omega^2$ gives four-momentum squared of the exchanged virtual photon, and $R(|\mathbf{q}|, \omega, \theta)$ $(= \sigma/\sigma_M)$ is the total response function in the square bracket.* A brief derivation of this Rosenbluth formula is provided in Appendix.

Experimentally, longitudinal (R_L) and transverse (R_T) response functions can be separated by measuring the cross sections at a fixed point in (ω, $|\mathbf{q}|$) plane at two or more angles. Then a plot of εR versus ε should lie on a straight line; the slope of this line is $(Q^4/\mathbf{q}^4)R_L$ and its intercept is $(Q^2/2\mathbf{q}^2)R_T$ (see Eq. 4.2).

After the Rosenbluth separation, a model-independent property known as Coulomb Sum Rule (CSR) can be tested by integrating R_L over the full range of ω at constant $|\mathbf{q}|$:

$$S_L(|\mathbf{q}|) = \frac{1}{Z} \int_{0+}^{\infty} \frac{R_L(|\mathbf{q}|, \omega)}{[(G_E^p + N/ZG_E^n)\zeta]^2} d\omega. \tag{1.4}$$

*In this thesis, σ usually means the double differential cross section ($d\sigma/d\Omega d\omega$), but sometimes it may refer to $d\sigma/d\Omega$, and so does the term "cross section".

Here, G_E^p and G_E^n are free nucleon (proton, neutron) electric form factors, ζ is a relativistic correction suggested by de Forest [3], and the lower integral limit 0^+ is the threshold for particle emission. In the limit of large momentum transfer ($|\mathbf{q}| \gg k_f$; k_f is the fermi momentum of the nucleus), CSR predicts S_L should be 1. In other words, when neglecting the small contribution from the neutron charge form factor G_E^n, the integral over the longitudinal reponse counts the number of protons times the square of the proton charge form factor G_E^p. However, existing experimental results (in the following section) in low $|\mathbf{q}|$ range show a quenching of CSR from 1 for heavy nuclei, which may indicates the possible medium modification of the nucleon form factors.

Coulomb correction

The idea of the Rosenbluth separation of the longitudinal and transverse response functions is based on the Plane Wave Born Approximation (PWBA) and one photon exchange. While the picture is valid for scattering of electrons off a nucleon, for scattering off a nucleus, this simple description becomes complicated due to the effect of the Coulomb field of the nucleus. In a large Z nucleus, the strong Coulomb filed induces a distortion of the wave front which modifies the structure of the (e, e') cross section and induces sizable effects in the longitudinal/transverse separation of the electromagnetic responses [4].

The effect of the Coulomb field on the cross section can be calculated using the Distorted Wave Born Approximation (DWBA). However, DWBA cross section cannot be written in a separable form, and the involved numerical complications are extremely time consuming. Due to these obstacles, approximate methods have been developed, and the Effective Momentum Approximation (EMA) is one of them used in this work[†].

In EMA, the momentum of the electron before and after the scattering is corrected using the mean value of the Coulomb potential of the nucleus:

$$E \to E - \overline{V}_{\rm C},\ E' \to E' - \overline{V}_{\rm C}. \tag{1.5}$$

Then the effective 3 momentum transfer can be written

$$\mathbf{q}_{\rm eff} = \mathbf{q} + \left(\hat{\mathbf{k}}_i - \hat{\mathbf{k}}_f\right)\overline{V}_{\rm C} = \mathbf{q}\left(1 - \frac{\overline{V}_{\rm C}}{E}\right) + \frac{\omega}{E}\overline{V}_{\rm C}\hat{\mathbf{k}}_f, \tag{1.6}$$

[†]Detailed discussion on Coulomb correction can be found in Ref. [1, 4] and references therein.

where $\hat{\mathbf{k}}_i$ ($\hat{\mathbf{k}}_f$) is the unit vector in the direction of the incident (scattered) electron.

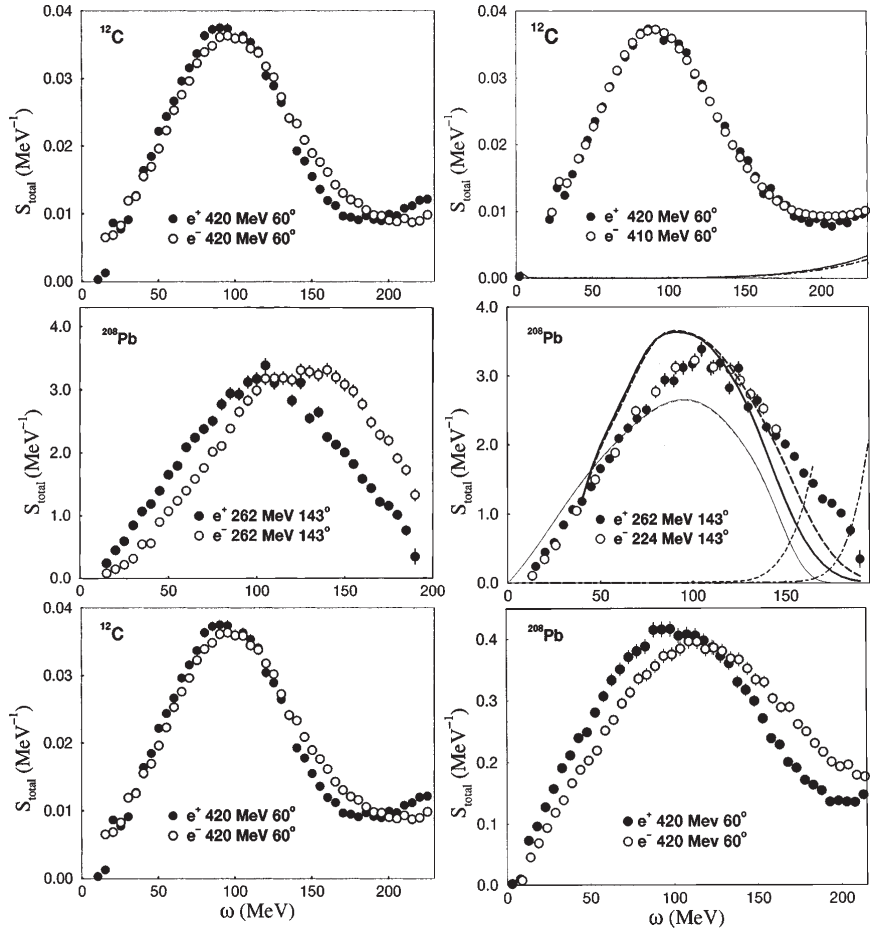

Figure 1.3: Total responses of electron (open circle) and positron (filled circle) quasi-elastic scattering off of ^{12}C (top) and of ^{208}Pb (middle and bottom) [5]. The quasi-elastic peaks are do not match for electron and positron with the same incident energy (left). When the incident energy of the electron is reduced by twice of the effective Coulomb potential of the nucleus, the peaks are aligned on top of each other (right).

The validity of EMA was tested experimentally by Gueye *et al* [5] (Figure 1.3). In their observation, the quasi-elastic peaks of the electron and of the positron did not match when incident energies were same. When the incident electron energy was reduced by twice of the effective Coulomb potential of

the nucleus ($V_C = 5$ MeV for ^{12}C, 19 MeV for ^{208}Pb), it was observed that the peaks were aligned on top of each other.

The application of Coulomb correction with EMA results in slight change of a measured kinematic point (ω, $|\mathbf{q}|$) to the effective kinematic point (ω, $|\mathbf{q}_{\text{eff}}|$). The size of correction depends on Z of the target nucleus, on the incident and scattered energy, and on the scattering angle as in Eq. 1.6. A small difference in change of the data points at diffrent scattering angles lead to a different result in R_L/R_T separation, and a significant change (suppression) of Coulomb Sum.

1.2 Existing Data

Longitudinal and transverse response functions

Figures 1.4 and 1.5 show the existing data of the longitudinal and transverse response functions of ^{40}Ca, ^{48}Ca, and ^{56}Fe at $|\mathbf{q}| = 410$ and 550 MeV/c [6]. One can see that the transverse response functions have not only the quasi-elastic contribution but also the contribution from inelastic process, and that they are fairly well reproduced by theories which take into account the contributions such as meson exchange current (MEC), particle-hole correlations and pion production. However, for the longitudinal part, where the main contribution is from quasi-elastic process, the experimental data show quenching of R_L from the simple relativistic Fermi gas (SRFG) model prediction, while the model predicts the total response function fairly well. The agreement becomes better when the final-state interaction (FSI) or the nuclear density effect is taken into account.

However, the data shown in Figures 1.4 and 1.5 was produced without considering the effect of Coulomb distortion. After the correction, the integrated R_L would quench more from the theories, while R_T is little affected.

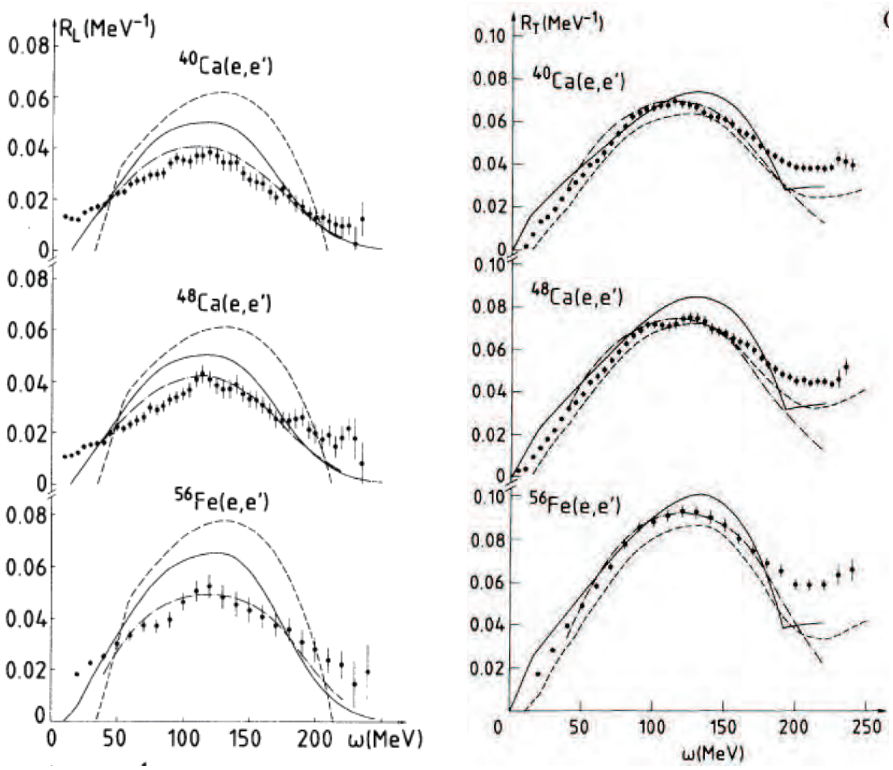

(a) (b)

Figure 1.4: (a) R_L and (b) R_T of ^{40}Ca, ^{48}Ca, and ^{56}Fe at $|\mathbf{q}| = 410$ MeV/c [6]. (a) The dashed line is a Fermi-gas caculation by Van Orden; the solid line, a shell model calculation by Laget; and the dot deshed line a calculation by Do Dang. (b) The dashed line is the total contribution from calculation by Laget. The dot-dashed line is the Do Dang and Va Giai calculation containing only the quasi-elastic process. The solid line is the random-phase approximation (RPA) calculation with 1p-1h and 2p-2h excitations by Alberico, Ericson, and Molinari.

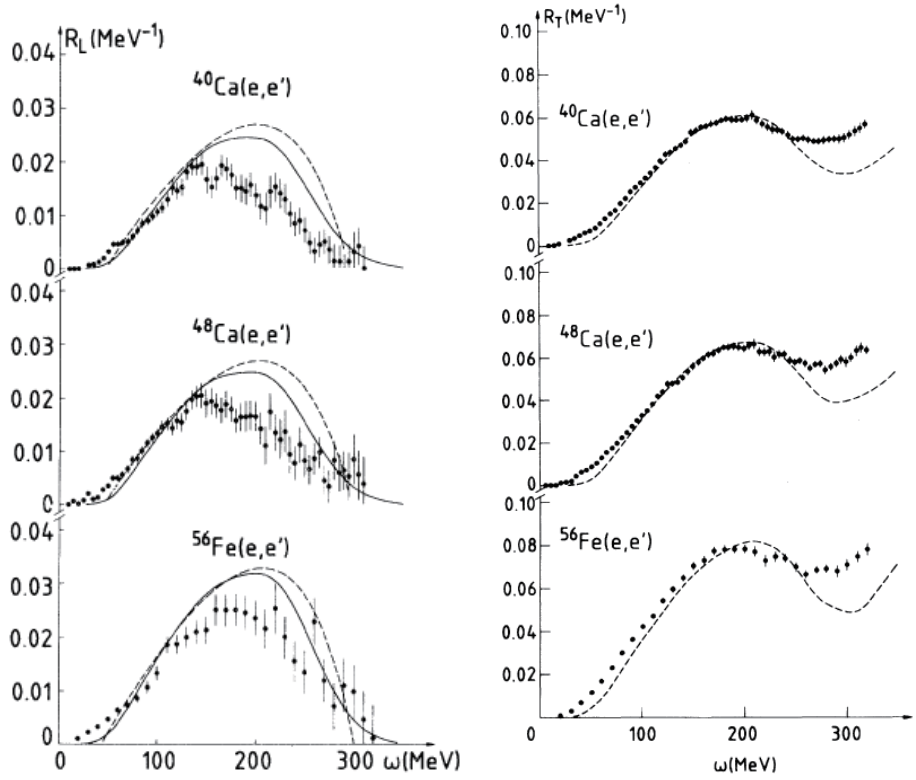

(a) (b)

Figure 1.5: (a) R_L and (b) R_T of ^{40}Ca, ^{48}Ca, and ^{56}Fe at $|\mathbf{q}| = 550$ MeV/c [6]. Description of curves are same as in Figure 1.4.

Coulomb Sum Rule

Figure 1.6 [7] shows the existing data of Coulomb Sum (S_L), considering Coulomb distortion using EMA method. S_L of ^{3}He, the lightest nucleus among them, is in a good agreement with, or a little excess from the theoretical prediction. S_L of the other heavier nuclei lie below the prediction which does not consider in-medium modification (long dashed curves). Data for these heavier nuclei target is better described when the prediction includes modified form factors (dot-dashed curves).

It should be pointed out that most data points are at below $|\mathbf{q}_{\rm eff}|$=600 MeV/c, where the quasi-elastic process is suppressed by Pauli blocking. Only one point from ^{56}Fe SLAC NE9 data is at $|\mathbf{q}_{\rm eff}|$=1.14 GeV/c but it has too large error bar to verify the Coulomb Sum Rule.

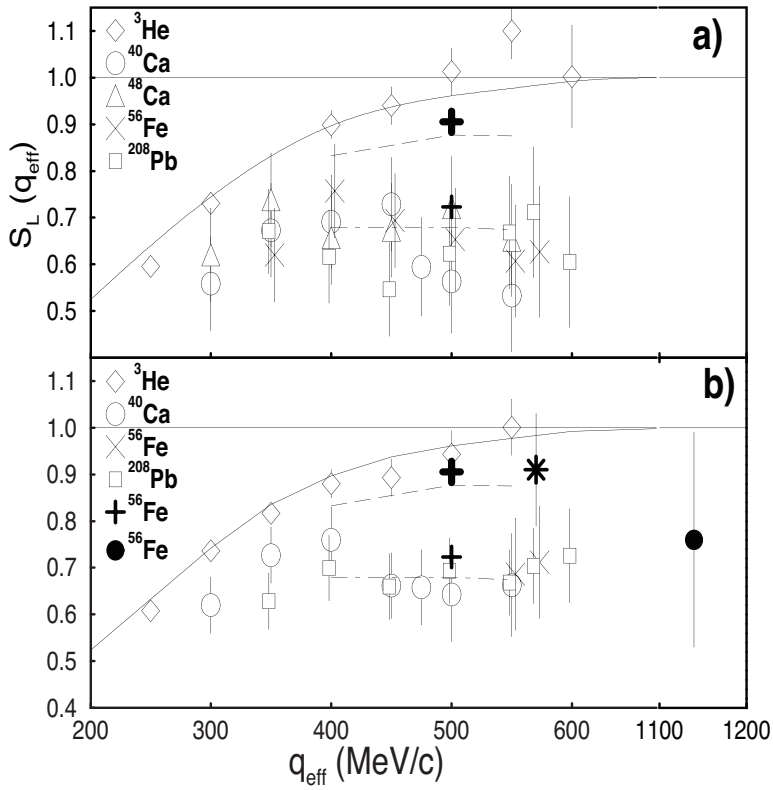

Figure 1.6: Existing data of Coulomb Sum [7]. (a) Saclay only, (b) Saclay+SLAC NE3+Bates. Solid line represents the microscopic Nuclear Matter (NM) calculations; dashed line, same calculation within the experimental limits; dot-dashed line, same with modified form factors; thick right cross, ^{208}Pb Hartree-Fock (HF) calcultions within the the experimental limit, and thin right cross, same with modified form factors. Thick star in (b) represents Jourdan analysis of Saclay data. Note that there is a jump between 600 and 1100 MeV/c in x-axis.

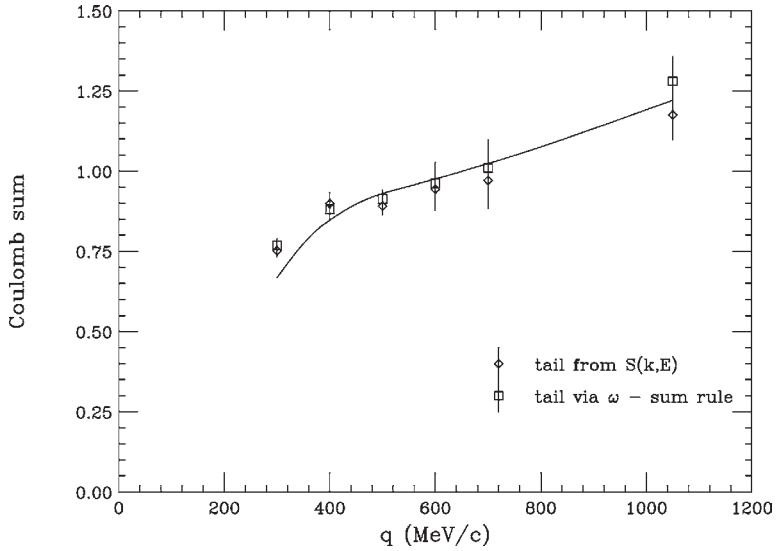

Figure 1.7: Coulomb Sum of ^{4}He from Ref. [8]. The calculation (solid curve) includes the contribution of two-body charge operators.

A recent analysis result of ^{4}He world data by Carlson *et al* [8] is shown in Figure 1.7. ^{4}He data cover a little bit wider range than the others: 300 MeV/c $\leq$ $|\mathbf{q}|$ $\leq$640 MeV/c, and $\mathbf{q}$ = 1050 MeV/c. The Coulomb distortion was neglected in their analysis because it is small for ^{4}He. Their prediction of Coulomb Sum is different from the one in the previous figure; S_L grows with $|\mathbf{q}$ at all range. They reported that MEC contribution is negative at low $|\mathbf{q}|$, but it grows up and contribute more than 10% at around 1 GeV/c. Therefore, the Coulomb Sum may not remain constant at 1 event for $|\mathbf{q}| \gg 2k_f|$, but grows with $|\mathbf{q}|$.

Not any of the existing data cover the $|\mathbf{q}|$ or $|\mathbf{q}_{\rm eff}|$ range from 600 to 1000 MeV/c continuously, where the Coulomb Sum Rule can be tested without the influence of Pauli blocking. And mixing of world data may raise a question on the treatment of systematics. Furthurmore, the existing data have larger error bars as $|\mathbf{q}_{\rm eff}|$ grows, because the R_L/R_T separation becomes more difficult.

1.3 JLab CSR Experiment

In order to verify the Coulomb Sum Rule in the previously undiscovered $|\mathbf{q}|$ range with minizing the uncertainty, a new CSR experiment was proposed and performed in the experimental Hall A at Jefferson Laboratory (JLab).

JLab E05-110 CSR experiment took place from October 2007 to January 2008. The experimental data cover the three momentum transfer range from 550 MeV/c to 950 GeV/c using 0.4-4 GeV incident electron energy beam and detecting the scattered electrons at 4 angles (15, 60, 90 and 120) degrees. The systematic uncertainties was minimized by the largest lever arm ($\Delta\varepsilon$) between 15 and 120 degrees with supplement of two more angles in a single experiment. ^{4}He, ^{12}C, ^{56}Fe and ^{208}Pb were used as target nuclei to see the nuclear medium effect. Background were controlled with a newly installed NaI shower detector with better resolution.

In this thesis, the analysis procedure and result of ^{12}C data will be presented with the preliminary results of ^{56}Fe and ^{4}He data.

In Chapter 2, the experimental facility and setup will be described. The analysis procedure will be discussed in detail in Chapter 3 and 4. Chapter 5 will show the result of the analysis. Brief derivation of the Rosenbluth formula is included in Appendix.

Chapter 2

THE EXPERIMENT

In this chapter, the experimental facilities of JLab used for this experiment will be briefly introduced.* And it will be shown how the experiment covers the desired kinematic range.

2.1 The Jefferson Lab Electron Beam

The Continuous Electron Beam Accelerator Facility (CEBAF) of JLab has been designed to investigate the structure of nuclei and hadrons and underlying fundamental interactions in the region below the high-energy "asymtotically free" regime. The schematic layout of CEBAF is shown in Figure 2.1. CEBAF consists of a beam injector, two linacs, and several recycle rings. Electrons are generated from a strained GaAs cathode gun and then accelerated to 45 MeV. The beam is then further accelerated by each linac containing 20 cryomodules with a designa accelerating gradient of up to 7 MeV/m, which has made it possible to accelerate electrons to 5.7 GeV†. The design maximum current is 200 μA, which can be split arbitrarily between interleaved 499 MHz bunch trains. All 3 Halls can simultaneously receive the maximum energy beam. Since Hall B with its CEBAF Large Acceptance Spectometer (CLAS) requires a current as low as 1 nA, a 100 μA beam is delivered to one or both of the Hall A and Hall C.

*Details of the Jefferson Lab experimental Hall A facility is in Ref. [9] and Ref. [10].

†Now, in 2012, it is under 12 GeV upgrade by adding 5 new cryomodules on each linac.

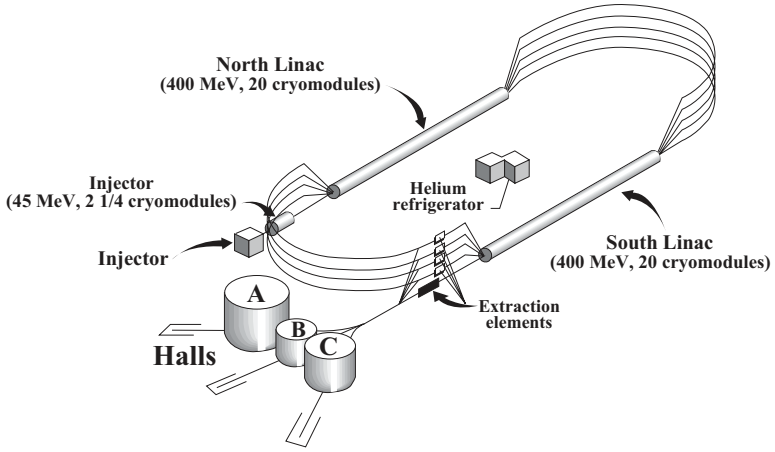

Figure 2.1: Layout of Jefferson Lab CEBAF facility. The electron beam is produced at the injector by illuminating a photocathode and then accelerated to 45 MeV. The beam is then further accelerated in each of two superconducting linacs, through which it can be recirculated up to four times. The beam can be extracted simultaneously to each of the three experimental halls.

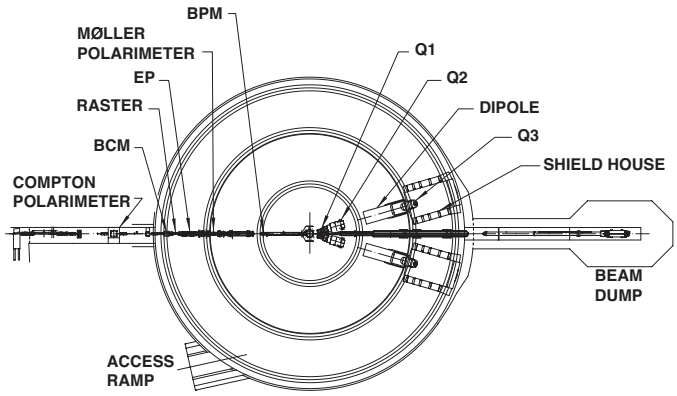

Figure 2.2: Schematic layout of Hall A[9].

2.2 The Experimental Hall A

The basic layout of Halla is shown in Fig. 2.2. The two High Resolution Spectrometers (HRS) provide a momentum resolution of better than 2×10^{-4}

and a horizontal angular resolution of better than 2 mrad at a design maximum central momentum of 4 GeV/c.

2.2.1 Beamline

The instrumentation along the beamline consists of various elements necessaray to transport the electron beam onto the target and into the dump, and to measure simultaneously the relevant properties of the beam.

Beam energy

The energy of the beam is measured absolutely by two independent methods. The arc method (Fig. 2.3) determines the energy by measuring the deflection of the beam in the arc section of the beamline. The nominal bend angle of the in the arc section is 34.3°. The momentum of the beam (p in GeV/c) is then related to the field integral of the eight dipoles ($\int \mathbf{B} \cdot d\mathbf{l}$ in Tm) and the net bend angle through the arc section (θ in radians) by

$$p = k \frac{\int \mathbf{B} \cdot d\mathbf{l}}{\theta} \tag{2.1}$$

where $k = 0.299792$ GeV rad T^{-1} m^{-1}/c. The Arc method consists of two simultaneous measurements. One is for actual bending bending angle of the arc measured by "superharps" wire scanners. The absolute position of superharps is determined by the survey during the experiment. When the beam strikes a wire, the scattering particles are collected by a simple ion chamber, hence a current is generated and the beam position is recorded. There are two superharps at the entrance and exit respectively. The other measurement is for that of the magnetic field integral $\mathbf{B} \cdot d\mathbf{l}$ of the eight dipoles based on a reference magnet (9th dipole) field measurement.

The beam energy can also be determined by the eP method in the hall by measureing the scattered electron angle and the recoil proton angle in the ^{1}H(e,e′p) elastic reaction.

In this experiment, various values of beam energy between 0.4 and 4 GeV were used (summarized in Table 3.1). An Arc measurement was performed with 845 MeV beam energy on 14th of November, 2007, and the resulting energy value was reported as 845.08±0.2 MeV, while the field integral $\mathbf{B} \cdot d\mathbf{l}$ calculation showed 844.87±0.4 MeV[‡]. Since the result is consistent with

[‡] "Tiefenbach" energy (named after JLab accelerator physicist Micheal Tiefenbach) which is calculated from the arc field integral $\mathbf{B} \cdot d\mathbf{l}$, is recorded in the experimental datastream.

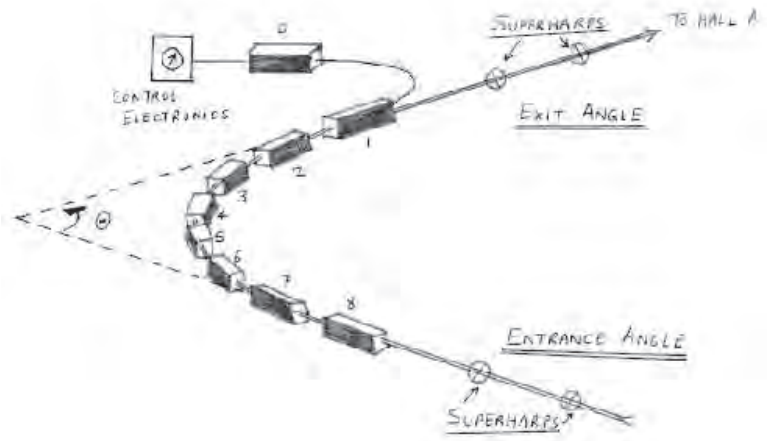

Figure 2.3: Illustration of arc energy measurement [10].

other experiments performed previously, 0.05 % of uncertainty is assigned to the beam energy higher than 0.8 GeV. For the energies below 0.8 GeV, eC and eP elastic scattering data were used to determine the uncertainty (Section 3.1.1).

Beam position and raster

The beam position combined with the other data of an event provides the precise information of the scattering vertex. Beam position and direction are monitored by two Beam Position Monitors (BPMs) which are located 7.524 m and 1.286 m upstream of the target (Fig. 2.2). The absolute position of the beam can be determined from the BPMs by calibrating them with respect to wire scanners (superharps) which are located adjacent to each of BPMs. The position information from the BPMs can be recorded in two different ways:

1. EPICS database records the position averaged over 0.3 s.

2. Event-by-event information is recorded in the main datastream (CODA).

The reliability of the position information is 100 μm (relative), and 200 μm (absolute).

The beam size is quite small ($\sim$100 μm) so that direct use of the beam may cause overheating of target, change in density of a fluid target, or even damaging the target. To avoid these, the beam is spreaded to the order of

several square millimeter size by using the raster. The raster is a pair of horizontal (X) and vertical (Y) air-core dipoles located 23 m upstream of the target. The raster can be used in two different modes: sinusoidal and amplitude modulated. In the sinusoidal parttern both the X and Y magnet pairs are driven with pure sine waves with relative phase, and frequencies which do not produce a closed Lissajous parttern. In the amplitude modulated (or square root of time) mode, both the X and Y producting a circular parttern. The radius of this pattern is changed by amplitude modulation at 1 kHz. The radius modulaton is controlled by a function generator whose function creates a uniform distribution of the area swept out by beam motion. It is not possible to switch on the fly between the two modes of operation as hardware changes are required.

During this experiment, 2×2 mm^2 sinusoidal mode was used for the most of the production runs with average 5-50 μA beam current on all the targets. Some other sizes were also used to study the effect on the fluid target density.

Beam current

At the accelerator injector, the OLO2 (current monitor) and Faraday cup are used to provide an absolute current reference during the calibration procedure. Since different beam current can be requested for different halls, the precise meausrement of beam current is needed in the individual hall. In Hall A, the Beam Current Monitor (BCM) system is located 25 m upstream of the target location. It consists of an Unser monitor, two RF cavities, associated electronics and a data-acquisition system (Figure 2.4).

The two resonant RF cavities on either side of the Unser Monitor monitor the current continuously. The voltage output of these monitors is proportional to the beam current. The output signals from the two cavities is split into two parts (to be sampled or integrated). The sampled data are sent to a digital multimeter which produces a digital signal that represents the RMS of the signal over one second. Signals from both cavities' multimeter and from the multimeter connected to the Unser are transported through GPIB ports to a computer where they are recorded in the EPICS data stream.

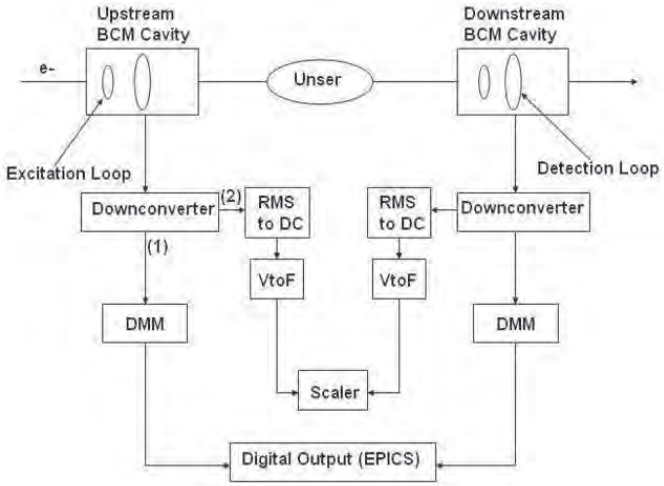

Figure 2.4: Schematic view of the Hall A Beam Current Monitor (BCM) system

For the intergrated data, the other amplifier output is sent to an RMS-to-DC converter, consisting of a 50 kHz bandpass filter to eliminate noise, which produces an analog DC voltage level. This level drives a Voltage-To-Frequency converter whose output frequency is proprotional to the input DC voltage level. The signals are then fed to 200 MHz VME scalers, the output of which is injected into the data stream along with other scaler information. These scaler simply accumulte during the run, resulting in a number which is proprotional to the time-intergrated volated level, and therefore more accurately represents the total beam charge. A set of amplifiers with gain factors of 3 and 10 allow the linear region to lower than 5 μA currents. Hence, there is a set of three signals coming from each BCM. As a result, six scaler outputs (U1, U3, U10, D1, D3, D10; U for upstream, D downstream) prodive the information to determine the charge during a run.

Each of these scaler outputs is calibrated during calibration runs. During this experiment, the beam current for Hall A ranged 5 to 50 μA, and a calibration run for each spectometer was performed at the early stage of the experiment. The procedure and result of the calibration is shown in the next chapter.

2.2.2 Target System

In the CSR experiment, the standard scattering vacuum chamber of Hall A was used. The chamber is constructed out of several rings 1037 mm in diameter, supported on a 607 mm diameter central pivot post. The stainless-steel base rings has one vacuum pump-out port and the other ports for viewing and electrical feed-throughs. The middle ring is made out of aluminum and located at beam height with 152 mm vertical cutouts on each side of the beam oer the full angular range ($12.5^\circ \leq \theta \leq 167.5^\circ$). The cutouts are covered with a pair of flanges with thin (0.38 mm) aluminum foils. It also has entrance and exit beam ports. The upper ring is used to house the cryotarget.

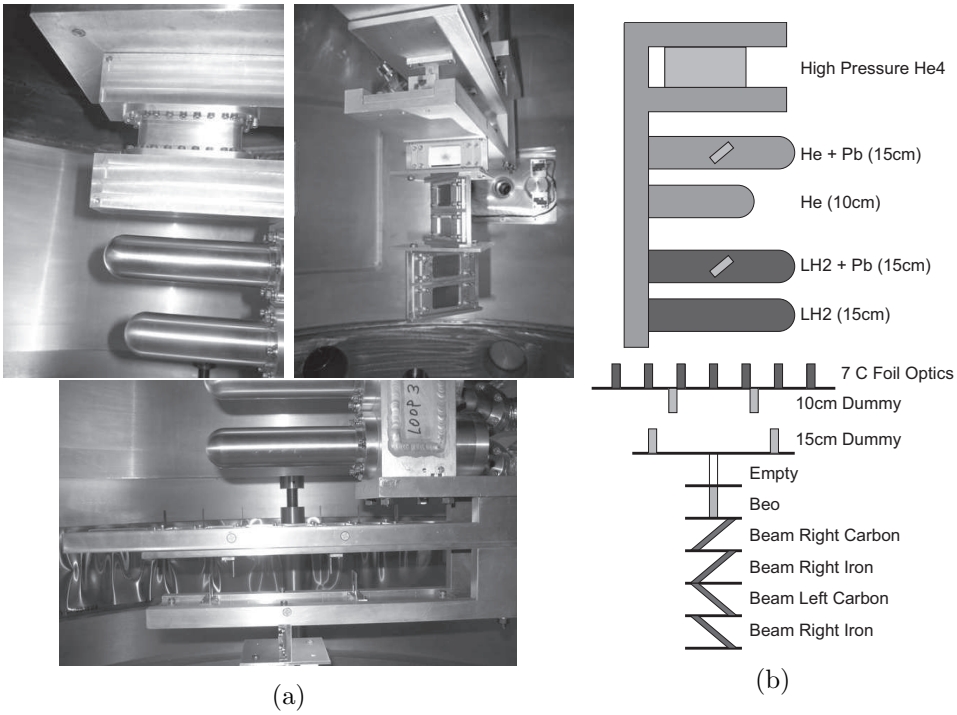

(a) (b)

Figure 2.5: Target configurations for CSR experiment, (a) pictures, (b) illustration

The target configurations for the CSR expriment is shown in Figure 2.5 and in Table 2.1. The cryogenic target system is mounted inside the scattering chamber along with sub-systems for cooling, gas handling, temperature and pressure monitoring, target control and motion, and an attached cali-

bration and solid target ladder. The basic cryogenic target has three independent target loops and, among them, a gaseous helium loop (Loop 1) and a liquid hydrogen (LH_2) loop (Loop 3) were used for the CSR experiment. The LH_2 loop has had two aluminum cylindrical target cells each of which is 63.5 mm in diameter and 15 cm long. A ^{208}Pb foil was held in the top LH_2 cell for cooling purpose. The ^{4}He gas loop has a single vertical cylindrical cell, also made out of aluminum. The cell has a diameter of 10.4 cm which defines the target length. The operating temperature and pressure of the LH_2 target are 19 K and 0.17 MPa, with a density of about 0.0723 g/cc. The ^{4}He gas target has been operated at 7.0 K and about 170 psi, giving a density of about 0.12 g/cc. The targets are arranged in a vertical stack, which can be moved from one position to another by remote control.

Target	Material	Entrance	Exit	Beam L-wall	Beam R-wall
L1 10cm	High pressure ^{4}He	.263 ± .008	.280 ± .005	.245 ± .002	.239 ± .007
L2 15cm	Pb in ^{4}He	.128 ± .002	.194 ± .009	.194 ± .009	.194 ± .009
L2 10cm	^{4}He	.257 ± .005	.120 ± .070	.120 ± .070	.120 ± .070
L3 15cm	Pb in Liquid H_2	.129 ± .001	.207 ± .005	.207 ± .005	.207 ± .005
L3 15cm	Liquid H_2	.217 ± .003	.115 ± .001	.115 ± .001	.115 ± .001

(a) Gas/liquid targets, numbers are thicknesses in mm. All cells are made of aluminum alloy Al7075-T6. The Pb foil in loop 1 is (0.1057 ± 0.0001) g/cm^2 thick and the one in loop3 (0.3187 ± 0.0004) g/cm^2

Target	Material	Thickness (g/cm^2)	Purity
7 foil optics	^{12}C	0.042 ± 0.001	99.5%
10 cm dummy	Al6061-T6	0.259 ± 0.001	N/A
Beam right carbon	^{12}C	0.0894 ± 0.0001	99.95%
Beam right iron	^{56}Fe	0.1027 ± 0.0001	99.99%
Beam left carbon	^{12}C	0.0895 ± 0.0001	99.95%
Beam left iron	^{56}Fe	0.1023 ± 0.0001	99.99%

(b) Solid/optics/dummy targets

Table 2.1: Target configurations for CSR experiment[10]

Besides the cryogenic targets described above, there have been 10 cm aluminum dummy target, used to measure the contribution from the window, seven ^{12}C foil optics target for calibration purpose, and ^{12}C, ^{56}Fe solid foil targets for the production data. The solid foil targets are tilted by about 50 degrees clockwise (cw, beam-right) or counterclockwise (ccw, beam-left) from the beam normal plane, so as to make the electrons travel shorter in the target after the scattering before they enter one or the other spectrometer (Figure 2.6). For example, assuming that the scattering take place at the middle of target length, when both spectrometer are set at 15 degrees, using of "beam left" target makes the electrons travels in the target after

the scattering about twice longer for HRS-R than for HRS-L. Therefore, by comparing the spectra from both HRSs, we can study the external radiative effect.

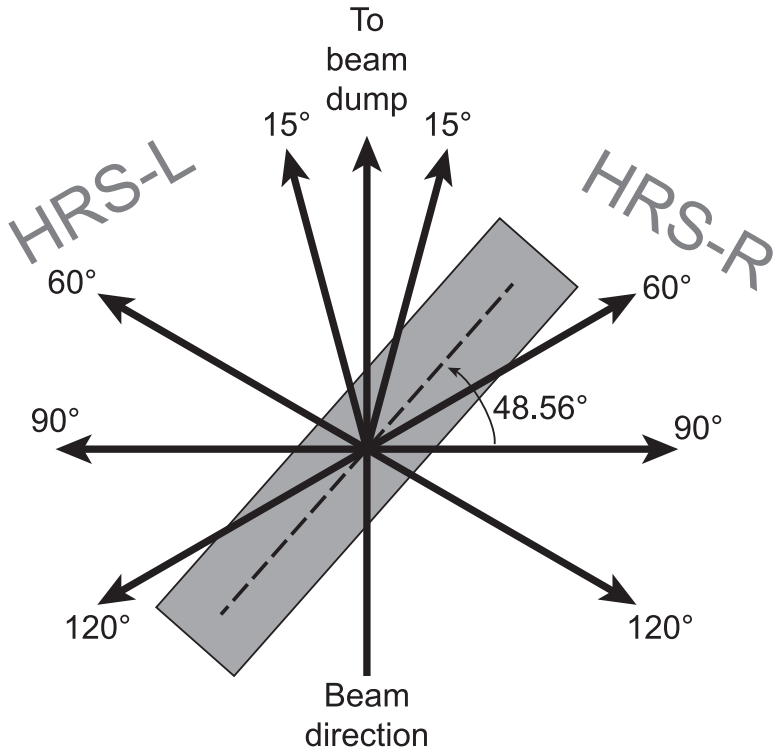

Figure 2.6: Illustration of the beam-left solid foil target (top view). The foil is tilted by 48.56° from the beam normal plane. The direction of the incident beam and the four measured scattering angles (15, 60, 90, and 120 degress) are denoted as lines with arrows. At each scattering angle, the scattered electrons travel different lengths in the target for HRS-L and HRS-R.

2.2.3 Jefferson Lab Hall A High Resolution Spectrometers

The core equipment for detecting scattered particles in the Hall A is a pair of almost identical 4 GeV/c spectrometers. The basic layout is shown in Fig. 2.7. The vertically bending design includes QQDQ superconducting magnets: a pair of quadrapoles followd by a 6.6 m long dipole magnet with focussing endtrance and exit polefaces and including additional focussing from field gradient, n, in the dipole; following the dipole is a third quadrapoles of each spectrometer are identical in design and construction. The main design

characteristics of the spectrometers are shown in Table 2.2.

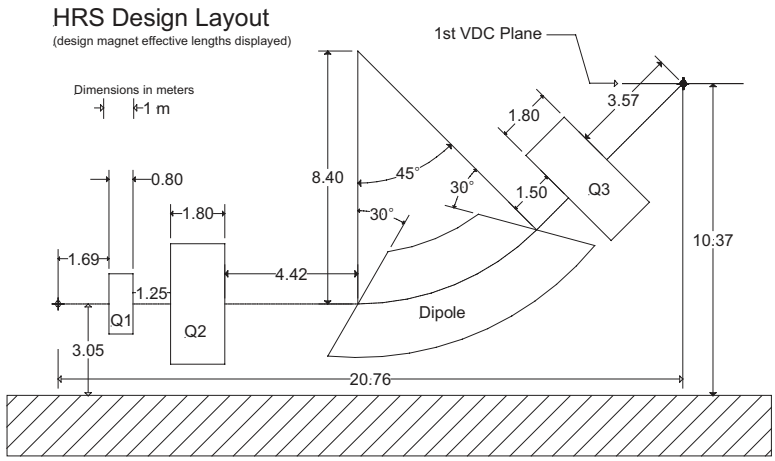

Figure 2.7: Schematic layout of a HRS device, showing the geometrical configuration of the three quadrupole and the dipole magnets. Also shown is the location of the first VDC tracking detector[9].

HRS central momentum

The currents and the magnetic fields of QQDQ magnets are synchronized with the central momentum of the spectrometer (P_0) which can be controlled remotely. And P_0 is monitored by measuring the magnectic field in each dipole using NMR field probes and a Hall probe. The NMR system is very accurate, giving field readings at the 10^{-5} level. The relations between P_0 and the magnetic fields from the NMR probes in the HRSs are:

$$\begin{aligned} \text{HRS-L} : P_0\ (\text{MeV}/c) &= 2702(\pm 1)\, B_{\text{NMR}} - 1.6(\pm 0.4)\, B_{\text{NMR}}^3 \\ \text{HRS-R} : P_0\ (\text{MeV}/c) &= 2698(\pm 1)\, B_{\text{NMR}} - 1.6(\pm 0.4)\, B_{\text{NMR}}^3 \end{aligned} \tag{2.2}$$

where the magnetic field B is in unit of Tesla. Supplemental to the NMR probes, each magnet has a Hall probe mounted in the vicinity of the NMR probes. The Hall probes are used as a backup for the NMR probes and also used in low field operation below $\sim$450 MeV/c, where the NMR probes does not work. In this experiment, the momentum went down to around 100 MeV/c, which is out of the HRS designed value. In this low momentum range, the relation between the momentum and the field measured by Hall probe was studied using eC and eP elastic scattering (in the next chapter).

Configuration	QQDQ vertical bend
Bending angle	45°
Optical length	23.4 m
Momentum range	0.3-4.0 GeV/c[§]
Momentum acceptance	-4.5 % $< \delta$p/p$<$ +4.5 %
Momentum resolution	1×10^{-4}
Dispersion at the focus (D)	12.4 m
Radial linear magnification (M)	-2.5
D/M	5.0
Angular range	
HRS-L	12.5-150°
HRS-R	12.5-130°
Angular acceptance	
Horizontal(ϕ)	± 30 mrad
Vertical(θ)	± 60 mrad
Angular resolution	
Horizontal($\Delta\phi/\phi$)	0.5 mrad
Vertical($\Delta\theta/\theta$)	1.0 mrad
Solid angle at δp/p=0, $y_0 = 0$	6 msr
Transverse length acceptance	±5 cm
Transverse position resolution	1 mm

Table 2.2: Main design characteristics of the Hall A high resolution spectrometers; the resolution values are for the FWHM[9].

Spectrometer central angle

The electron scattering angle, $\theta_{\rm sc}$, is calculated by combining the horizontal ($\phi_{\rm tg}$) and vertical ($\theta_{\rm tg}$) angular distribution measured relative to the central ray of the spectrometer and the spectrometer central angle θ_0 between the beamline and the spectrometer nominal central ray:

$$\theta_{\rm sc} = \arccos\left(\frac{\cos\theta_0 - \phi_{\rm tg}\sin\theta_0}{\sqrt{1+\theta_{\rm tg}^2+\phi_{\rm tg}^2}}\right). \tag{2.3}$$

The spectrometer central angle is determined from marks etched into the floor at a nominal distance of 10 m from the hall center. A closed circuit television camera mounted on a linear translation stage is used to read the floor marks. However, the spectrometers are not constrained to remain along a radius as they move around the hall central bearing by design, and

various factors change the spectrometers pointing by as much as ±4 mm in a non-reproducible manner. A linear variable differential transformer (LVDT) measures the gap between an arm parallel to the spectrometer mid-plane and the outer surface of the scattering chamber to correct the raw floor reading values. The raw angular readings should be then corrected for spectrometer roll/pitch and offset in the location of the support arm with respect to the spectrometer central ray.

During this experiment, each spectrometer moved more than twenty times due to frequent kinematic setting changeover. Spectometer alignments at several angles were surveyed and the result is shown in Table 2.3. The difference between floor/LVDT value and survey result for HRS-L is at most 0.0073 degree (∼0.13 mrad), from which the uncertainty in the scattering angle can be estimated. The eC and eP elastic scattering data can also be used to estimate the uncertainty in the scattering angle, it will be discussed in the next chapter.

Date (in 2007)	HRS	Survey Result	Misptg. cor.	Floor/LVDT	Difference
Oct 4	L	14.635	14.645	14.6423	+0.0027
Nov 7	L	59.990	59.993	60.0003	-0.0073
	R	60.017	59.988	59.9999	-0.0118
Nov 20	R	89.989	89.998	90.0010	-0.0030
Nov 27	L	119.980	119.995	120.000	-0.0050
	R	119.989	120.006	120.000	+0.0060
Dec 4	L	15.023	15.006	14.9991	+0.0069
	R	89.973 (89.971)	89.990 (89.992)	90.0010	-0.0110 (-0.0108)

Table 2.3: Spectrometer central angles; survey results[10] and floor angle read-out numbers. Unit in degrees.

2.2.4 Detector Packages

The layouts of the detector packages of the two HRS are in Figure 2.8. The detectors perform various functions in the characterization of charged particles passing through the spectrometer. These include: a **trigger** to activates the DAQ electronics, collecting **tracking** information (position and direction), and **identification of the scattered particles**. The main

trigger scintillators are also used to provide the timing information. The particle identification is obtained from the gas Cerenkov detectors, lead-glass shower counters and NaI shower detector. A pair of VDCs provides tracking information. The main part of the detector package in the two spectrometers (trigger scintillators and VDCs) is identical; the arrangement of particle-identification detectors differs slightly. For the CSR experiment, NaI(Tl) scintillation detector was newly installed between the S2 scintillator plane and the pion rejector.

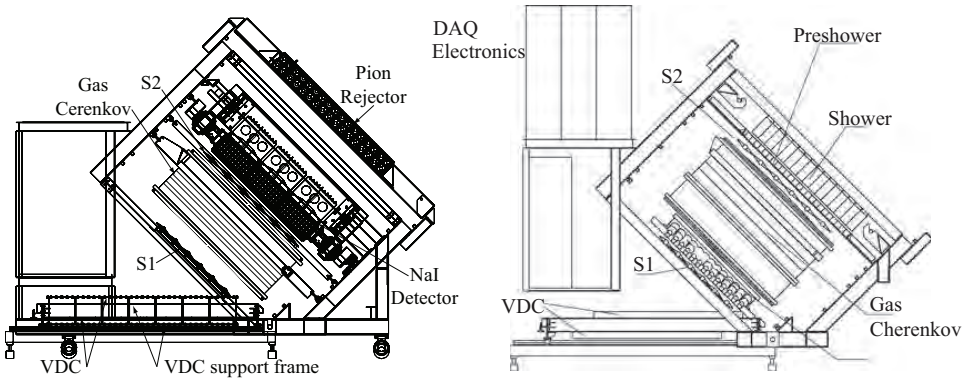

Figure 2.8: Layout of detector packages of HRS-L (left) and of HRS-R (right)

The detector package in both spectrometer is in the shielding huts made of a 10 cm thick steel frame with a 5 cm lead layer inside and a layer of concrete outside. And the Line-of-Sight Block which is a two-meter thick concrete block located 2 m from the target on top of Q1 and Q2 also provides shielding from background signals.

Trigger

There are two primary trigger scintillator planes (S1 and S2), separated by a distance about 2 m. Each plane is composed of six overlapping paddles made of thin plastic scintillator to minimize hadron absorption. Each scintillator paddle is viewed by two photomultipliers (PMTs). The time resolution per plane is approximately 0.30 ns (σ). The trigger system (Fig. 2.9a) is built from commercial CAMAC and NIM discriminators, delay units, logic units, and memory lookup units (MLU). A coincidence between two PMTs is made for each scintillator paddle. The logical OR of these signals is formed individually for the S1 and the S2 plane. For the gas Cerenkov detector

the analog sum of the signals from its 10 PMTs is used to prepare a hit signal. The main trigger for one spectometer is formed by the logical and of the first and the second scintillator plane. The secondary trigger is formed by a hit in either S1 or S2 plane and a hit in the gas Cerenkov detector. The various trigger signals go to the trigger supervisor module which starts the DAQ readout. Most inputs of the trigger supervisor can be individually prescaled. Triggers which are accepted by the DAQ are then retimed with the scitillators to make gates for the ADCs and TDCs.

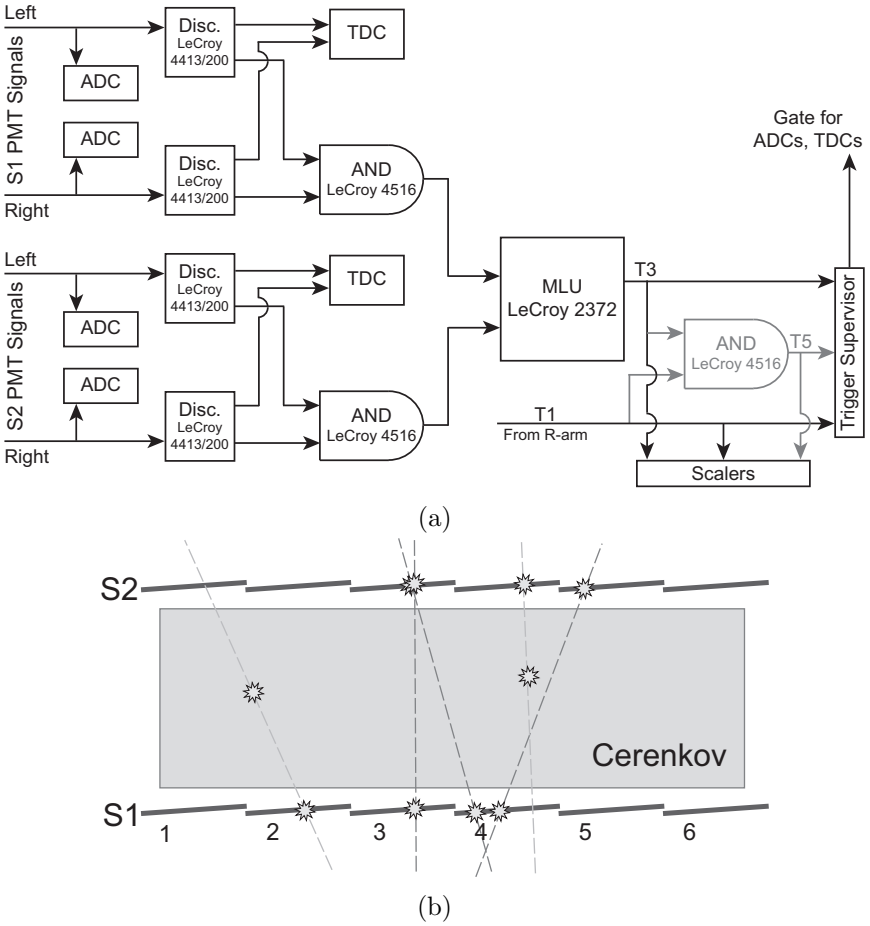

Figure 2.9: (a) Simplified block diagram of the main trigger setup[10][12], (b) illustration of the main(red) and the secondary(blue) trigger[13].

Tracking

Tracking information is obtained from two vertical drift chambers (VDCs). Figure 2.10 shows the layout of the VDCs. Each VDC chamber is composed of two wire planes, separated by about 335 mm, in a standard UV configuration–the wires of each successive plane are oriented at 90° to one another, and lie in the laboratory horizontal plane. They are inclined at an angle of 45° with respect to the dispersive and non-dispersive directions. The nominal particle trajectory crosses the wire planes at an angle of 45°. There are a total of 368 sense wires in each plane, spaced 4.24 mm apart. The electric field of the VDCs is shaped by gold plated Mylar planes, nominally at -4.0 kV when the standard gas mixture of argon (62%) and ethane (38%) is used. In the pocal plane the position resolution is around 100 μm, and the angular resolution about 0.5 mrad.

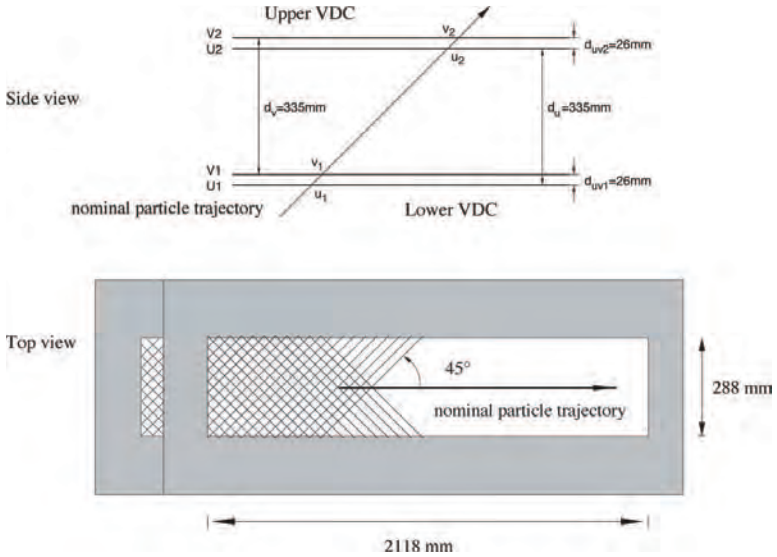

Figure 2.10: Schematic layout of a pair of Vertical Drift Chambers for one HRS. [9]

Particle identification

A gas Cerenkov detector filled with CO_2 at atmospheric pressure is mounted between the trigger scintillator planes S1 and S2. The detector allows an electron identification with better than 99% efficiency (discussed in Chapter 3) and has a threshold for pions at 4.8 GeV/c. The detector has ten spherical mirrors with 80 cm focal length, each viewed by a PMT (Fig. 2.11). The

Cerenkov light emitted from a charged particle is reflected by the mirror and is viewed by PMTs. The sum of 10 PMT signals is used as an event. The length of the particle path in the gas radiator is 130 cm for the gas Cerenkov in the HRS-R, yielding an average of about twelve photoelectrons. In the HRS-L, the length is 80 cm, yielding seven photoelectrons on average.

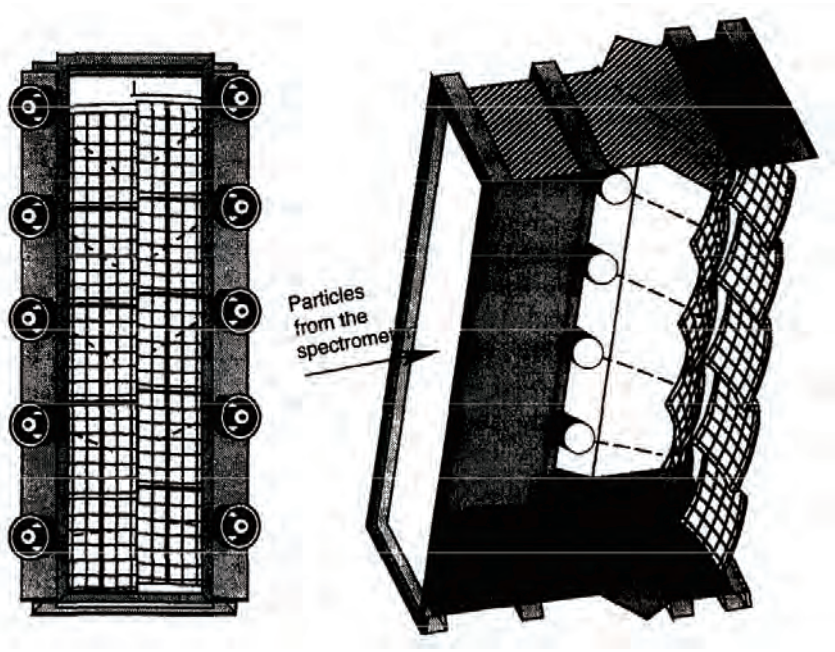

Figure 2.11: Layout of gas Cerenkov detecter. The detecter in each HRS has ten spherical mirrors, each viewed by a PMT.

In the HRS-R, two layers of shower detectors are installed. The 48 lead blocks in the first layer ("pre-shower") are oriented perpendicular to the particle tracks. The 80 blocks in the second layer ("shower") are parallel to the tracks. In the HRS-L, two layers of lead glass blocks ("pion rejector") oriented perpendicular to the tracks are positoned at the end of the detector package.

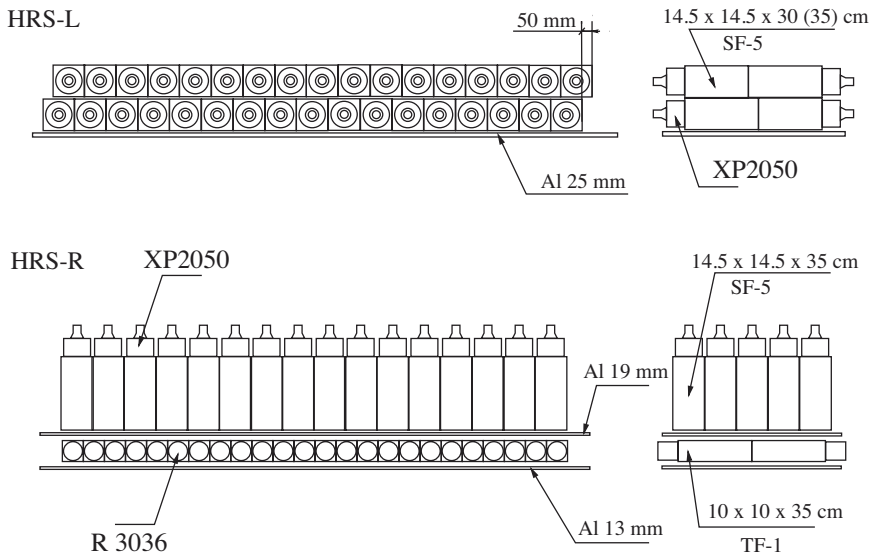

Figure 2.12: Schematic layout of Shower detecters; pion rejector in HRS-L (top) and pre-shower/shower detecter in HRS-R (bottom).

CSR NaI scintillator

A new detector composed of 270 NaI(Tl) scintillator blocks was installed in the HRS-L. More than 300 blocks which had been used at Brookhaven National Laboratory [19] were transferred to Jeffereson Lab, refurbished and reconfigured into three individual boxes (Fig. 2.13). Each box holds 10 horizontal $\times$ 9 vertical blocks. Each block consists of a $5\times5\times12$ cubic-inch rectangular NaI(Tl) scintillation crystal connected with a PMT.

Unfortunately, due to shortage of installing and commissioning time, the optimum high-voltage settings for the PMTs were found in the middle of the experiment. And it was found that during the installation some of PMT channels went out of order and made no signal. Yan [14] did hard work to calibrate the detecter with estimating the energy deposit in the bad channels. So far as now, two boxes in the middle and the bottom have been calibrated reasonably. The calibration result is shown in Figure 2.14a. The resolution is 12% (FWHM) at around the lowest spectrometer momentum, 120 MeV/c, which is better than the pion rejecter.

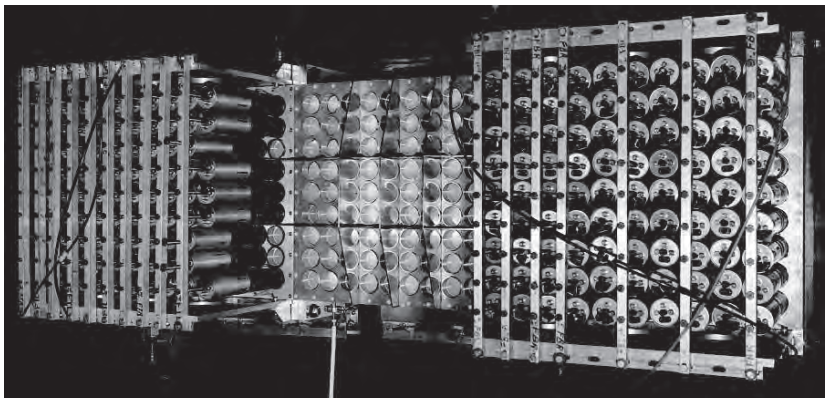

Figure 2.13: A photo of CSR NaI(Tl) detecter. It was taken during the installation, right before attaching PMTs on the middle box.

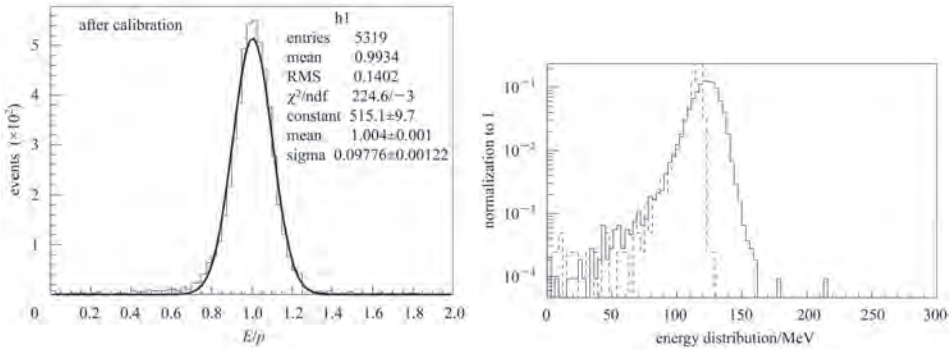

(a) (b)

Figure 2.14: (a) Calibrated NaI(Tl) calorimeter signal (E/p). (b) Comparison of yields between data (solid line) and simulation (dashed line) at a momentum setting of 120 MeV, y-axis in log scale [14].

One of the concerns about CSR experiment was background from low energy electrons which might come from scattering off the walls of magnets in the spectrometer. It is another reason that a detecter with better resolution was installed. However, Monte Carlo simulation by Yan using SNAKE [9] and GEANT (Figure 2.14b) showed the contamination should be at most 0.3%, far smaller than the concern. NaI(Tl) calorimeter was not used in this analysis, because the detecter could not cover the whole spectrometer acceptance due to the uncalibrated top box.

2.2.5 Data acquisition

When a scattered electron satisfies trigger condition, the trigger supervisor opens the gate and starts recording. This makes an event which contains all information of scattering interaction and it is inserted into the CEBAF On-line Data Acquisition (CODA) system. For each event, corresponding data from each read-out-controller (ROC) are collected together. There are four-type components in raw raw data:

- Data of scattered electron information–trajectory, momentum, etc,
- Scalers–normalization factor like beam charge, trigger, etc,
- Information of kinematic setting–Experimental Physics and Idustrial Control System (EPICS), and
- Specific information of the detector setting (detector map).

About three tera-bytes of raw data were obtained from this experiment. The raw data are decoded and the generated ntuples can be analyzed by Analyzer [10] (a Hall A software tool based on ROOT [11]).

2.3 Kinematic Coverage

The kinematic coverage in (ω, $|\mathbf{q}|$) plane is shown in Figure 2.15. At each beam energy, the spectrometer momenta were set to measure the spectrum from the elastic peak down to around $\Delta(1232)$ resonance. Continuous spectra were obtained for most of the beam energies by changing the spectrometer momentum by 7% step. Only one data set of spectrum at $E = 528$ MeV, $\theta = 90^\circ$ is discontinuous at several points around the quasi-elastic peak. There had been one more kinematic settings scheduled at $E = 4$ GeV but we could not take any data for it due to a magnet power supply failure at high current operation. As a result, the overlapped $|\mathbf{q}|$ range among data sets, required for LT separation, is from 550 MeV/c to 950 MeV/c.

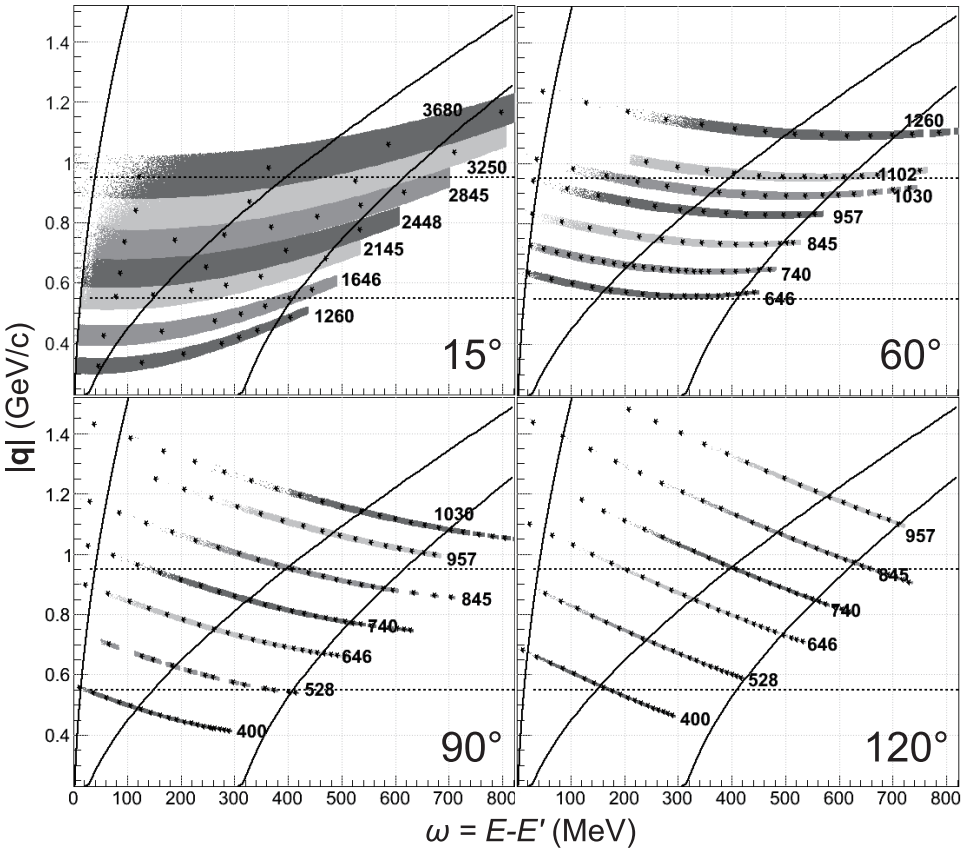

Figure 2.15: Kinematic coverage of JLab E05-110 CSR experiment. Each star represents a single run, $\pm 3.5\%$ of δP/P acceptance allows to have almost continuous spectra along $\omega(= E - E')$ in x-axis, while $|\mathbf{q}|$ in y-axis has finite range for each run by ± 20 mrad horizontal angular acceptance. In each figure, shadowed areas are actual data points from ^{12}C runs, numbers next to them are beam energies, two dashed line denotes for the 0.55 GeV/c < $|\mathbf{q}|$ <0.95GeV/c. And the solid curves are for the estimated positions of elastic scattering peak (left), quasi-elastic peak (W=940 MeV/c^2, middle), and of Δ resonance (W =1232 MeV/c^2, right).

Chapter 3

ANALYSIS PART I

The analysis procedures can be split into several steps: the first step involves the hardware calibrations to reconstruct the good electron events: beamline instruments, spectrometer optics properties and detectors' performance were checked and calibrated to have accurate raw cross sections. Radiative corrections and normalization were applied to the raw cross section to have the absolute Born cross sections. After getting the cross sections, interpolation in $|\mathbf{q}|$ vs ω plane was needed to have response functions in constant $|\mathbf{q}|$ values. Coulomb correction was applied to see the distortion effect of the nuclear Coulomb field. And finally, longitudinal and transverse response functions are separated and Coulomb Sum is derived.

In this chapter, as the first part of the analysis, the steps to produce the absolute experimental cross sections will be described in detail with estimation of the systematic uncertainties.

3.1 Experimental Cross Sections

To obtain the experimental Coulomb Sum precisely, it is important to measure the differential cross sections ($d\sigma/d\Omega d\omega$) with minimizing the uncertainties. The experimental cross section can be written:

$$\frac{d\sigma}{d\Omega d\omega} = \frac{N_{\rm det}/(\prod_i \varepsilon_i)/(1-{\rm DT})}{(N_{\rm inc})\left(\int \rho N_A dx\right)\left(\int d\Omega d\omega\right)}, \tag{3.1}$$

where $N_{\rm det}$, $N_{\rm inc}$ denote the number of detected/incident electrons, $\Pi_i \varepsilon_i$ product of all the efficiencies of the detecters, DT the dead time, ρ the target density, N_A Avogadro number, $\int dx$ the target length, and $\int d\Omega d\omega$ is the acceptance of the spectrometer. Each term in Eq. 3.1 independently

involves its systematics uncertainty. The uncertainty of the cross section can be calculated by adding the contributions from each of the uncertainties in quadrature.

3.1.1 Incident/scattered energy

The uncertainties in the incident and the scattered energies of the electrons affect the Mott cross section (σ_M), the momentum transfers ($\mathbf{q}$ and Q^2) and the virtual photon's polarization (ε) and result in the uncertainty of the response function. The typical uncertainty of the incident electron beam energy is below 0.05% level when the energy is higher than 0.8 GeV, as mentioned in the previous chapter. In this experiment, there were 4 beam energies below 0.8 GeV: 400, 528, 646 and 740 MeV, and there were no arc energy measurement at these energies. On the other hand, HRS central momentum is also known to be as accurate as 0.05%, but this is also guaranteed down to 450 MeV/c where the NMR field probe works. And a large portion of the experimental data was taken below 450 MeV/c (see Figure 2.15; $E - \omega$ is the scattered energy).

15°		60°		90°		120°	
E	$E'_{\rm low}$	E	$E'_{\rm low}$	E	$E'_{\rm low}$	E	$E'_{\rm low}$
1260	810	646	187	400	100	400	100
1646	1147	740	250	528	108	528	98
2145	1605	845	305	646	127	646	107
2448	1838	957	377	740	170	740	110
2845	2135	1030	270	845	135	845	105
3249	2440	1102	333	957	267	957	237
3679	2770	1260	370	1030	100		

Table 3.1: Incident energy and the lowest scattered energy detected (in MeV) at each kinematics

To determine the precise values of the incident and scattered energies, carbon, iron and proton elastic scattering data were used. The scattered energy for the elastic peak ($E'_{\rm el}$) is

$$E'_{\rm el} = \frac{E}{1 + 2E\sin^2(\theta/2)/M_{\rm T}}, \tag{3.2}$$

where $M_{\rm T}$ is the mass of the target nucleus in its ground state. And the energy loss before and after the scattering is taken into account, i.e., E

means $E - E_{\rm loss}$ and E' means $E' - E'_{\rm loss}$. The energy losses are calculated using the most probable energy loss [18] in the target and window materials; for example, the incident energy loss is only around 0.1 MeV in the carbon foil target, while it is around 1 MeV in the liquid hydrogen or in the gaseous heilum target.

First, using the runs where the HRS central momenta were higher than 450 MeV/c, i. e. where the NMR field probe worked, two beam energies (646 and 740 MeV) can be determined. Figure 3.1a shows the elastic peak and the peaks from several nuclear levels of ^{12}C. The elastic peak was resolved with 0.43 MeV FWHM and the corresponding expected beam energy was 740.2 MeV while Tiefenbach energy reading was 739.6 MeV. Analyzing the runs with different scattering angles and with different beam energy, small offsets ($\sim$-0.5 MeV) were found in the Tiefenbach energy reading for these two beam energies (Fig 3.1b). Considering the uncertainties from the spectrometer momentum and from the scattering angle, the uncertainty for these beam energies is assigned to be in the same level with higher beam energies: 0.05 %.

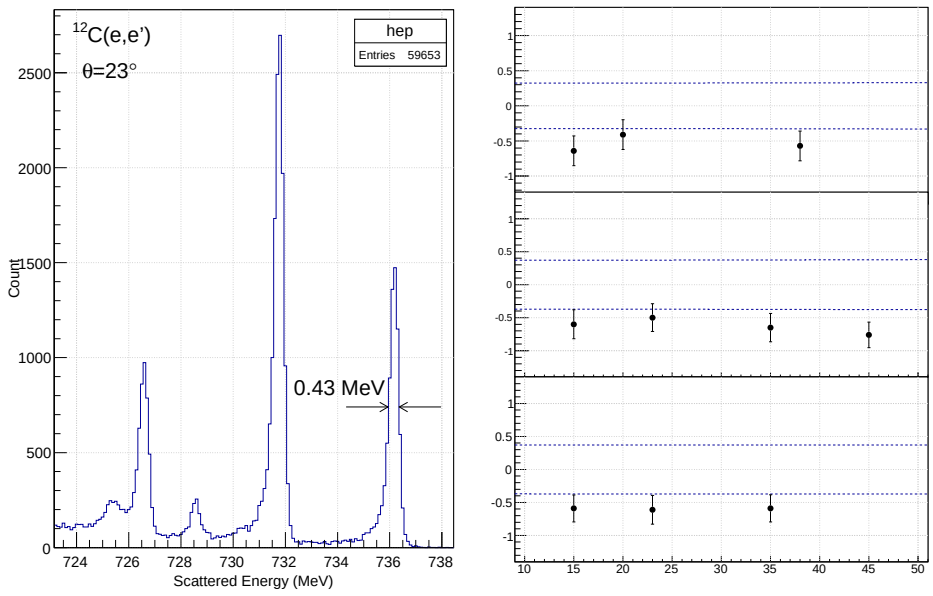

(a) (b)

Figure 3.1: (a) Elastic peak and several nuclear level observed in ^{12}C data with beam energy 740 MeV and scattering angle 23°. (b) Deviation of Tiefenbach energy readings from the expected beam energy calculated from the elastic peaks. Dashed lines denotes the allowable range from the uncertainties of the scattering angles and the HRS resolution.

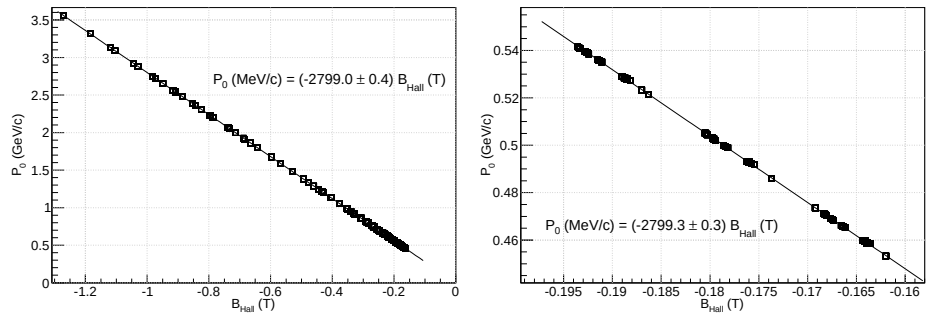

(a) (b)

Figure 3.2: Relation between the HRS central momentum calculated from the NMR field and the magnetic field measured by Hall Probe. (a) Full P_0 range from 0.45 to 3.5 GeV/c. (b) Zoomed into 450-550 MeV/c. Data points are taken from EPICs data in ^{12}C production runs and errors indicate the standard deviations from the straight fitting lines.

Secondly, the scattered energy below 450 MeV, where the NMR probe does not work, should be calibrated by figuring out the relation between the magnetic field measured by Hall probe ($B_{\rm Hall}$) and the HRS central momentum (P_0). Above 450 MeV/c, the magnetic field measured by Hall probe showed a good proportionality with the HRS central momentum calculated from the NMR field as shown in Figure 3.2. It is possible to extrapolate the same coefficient down to the lowest momentum because of the scaling behavior of the magnetic field in an ideal case. Relation between $B_{\rm Hall}$ and P_0 was checked using eP elastic scattering data with known beam energies $E = 646, 740$ MeV at θ=90, 120 degrees (Figure 3.3a). Seperations of the nuclear levels of ^{12}C at this momentum range can also be used to determine the coefficient (Figure 3.3b). The scattered energy (E'_*) from the excited state of ^{12}C with mass M_* can be written:

$$E'_* = \frac{E - (M_*^2 - M_{\rm T}^2)/2M_{\rm T}}{1 + 2E\sin^2(\theta/2)/M_{\rm T}}, \tag{3.3}$$

where the other variables are defined as same as in Eq. 3.2. Then the Hall probe coefficient can be derived by comparison of the separations between the levels in δP/P to the existing data. The result is:

$$P_0\ ({\rm MeV}/c)\ =\ (-2802 \pm 3) B_{\rm Hall}\ ({\rm T}), \tag{3.4}$$

where uncertainty comes from the width of the elastic and inelastic peaks of the proton and ^{12}C. The absolute value of the coefficient was found to be

a little bit bigger than that of higher momenta, but it was still consistent considering the uncertainty.

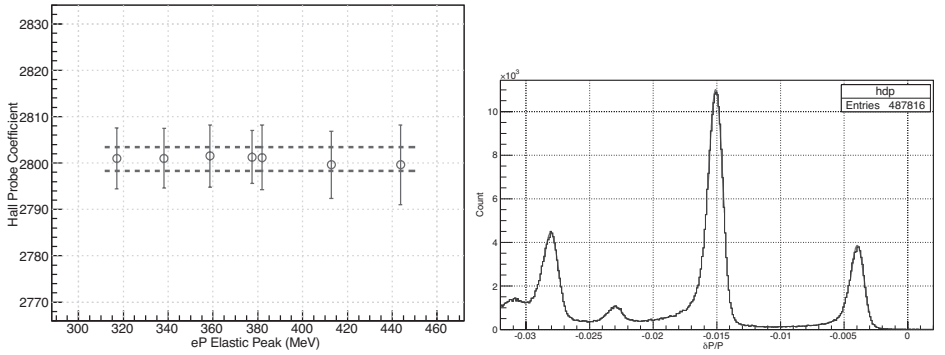

(a) (b)

Figure 3.3: (a) Hall probe constant of the HRS-L below 450 MeV/c using the position of the eP elastic peak. The area between the dashed lines denotes the systematic allowance from the uncertainties in the incident energy and the scattering angle. (b) δP/P spectrum of ^{12}C for $E = 400$ MeV, $\theta = 45°$. The separations of the elastic peak and the nuclear excited states can be used to determine the central momentum of the spectrometer.

Finally, the remaining two lowest beam energies (400, 528 MeV) and the lower central momentum down to around 240 MeV/c (where the lowest eP elastic data were taken) were determined in similar ways. For the momenta below 240 MeV/c, where there was no way to calibrate the Hall probe coefficient but the extrapolated value had to be used, a sufficiently large uncertainty (0.3%) was assigned.

3.1.2 Beam current and charge

Beam Current Monitor calibration consist of two parts*: the EPICS calibration and the scalers calibration. The EPICS calibration provides the absolute current reference using OLO2 cavity monitor and Faraday cup at the accelerator injector section during the calibration run. In the calibration run, I_{Faraday}, I_{OLO2} and the average voltage level of the BCM cavities (Figure 2.4) are measured simultaneously when beam is delivered only to Hall A. After comparing I_{OLO2} with I_{Faraday} to make sure that the absolue beam

*This work is done by Xinhu Yan and re-checked by the author.

current value is reliable, the EPICS calibration constants can be determined by comparing the BCMs' voltages to I_{OLO2}.

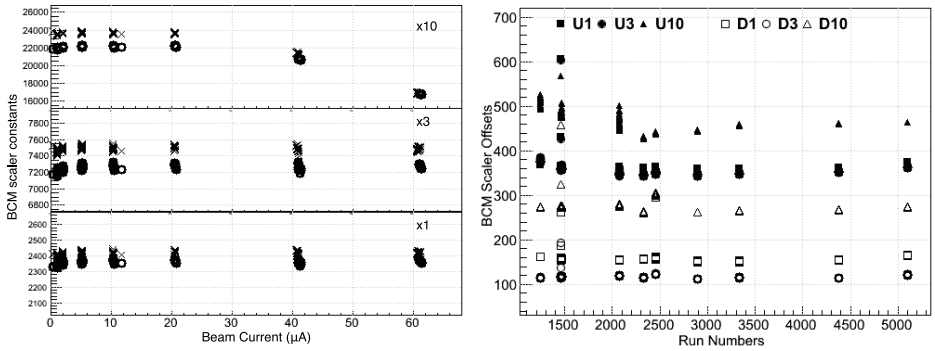

(a) (b)

Figure 3.4: (a) BCM scalers constants for various beam currents. Circles for upstream monitors, crosses for downstream monitors. (b) Offsets from no-beam runs.

After the EPICS calibration was done, six scaler signals from RF cavities were calibrated. The calibration procedure involves finding the offset (signals when there is no beam) and the amplifying constant of each amplifiers. Figure 3.4a shows the amplifying constants. The amplifiers with gain factors 1 and 3 (U1, U3, D1 and D3) show good linear behavior in 5-60 μA beam current range, while U10 and D10 saturate at high current. The offsets were measured from time to time when there was no beam into Hall A (Figure 3.4b). Compared to the scaler constants, the changes in offsets were observed to be negligible during the experimental period. The calibration result is shown in Table 3.2.

BCM	Scaler constant	Offset	BCM	Scaler constant	Offset
U1	2372.4 ± 2.4	362.5	D1	2427.9 ± 2.2	160.1
U3	7294.5 ± 7.5	350.2	D3	7517.4 ± 8.7	126.7
U10	22067 ± 225	442.6	D10	23485 ± 286	321.1

Table 3.2: Beam Current Monitor (BCM) calibration result

In this work, the beam charge ($Q = \int Idt$) for a run was calculated with the intergrated U3 signal, because U3 produced the most stable signal

during the entire experimetal period. The calculation formula is:

$$Q = \frac{(\text{Scaler})_{\text{U3}} - (\text{Offset})_{\text{U3}} \times T}{(\text{Scaler Constant})_{\text{U3}}} \tag{3.5}$$

where T is time of the run which is counted by 1024 Hz clock and recorded into data stream with other scaler data. The other scaler values were used as backup. The differences among U1, U3, D1 and D3 were taken into account to estimate the uncertainty. Considering the stability and the reliability of the BCM, 0.3% of uncertainty was assigned to beam charge.

3.1.3 Deadtime

Detector deadtime

Detector deadtime, or electronics deadtime occurs when an event is followed by another before the gate is ready for the latter. It can be simply calculated by multiplying the trigger rate and a single gate opening time, which is ∼100 ns for each HRS. Or, it can be checked by testing the proportionality of the trigger rate to the beam current.

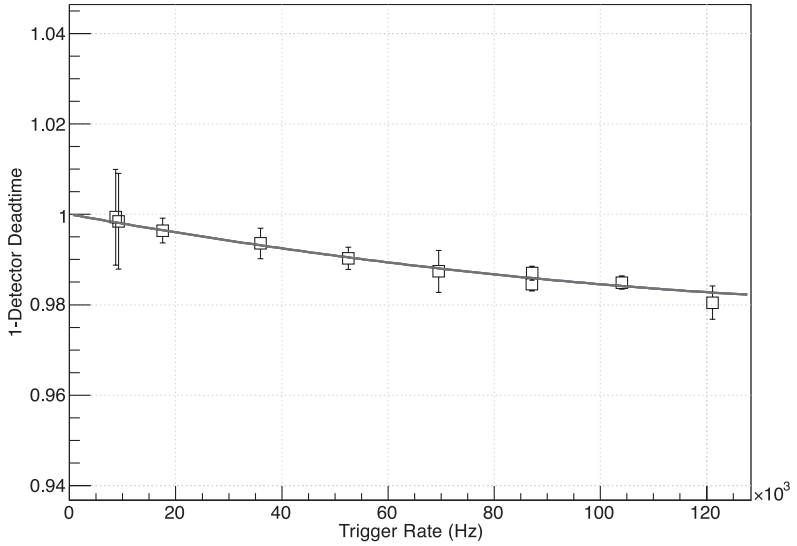

Figure 3.5: Deviation from the proportionality of the trigger rate to the beam current.

Figure 3.5 shows the deviation from the proportionality, which directly means the electronics deadtime in percent unit, as a function of the trigger

rate. The deadtime was at most 2 percent at the highest rate ∼100 kHz. Since most of the production data were taken with the rate lower than a few times 10 kHz, the deadtime from electronics is very small.

Computer deadtime

The computer deadtime (CDT) occurs during the process of writing the experimental data into computer disk. CODA stores each event by its trigger type separately and controls the recording rate by adjusting the prescale factor (PS). Then the computer deadtime is defined by comparing the number of events stored in the computer (N_{DAQ}) and the number of prescaled raw trigger events (N_{trigger}/PS), which is recorded independently in the scaler information:

$$\mathrm{CDT} = 1 - \frac{\mathrm{PS} \times N_{\mathrm{DAQ}}}{N_{\mathrm{trigger}}}. \tag{3.6}$$

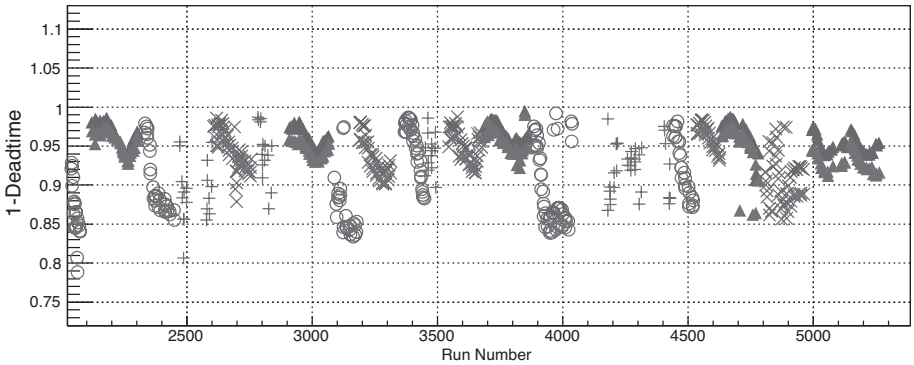

Figure 3.6: Computer deadtimes of all ^{12}C production runs. Different symbel denotes the different scattering angle.

During the experiment, the computer deadtime was controlled to remain less than about 15% for the most of the production runs by adjusting the prescale factor (Figure 3.6).

3.1.4 Tracking efficiency

VDCs detect tracks of the scattered electrons and reconstruct target variables which give the scattering information. However, the inefficiency of VDC wire and the failure of track finding by track reconstruction algorithm

may result in the tracking failure. The inefficiency of a wire can be found by counting the events in which the wire did not fire while two neighboring wires did fire. In an orinary environment when the trigger rate is smaller than several tens of kHz, the wire inefficiency is less than 0.1%. The wire efficiency cannot be separated from the tracking efficiency and is incorporated into the multi-track correction in runs with extraordinary high rate. In other words, wire efficiency can be ignored and the failure of track finding is solely considered for the tracking efficiency.

A multi-track event means an event consiting of two or more tracks found by VDC within a single gate opening interval. The event may consist of mixing of good electrons and backgrounds. In normal condition, where the trigger rate is lower than a few kHz, the portion of multi-track is less than a few percent. In this case, there is no harm to estimate that at least one good electron event is in one multi-track event. But there were some runs with trigger rate much higher than 10 kHz. In these runs, multi-track events possessed more than a few percent, and therefore more careful treatment was necessary (Figure 3.7a).

Even though each track of the multi-track event can be reconstructed by the algorithm, the reliability is still poorer than that of a single track event. Therefore, instead of analyzing the multi-track events, only single track events are used in producing any spectra, and the multi-track events are treated using the tracking efficiency.

The tracking efficiency can be defined:

$$\varepsilon_{\rm tr} = \frac{\text{Number of good single track events}}{\text{Number of good events}}.$$

Here, the "good event" in the denominator means the event which has one or more tracks and the energy deposit in the shower detecter is larger than the cut. Because not any reconstructed track of a multi-track event is so reliable as that of a single track event, a "good event" can only be defined by its energy deposit in the shower detecter. If there were at least one good electron in the events, the energy deposit in the shower should be equal to or larger than the energy deposit of a single track event.

After the cut, $\sim$70% of the multi-track events survived in low trigger rate runs, which is smaller than the naive estimation mentioned above. And as the trigger rate grows, the portion of muli-track survivors also grows and reaches higher than 90% at about 100 kHz. Figure 3.7 shows the relation between the tracking efficiency and the trigger rate. For the production data, the trigger rate was never higher than 100 kHz, and therefore the tracking efficiency was always better than 90%. The uncertainty was estimated from

the deviations of data points from the linear fit shown in Figure 3.7. The uncertainty is at most 0.5%.

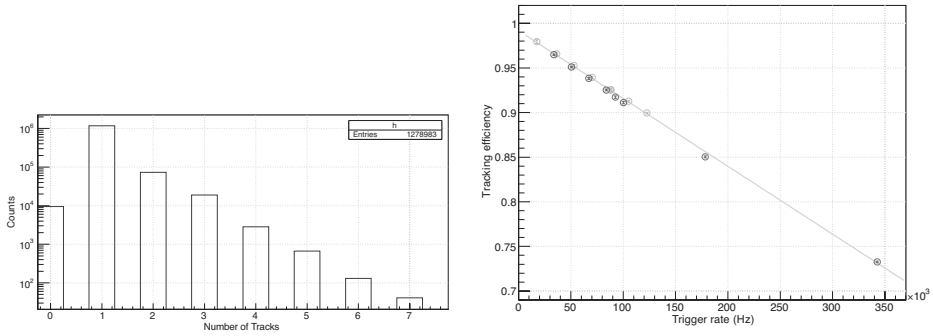

(a) (b)

Figure 3.7: (a) An example of the number of tracks from a high trigger rate run (Run 21564, ∼70 kHz). (b) Tracking efficiency versus raw trigger rate.

3.1.5 HRS optics and track reconstruction

†The transfer of a charged particle from the interaction point through a series of magnets to the focal plane can be represented by a simple maxtrix equation. The "optics" of HRS means finding the matrix which allows the reconstruction of the interaction vertex at the target from the coordinates of the detected particles at the focal plane in the VDC. In other words, the optics is the mathematical mapping of the magnetic field of the HRS. Data obtained with a set of foil targets (which define a set of well-defined interaction points along the beam; see Fig. 2.5.) and a sieve slit collimator were used to determine the optical matrix elements.

The ideal design of HRSs only considered the first order transport maxtrix. But in practice, the expansion of the focal plane coordinates is performed up to fifth order. A set of tensors Y_{jkl}, T_{jkl}, P_{jkl}, and D_{jkl} links the

†A great effort was taken by Yao [15] for the optics calibration. In this thesis, the procedure and the result are briefly summarized. Details can be found in the reference.

focal-plane coordinates to target coordinates according to

$$\begin{aligned} y_{\rm tg} &= \sum_{j,k,l} Y_{jkl} \theta_{\rm fp}^j y_{\rm fp}^k \phi_{\rm fp}^l, \\ \theta_{\rm tg} &= \sum_{j,k,l} T_{jkl} \theta_{\rm fp}^j y_{\rm fp}^k \phi_{\rm fp}^l, \\ \phi_{\rm tg} &= \sum_{j,k,l} P_{jkl} \theta_{\rm fp}^j y_{\rm fp}^k \phi_{\rm fp}^l, \\ \delta &= \sum_{j,k,l} D_{jkl} \theta_{\rm fp}^j y_{\rm fp}^k \phi_{\rm fp}^l \end{aligned} \tag{3.7}$$

where the tensors Y_{jkl}, T_{jkl}, P_{jkl}, and D_{jkl} are polynomials in $x_{\rm fp}$. For example,

$$Y_{jkl} = \sum_{i=0}^{m} C_i x_{\rm fp}^i. \tag{3.8}$$

These optics tensor coefficients are determined from a χ^2 minimization procedure in which the events are reconstructed as close as possible to the known position of the corresponding foil target (in the case of $z_{\rm react}$) or the sieve-slit hole (in the case of $y_{\rm sieve}$ and $x_{\rm sieve}$). The definition of the variables can be found in Figure 3.8.

One set of optics tensor coefficients is not applicable to whole range of the spectrometer momentum of this experiment, 0.1-4 GeV/c. Elastic scattering data were taken at four different incident beam energies, 400, 645, 740 and 1102 MeV, on the single foil and on the multi foil ^{12}C target for this experiment. Unfortunately, by mistake, 645 and 740 MeV data are taken with rastered beam, which made the quality of track reconstrunction worse than expected. However, it was found that the coefficients of these two sets are not far from the 1102 MeV set. In this analysis, the 400 MeV optics set was applied to the data with the spectrometer momenta below 450 MeV/c, it is called "low (energy) optics set" hereafter. And for the data with the HRS momenta above 450 MeV/c, 1102 MeV set was used, "high (energy) optics set".

The reconstructed multi-foil target and the sieve slit collimator with the high optics set are shown in Figures 3.9 and 3.10. For the low energy data, the result is similar but has poorer resolutions caused mainly by heavier multiple scattering.

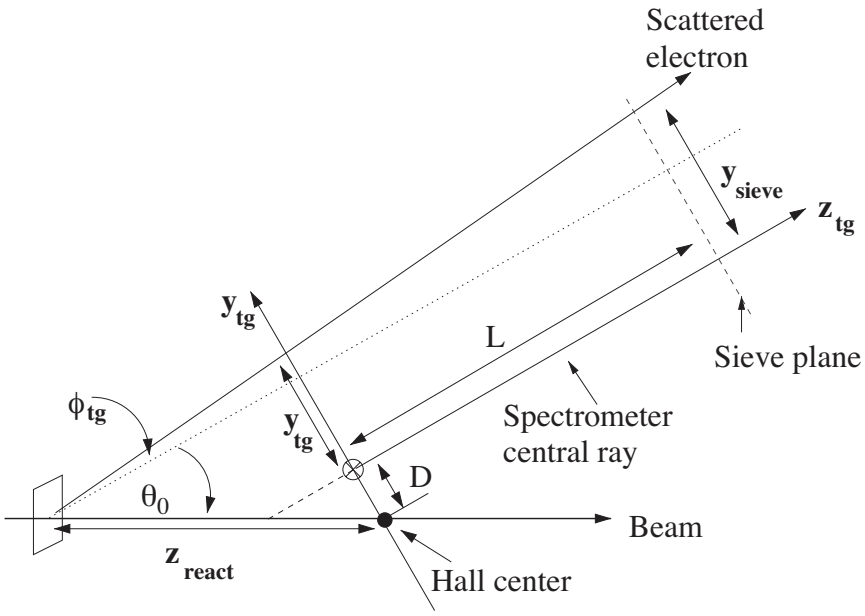

Figure 3.8: Coordinates for electrons scattering from a thin foil target [9]. **L** is the distance from Hall center to the sieve plan, while **D** is the horizontal displacement of the spectrometer axis from its ideal position. The spectrometer central angle is denoted by θ_0. Note that $x_{\rm tg}$ and $x_{\rm sieve}$ are verically down (into the page).

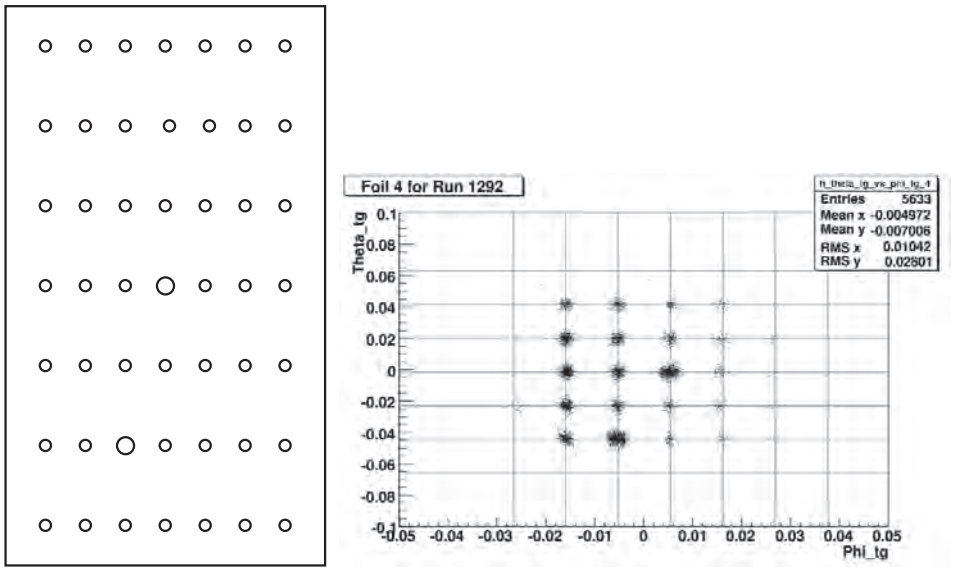

(a) (b)

Figure 3.9: (a) Geometrical and (b) reconstructed configurations of the sieve slit [15].

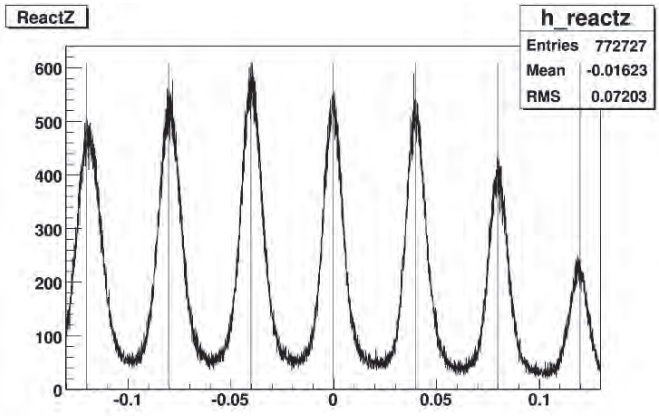

Figure 3.10: Reconstructed multi-foil ^{12}C target; the reaction point along the beam direction (z_{react}) is shown. 4-centimeter spaces between any two foils are well reconstructed [15].

Acceptance

As shown in Table 2.2, the acceptances of the HRS are 30 mrad in horizontal angle, 60 mrad in vertical angle and ±4.5% of ΔP/P. But these number do not mean that all of the electrons in those range pass through the spectromter and reach the detector to form events. Some of the electrons close to the edge of those acceptances can be missing or, processes such as multiple scattering and energy loss inside the spectrometer can change the original spectrum at the scattering vertex.

A usual way to find the spectrometer acceptance is comparing the data to an adequate Monte Carlo simulation. But, in this analysis, it was found that, at least for the single foil targets, a fairly stable acceptance could be achieved with a simple geometrical cut on the angular spectra.

Angular acceptance

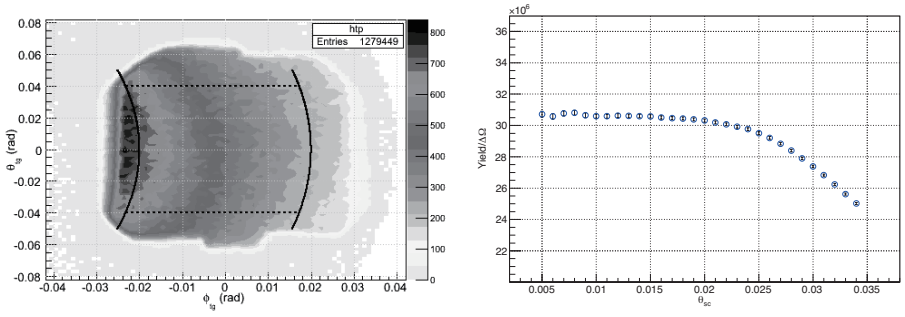

(a) (b)

Figure 3.11: (a) Augular distribution of the events from a 15° run. Geometrical cut defined by the area between a pair of curves ($\theta_{\rm sc} - \theta_0 = \pm 20$ mrad) and between two dotted lines ($\theta_{\rm sc} = \pm 40$ mrad) is also shown. The cut becomes more close to a rectangle at the backward angles. (b) Normalized yields as a function of scattering angle ($\theta_{\rm sc}$) cut from a run with $P_0 = 250$ MeV/c.

Figure 3.11a shows a typical angular distribution; most events were distributed in ±30 mrad horizontally and in ±60 mrad vertically. With $\theta_{\rm sc}$ in ±20 mrad of the HRS central angle, the events were distributed linearly along θ_{sc}, which made the normalized yield stable with varying $\theta_{\rm sc}$ cut up to around ±20 mrad as shown in Figure 3.11. Vertical distribution was

studied in the same manner. To maximize the statistics within the stable acceptance, $|\theta_{\rm sc}| < 20$ mrad and $|\theta_{\rm tg}| < 40$ mrad cuts were chosen, denoted by the area between two solid curves and two dotted lines in Fig. 3.11a.

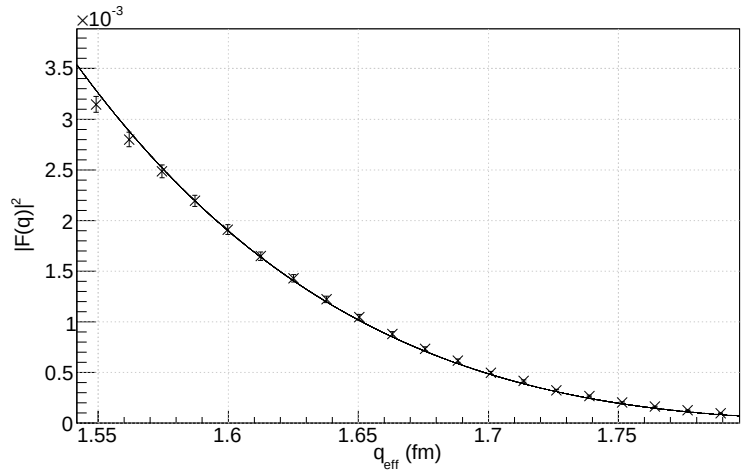

Figure 3.12: Elastic form factor of ^{12}C obtained from a single kinematic setting ($E = 1260$ MeV, $\theta = 15°$) of the HRS-L. The corresponding effective momentum transfer is 1.67 fm at center, but the data are spread in q from 1.55 fm to 1.8 fm due to the wide open cut ($\pm$20 mrad) on the scattering. Chopping the data into 20 bins in the scattering angle, the form factor from each bin shows a good agreement to the phase shift [25] calculation result, which implies a quite stable geometrical angular acceptance in the HRS. Here, data from 7 runs are statistically averaged, and the error bars include the systematic uncertainties from the scattering angle and the beam energy.

The reason why $\theta_{\rm sc}$ was used instead of $\phi_{\rm tg}$, was that the dependence of the cross section on $\theta_{\rm tg}$ could be neglected. And the dependence on $\theta_{\rm sc}$ could be directly seen. Figure 3.12 shows the ^{12}C elastic cross sections at $E = 1260$ MeV, $\theta = 15°$. Data, chopped into 20 bins in $\pm$20 mrad scattering angle, show good agreement with the theoretical calcultion in whole range, only with the radiative corrections.

The stability of the acceptance at the edge of $\theta_{\rm sc}$ is, generally, expected to be not as good at low energy ($E' < 250$ MeV) as at high energy, because more electrons can be lost due to multiple scattering. But those low energy data exist only for 90 and 120 degrees, where the cross sections do not change as much with the angle variation as at the forward angles.

In addition, for the forward angle, where the cross section may vary

considerably in the large geometrical angular cut, the finite acceptance correction is required. It will be discussed later in this section.

Acceptance in $\Delta P/P_0$

While most data were taken with changing the HRS momentum (P_0) by 7% step, some of them were taken with 3.5% step in order to investigate $\Delta P/P_0$ acceptance. Figure 3.13 shows normalized yields of a series of $\Delta P/P_0$ overlapping runs. The yield at around the edge of the acceptance from a run is compared to the one at around middle from the neighbor, which can tell the relative correction of the acceptance.

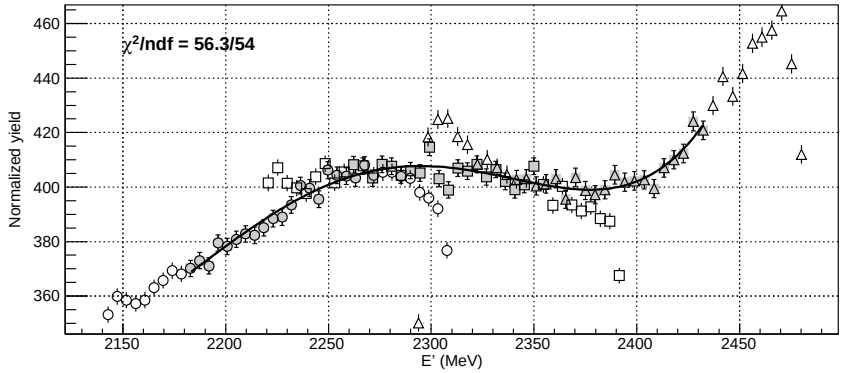

Figure 3.13: Using a series of 3.5% step $\delta P/P_0$ runs, correction factors are derived. Different symbols refer to the data from different runs, and shadowed symbols are points used in fitting, which are in $\pm 2\%$ of each P_0.

Figure 3.14 shows the resulting correction factors (i. e. acceptance functions) for the high and low energy data. For application, interpolated functions were used. At around middle, $\Delta P/P_0$ <2%, the correction is negligible for both. Several percent enhancement was found at around the low edge, and several percent suppression at the other edge. This tendency was found all over the spectrometer momentum range, and it is amplified as the spectrometer momentum gets lower.

The overlapped data were taken at $E' > 360$ MeV. And for E' lower than that, where one would expect much worse fluctuation, no data were taken. However, by adjusting the size of E' bin, the uncertainty from the acceptance could be reduced.

For application to the production data, in order to minimize the statistical fluctuation in the cross section spectrum, events in -3.5%< $\Delta P/P_0$ <3.3%

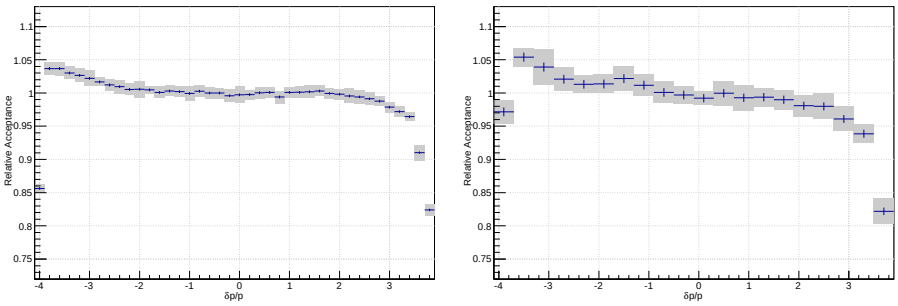

Figure 3.14: $\delta P/P_0$ relative acceptance functions (correction factors) for high energy (left), and for low energy (right). Shadows are deviations from several data sets.

were chosen and put into histrams which have the size of 10 or 20 MeV E' bins with the bin center fixed at $10n + 5$ MeV (n is an integer). The $\Delta P/P$ acceptance was corrected event by event using the acceptance function. This binning scheme had an advantage for low energy. Below 400 MeV, good events of a run were distributed in at most three E' bins. Then the bins were large enough to compensate the acceptance fluctuation in themselves. Even at the edge of $\Delta P/P_0$ of a run, the other edge of the neighboing run compensate the fluctuation.

The uncertaintiy due to the acceptance was assigned from the deviations shown in Figure 3.14: 0.8% for high energy ($E' > 450$ MeV) data, and 1.6% for low energy data.

3.1.6 Backgrounds

In the forward angle (15°) data, most of the events survived after the acceptance cut described above are good electrons. For some of the lowest incident energy, radiative tails from the elastic scattering process are not negligible but can be subtracted using radiative corrections. The main sources of the backgrounds at the backward angles are π^- particles produced in the target and the electrons from e^+e^- pair production.

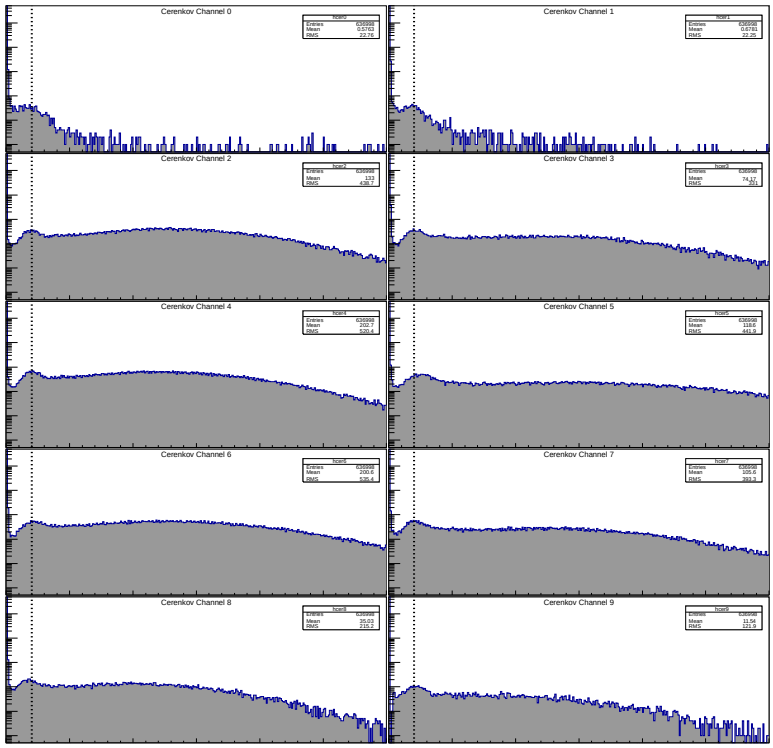

(a)

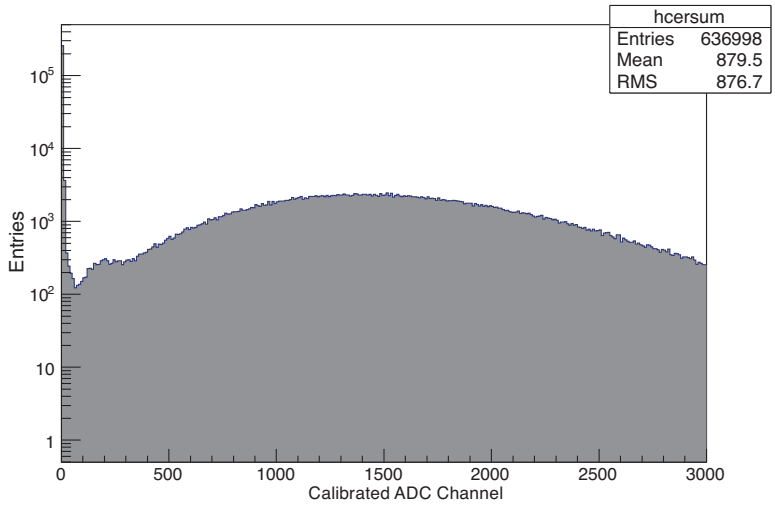

(b)

Figure 3.15: (a) Typical calibrated ADC signals of 10 channels of the L-HRS Cerenkov detector. (b) Sum of the ADC signals. Signals of the single Cerenkov photon are aligned at around the channel 200.

Pion

Most pions can be eliminated by a proper cut on the sum of the Cerenkov ADC signals. Figure 3.15 shows the calibrated ADC signals and the sum of them[‡]. Most of the background particles, including pions, do not produce any signals in Cerenkov detector. And most of the electrons produce at least one Cerenkov photon.

For HRS-R, the efficiency can be determined using shower detecter signals. Since pions deposit much smaller energy in the detecter than electrons do, samples of pions and electrons can easily be separated in the ADC spectrum (Fig. 3.16). Cutting the events below channel 350 of the Cerenkov ADC sum left (99.6±0.1)% of good electrons, while 0.7% of backgrounds still remain.

For HRS-L, it was not easy to use NaI detecter to study the efficiency because the detector did not cover the whole acceptance. Electron (pion) dominant runs were used, instead, to determine the electron detection (pion rejection) efficiency. Electron dominant runs are some of the forward angle, high energy runs, in which pion contribution is negligible. The electron detection efficiency was found to be 99.0±0.1% with the same (350) channel cut. It was a little bit worse than HRS-R, which make sense because Cerenkov detector in HRS-R is longer than one in HRS-L. And more than 99.0±0.5% of pions were found to be eliminated by the cut.

e^+e^- pair production

γ-rays produced by the decay of π^0 produced in the target can create e^+e^- pairs; e^- produced in this process, with momenta in the range of the momentum acceptance of the spectrometer, simulate electrons originating from inelastic scattering on the nucleus. To evaluate this contamination and assuming equal yield for e^- and e^+ production, the e^+ spectra were measured by reversing the magnetic field in the spectrometer at the several backward angle (90 and 120 degrees) kinematics of the experiment. Because e^+ spectra were not measured at all kinematics, instead of direct using of the measured e^+ cross sections, the parametrization using EPC code and J.-P. Chen's calculation were used [17]. Chen's calculation had been used for analyzing SLAC NE9 experimental data, it generates the e^+e^- pair production cross sections using the existing pion spectra. In this analysis, the pion spectra generated by the fortran program EPC were used as input for the Chen's calculation. And the generated positron cross sections were corrected (folded)

[‡]Calibration of the Cerenkov detecter was done by Yan [16].

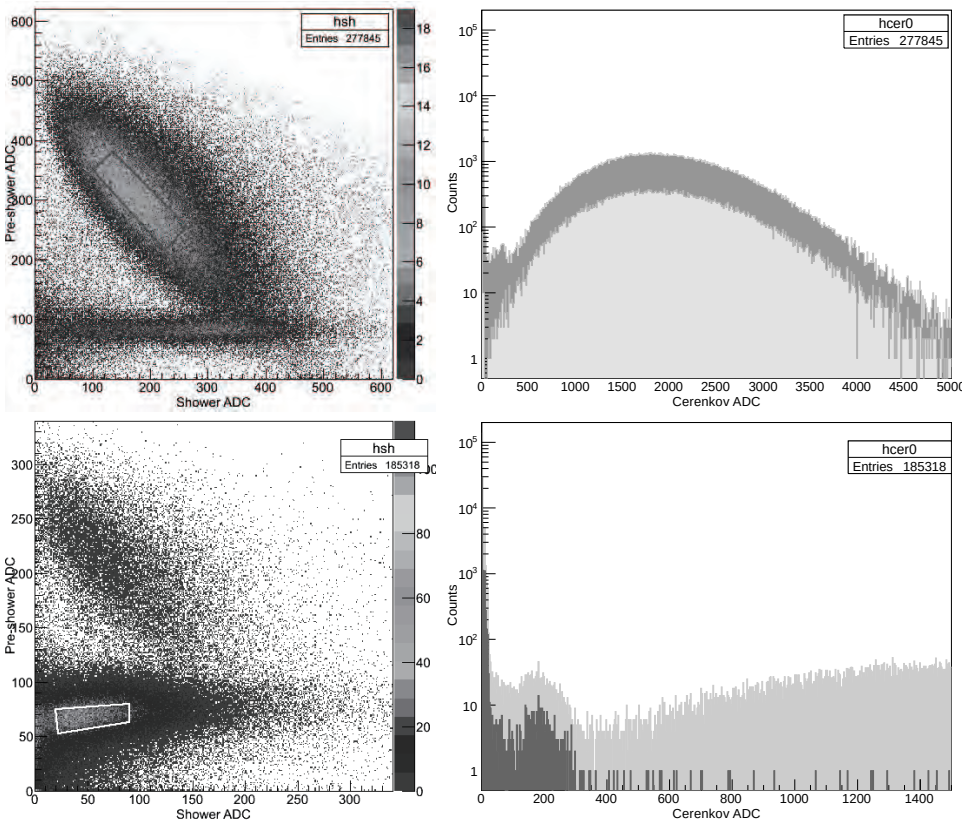

Figure 3.16: Electron detection efficiency (top) and pion rejection inefficiency (bottom) of gas Cerenkov detector. The electron (pion) samples were chosen inside the small dark (bright) rectangle in the left shower spectrum.

for radiative effects using the radiative correction program. Because the experimental conditions such as the scattering angle, the target material, the target thickness, the material after the target and the detector acceptance differ from Chen's experiment, the generated cross sections have been multiplied by a constant for each target at a given scattering angle. The constant was chosen to minimize χ^2 of the fitting of the measured spectrum to the generated one.

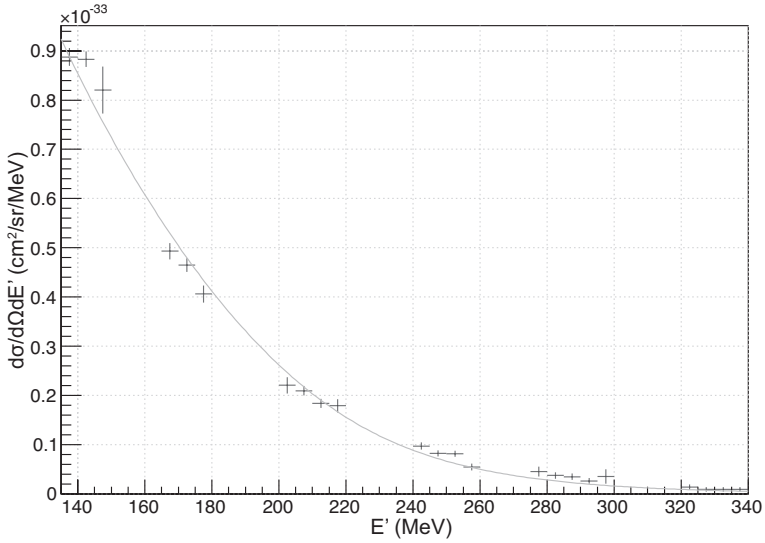

Figure 3.17: ^{12}C(e^-, e^+) cross section, $E = 845$ MeV, $\theta = 90°$. Soild curve is calcuation using EPC and J.-P. Chen's parametrization

Figure 3.17 shows the measured e^+ spectrum with the fitting result at 845 MeV beam energy and 90 degrees scattering angle. At the same angle of a target, the constant did not change by varying the incident electron energy. The constants were found to be different at the different angles and for the different targets; which is reasonable in the sense that the material thicknesses are different from one another. And the differences may also come from the imperfect pion spectra generated by the EPC code. For the unmeasured 60 degree spectra, the existing Saclay data have been compared to the calcuation to derive the constants.

This background increases with the incident electron energy and decreases with the scattering electron energy. The contamination is less than a few percent near the quasi-elastic peak, and up to several tens of percent maximum at high energy loss. Although the calculated spectra describe the measured ones in a good agreement, due to many other unmeasured kinematic points, 10% uncertainty is assigned to this pair electrons contamination, which result in at most about 2% uncertainty in the final electron cross section.

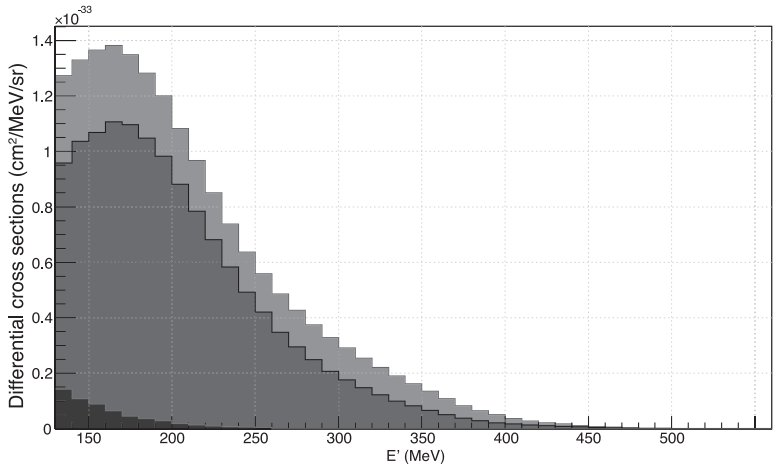

Figure 3.18: Raw spectrum of E=740 MeV, 120°, ^{12}C data. Light gray area denotes the cross sections from electron events, dark gray area the pion cross sections produced by reversing the cerenkov cut, and the darkest denotes the backgrounds from e^+e^- pair production.

3.1.7 Center-of-bin correction

With the large opening angular cut ($|\theta_{\rm sc} - \theta_0$ <20 mrad), as mentioned previously, the cross section at a certain central HRS angle actually represents the average cross section of θ_0±20 mrad. As shown in Fig. 2.15, the effect is larger on forward angle data. If the physical cross section changed linearly in the acceptance, no correction would be necessary. Or, if we know the the cross sections pretty well, such as carbon or proton elastic case, we can use the parametrized cross section to correct this finite acceptance effect. But we don't know the exact behavior of the quasi-elastic response around a particular angle. Hence, the correction should be performed with the data itself.

For 15 degrees, which have enough statistics, the data were split into 5 bins of $\theta_{\rm sc}$ (-20∼-12, -12∼-4, -4∼4, 4∼12, and 12∼20, in mrad). Then 5 cross sections were obtained, then are parametrized by fitting to a parabolic curve. The value at the middle of the curve was compared to the average value, to determine the correction factor. The resulting correction factor was significant at around the rise of the quasi-elastic peak, up to several tens of percent. And it was a few percent for the other range.

For other angles, where the statistics is worse than 15 degrees, same procedure was performed with 3-angle-bin splitting. As expected, the cor-

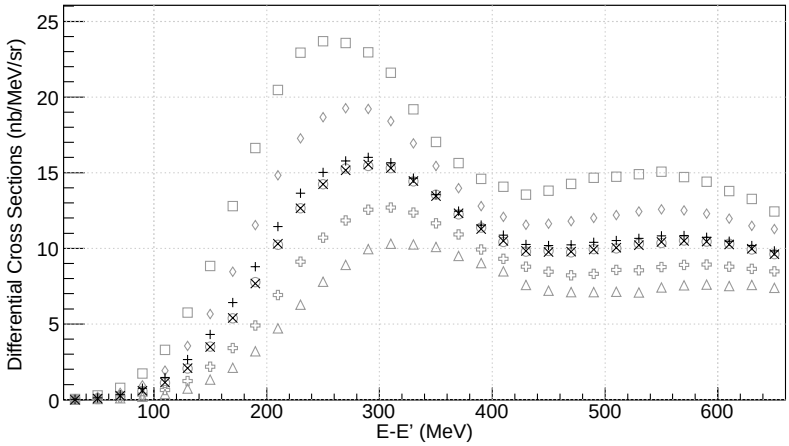

Figure 3.19: An example of center-of-bin correction, E =2845 MeV, $\theta = 15°$. Data are divided into 5 bins out of ± 20 mrad of θ_{sc}. Plus(+)'s are the uncorrected cross sections from whole angular acceptance, crosses($\times$) are the corrected ones. Squares are for the most forward angle bin($14.0833° \pm 4$ mrad) data, and triangles for the most backward angle bin angle bin($15.9167° \pm 4$ mrad).

rection was small for backward angle data. At 60 degrees, the correction is at most several percent at the rise of a quasi-elastic peak, and negligible beyond. At more backward angles, almost no corrections were found at $E' > 200$ MeV. At very low E' (below 200 MeV), small increases were found after the correction. This can be understood as the compensation for the loss at the edge of the spectrometer acceptance.

Using the similar method, elastic cross sections of ^{12}C and of proton, which will be discussed in the next section, were also corrected. The results were then compared with theoretical corrections which are available in elastic case. The differences were at most 0.5%. Because the dependence of the cross section on the scattering angle is smaller for the quasi-elastic scattering than for the elastic scattering, the uncertainty of this correction was assigned to be 0.3% at most.

3.1.8 Radiative corrections

In any electron scattering process, the electron loses additional energy by the radiation of (real or virtual) photons not associated with the nuclear

transition[§]. As a result, the electron spectrum which is measured can differ appreciably from the one which would have been produced, in the absence of this radiation, by the processes one wishes to study. For a given energy loss in the detected electron spectrum, one must (a) subtract the radiative tail of the elastic electron-nucleus scattering, and (b) perform an unfolding procedure to obtain the appropriate corrections for inelastic (continuum) part of the spectrum.

The formalism and the practical method of the radiative corrections is well established by Mo and Tsai [21], and has been widely used in analyzing the electron-nucleus (or muon-nucleus) scattering data as well as in this work.

First, the peaking approximation was used to calculate the elastic tail contribution. Proton and ^{12}C nuclear form factor parameters by Simon [24] and deVries [23], respectively, were used with the first order Born approximation to calculate the elastic cross sections. Although the peaking approximation with the first order Born approximation does not produce the exact spectrum of the elastic tail, it is sufficient to estimate its contribution because the contributions are very small in most of our spectra.

After the radiative tail was subtracted, the remaining quasi-elastic and inelastic scattering spectra were than unfolded using Slifer's fortran program upgraded from Whitney's [26]. The program includes standard Mo and Tsai's technique, as well as the interpolation and extrapolation method to calculate the cross sections for the unmeasured incident energies which are required by the formalism. The unfolded spectra have converged to the final ones with only a few iterative corrections, which are also implemented in the program.

Figure 3.20 shows the spectra of ^{4}He (preliminary), ^{12}C and ^{56}Fe before and after the radiative corrections. One can see that the cross sections around the quasi-elastic peaks are increased after the corrections. Beyond the quasi-elastic peak, the cross sections are generally decreased except for 15° high incident energy ($E > 2.4$ GeV) cases.

In addition to the corrections to the continuous spectra, the elastic cross section can also be corrected. It will be briefly discussed in the next section.

[§]Text in this paragraph is quoted from Ref. [34].

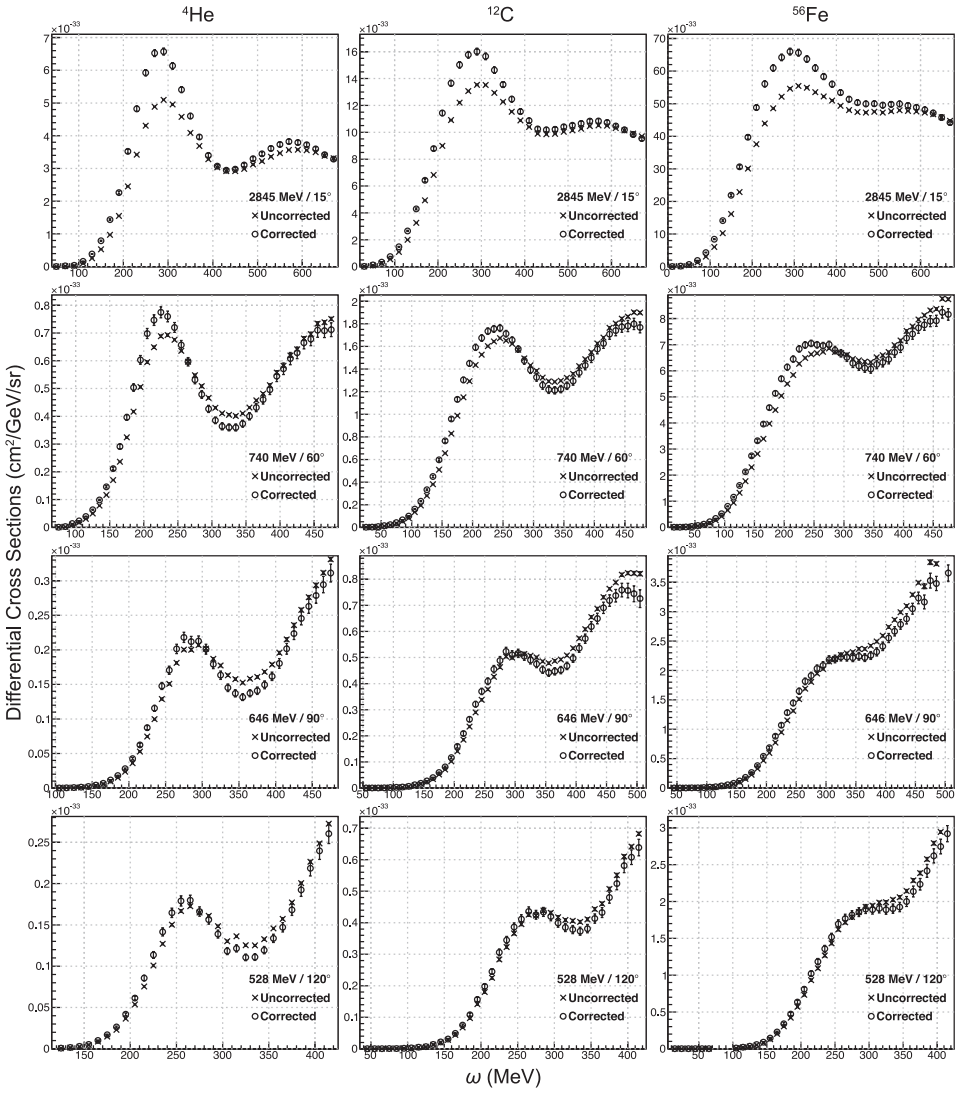

Figure 3.20: Radiative corrections for the continuous spectra (after subtracting the tails from elastic peaks) of ^{4}He(left, preliminary), ^{12}C(middle), ^{56}Fe(right) at 15°(top row), 60°(2nd from top), 90°(3rd), and 120°(bottom). Crosses are before the corrections, circles are corrected cross sections.

3.1.9 Additional note for fluid targets

As mentioned previously, in this thesis, ^{12}C and ^{56} data are mainly presented. But it would be interesting to compare the result with ^{4}He preliminary result. To present the preliminary results of ^{4}He and proton elastic data, additional analysis procedures for fluid targets are summarized here.

In addition to uncertainties applied to the solid foil target data, data of the liquid hydrogen and of the gaseous heilum-4 targets accompany more sources of uncertainties.

Density fluctuation

Local heating by beam current may result in decrease of the density of fluid targets which happens near the beam trajectory and, therefore, cannot be detected by sensor devices. This boiling effect can be studied by invesgating the proportionality between the normalized yield (or raw trigger rate) and the beam current.

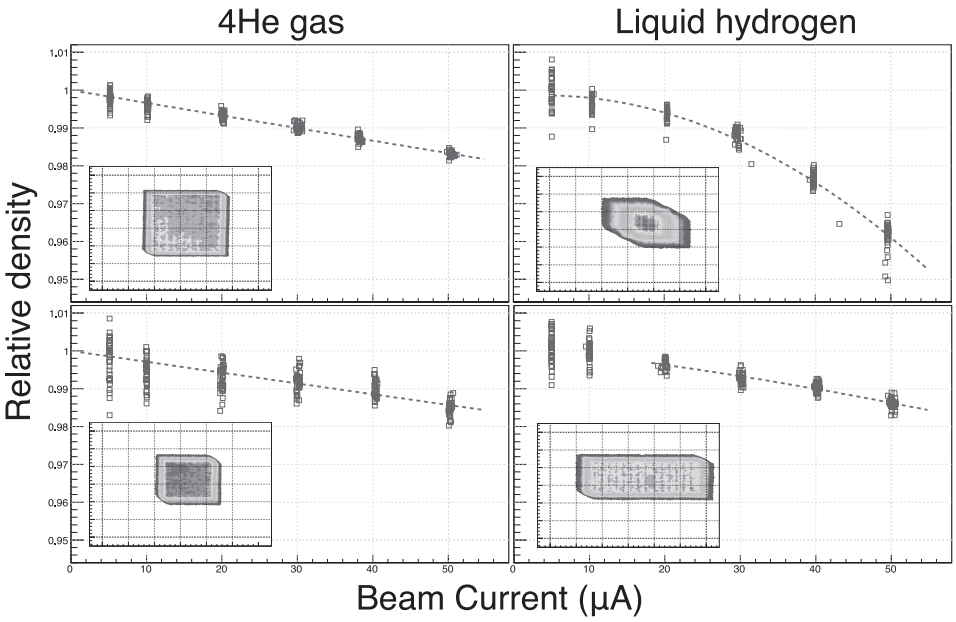

Figure 3.21: Density fluctuation (boiling effect) of fluid targets. the small panels inside show the rastered beam size on the target, one grid for 1 mm.

The density fluctuation depends on two parameters: current and size of the beam. As shown in Figure 3.21, the boiling effect is larger at higher beam

current, and at smaller beam size. And it is interesting to see the difference between the two targets: the density of gaseous heilum drops almost linearly with the beam current, while the density of the liquid hydrogen target shows a change of slope at around 20 μA. Correction for the boiling effect was always less than 5%.

Acceptance

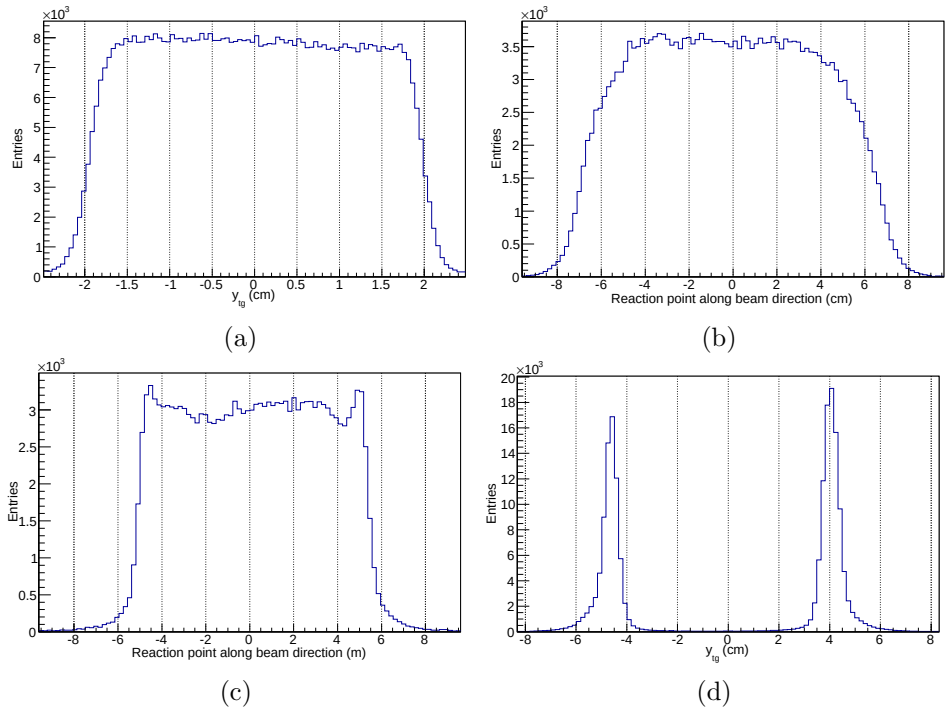

(a) (b) (c) (d)

Figure 3.22: Reconstructed fluid target spectra. (a) $y_{\rm tg}$ of the liquid hydrogen target at 15°. 15 cm length is project to ∼3.9 cm on the spectrometer. Most electrons are in the spectrometer acceptance. Contribution from the target windows is hardly seen because the elastic scattering yield is dominant. (b) $z_{\rm react}$ of same target, at 60°. The events beyond the HRS acceptance ($\sim \pm 5$ cm) are not reconstructed very well. (c) $z_{\rm react}$ of 10.4 cm length ^{4}He target at 60°. Window contribution is seen at each end. (d) $y_{\rm tg}$ of 10 cm dummy foil target at 60°. The projected distance between the two foils on the HRS y-axis should be ∼8.8 cm.

The fluid targets have finite lengths, helium 10 cm, hydrogen 15 cm. At 15 degrees, the projected lengths onto the spectrometer are about 2.6 and 3.9 cm, respectively, which are in the acceptance. Most electrons survive and are contributed to the spectra (Figure 3.22a). However, at the other angles, where the projected lengths are 8.7, 13 cm (60, 120°), and 10, 15 cm (90 degrees), a number of electrons scattered far from the target center may go out of the spectrometer acceptance. Furthermore, the optics elements are not well optimized for the acceptance edge (Figure 3.22b).In short, acceptance for the fluid targets is different from the one for a single foil target. The best way to deal with it should be to use a Monte Carlo simulation, but it was not used for the preliminary result shown in this work. Instead, events in $|z_{\rm react}|$ <3.5 cm were chosen for the backward angle data, in order to maximize the statistics and to minimize loss/fluctuation in the acceptance.

Container and target length

By cutting $|z_{\rm react}| > 3.5$ cm events, most electrons scattered from the target windows were eliminated for the backward angle (60, 90 and 120 degrees) data. But for 15 degrees, because the resolution in y_{tg} is amplified by projection on the beam direction, it is better to use whole spectra and to subract the contribution from the target window. 10 cm dummy target spectra were used to estimate the window contributions. The dummy target and the fluid target container are different by thicknesses (see Table 2.1), the materials are slightly different (Al6061 vs. Al7075), and the incident energies at the downstream foil (target end window) can be different due to more energy loss in the fluid between the windows. Ignoring small difference in the beam energies, the yields of the two should be proportional to each other, and the proportionality should come from no other than the target thicknesses (or in other words, the numbers of protons in the targets). The ratio of the numbers of protons can be estimated using material data sheet [20]. The calculated ratio of the number of protons in the dummy target to that in ^{4}He target windows is ∼3.5. It can be checked with super-elastic (SE) spectrum, which is the spectrum located at E' higher than the elastic peak of ^{4}He. Although the super-elastic spectrum is very narrow and it can vary significantly with momentum transfer change, the result (3.4±0.8) agreed with the calculated number. A wider range of super-elastic spectrum is available for the hydrogen target, because elastic peak is located at E' much lower than that of ^{4}He. The ratio of the normalized yield of dummy to that of hydrogen target at SE was found to be 7.0±0.7. Using these numbers, in the cross section spectrum of production data, the contribution of the helium

target windows was found to be at most ∼10% at around the quasi-elastic peak. For hydrogen elastic spectrum, less than a few percent's contribution of the windows was found.

The lengths of the target at backward angles was also calculated using dummy the spectra. One dummy foil is separated from the other physically by 10 cm in the beam direction, but a reconstructed distance can be different from the actual distance, due to poor track reconstruction at the edge of the spectrometer acceptance. The relative distance between the two foil in the $y_{\rm tg}$ spectrum (Figure 3.22d) was compared to the actual projected length (10 cm$\times \sin\theta_0$; θ_0 is the spectrometer centeral angle). And then the ratio of the two was given as a correction for the selected target length defined by a cut ($\pm$3.5 cm):

$$\begin{aligned}\text{(Target length)} =&\text{(Reconstructed 7 cm length in cut)}\\ &\times \frac{\text{(10 cm)} \times \sin\theta_0}{\text{(Reconstruncted distance in } y_{\rm tg})}.\end{aligned}$$

3.2 Elastic Cross Sections and Absolute Normarlization

After all the calibrations of hardwares and the corrections at raw levels, elastic scattering cross sections were compared to the existing data to have the absolute normalization factors. The normalization factors may come from the imperfect knowledge of the solid angle. Especially, since two different sets of optics elements were used to analyze the trajectories: one for scattered energy above 450 MeV, the other for below 450 MeV which shows worse resolution, difference between them may exist.

^{12}C elastic scattering data were taken with several low beam energies (400, 646, 740, 1260 MeV) at several forward angles, and proton elastic data were taken at all the kinematic settings except for at 90° with 528 MeV beam energy. The measured ^{12}C form factors were compared to the form factors calculated using a phase-shift code[25] which used the charge distribution parameters from Ref. [23]. The result is in Fig. 3.23.

The radiative corrections to the elastic peaks were calculated using Mo and Tsai's formula [21]. The E' cuts were chosen to count only the elastic events excluding any exited states of ^{12}C or pion threshold for proton. of the target nucleus–$\Delta E = (E'_{\rm peak} - E'_{\rm cut})/E'_{\rm peak}$ were around 0.6-1% for ^{12}C, and around 3% for proton. The resulting corrections (e^{δ} defined in [21]) were ranging 0.65-0.8.

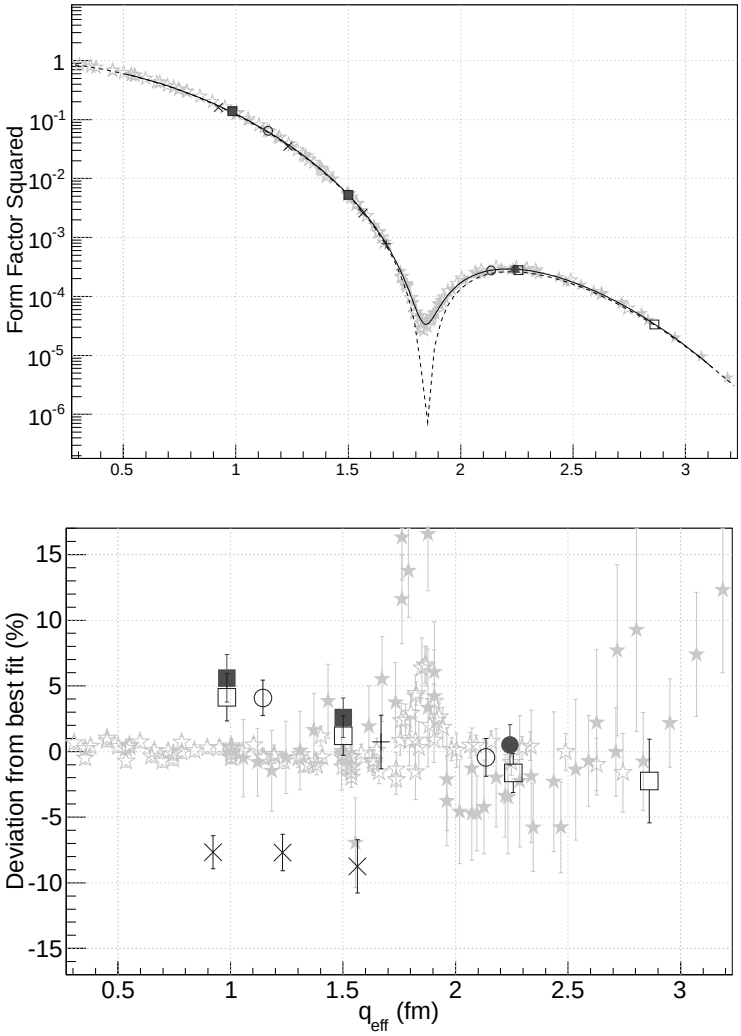

Figure 3.23: ^{12}C elastic form factor (top), deviation of data from the best fit (bottom). Error bars includes both statistical and systematic uncertainties. Solid curve in the left is from phase shift calculation, and dashed curve is from Born approximation. Gray stars are existing data from McCarthy *et al* [27] and from Reuter *et al* [28]. Three crosses($\times$) are from E =400 MeV data for which the low energy optics elements set is used, the others (circles: 646 MeV at 20°, 38°, rectangles: 740 MeV at 15°, 23°, 35°, 45°, and right cross : 1260 MeV at 15°) are analysed with the high energy optics. 740 MeV, 15° data and 646 MeV, 20° data are not quite reliable due to their VDC efficiencies; the raw trigger rate were too high. (Filled symbols are for HRS-R result.)

Figure 3.23 shows the resulting elastic form factor of ^{12}C. All the systematic uncertainties described previously were included in the error bars. In addition, the uncertainty of 0.2 mrad in the scattering angle was also added. Statistical errors are negligible except for three points at high $q_{\rm eff}$[¶]. The results using high energy optics elements were in good agreement with existing data and with the phase-shift calculation: a average deviation of $+1.1\pm0.9\%$ was found and used for absolute normalization. And the results with low energy optics elements (three crosses) formed a group which is deviated by $9.3\pm0.9\%$ lower than the high energy optics elements' group. This number (9.3%) defined the relative normalization between the two sets of results from different optics elements, and 0.9% its uncertainty. Almost same result was found in the preliminary result of the proton elastic cross sections (Figure 3.24). While the uncertainty in the relative normalization is one of the major sources of error in the final response functions and in the Coulomb Sum, the uncertainty in the absolute normlization (0.9%) remained constant till the end.

Uncertainty in scattering angle

Uncertainty in scattering angle may come from the misalignment of the spectometer (error in θ_0) and from the error in track ($\theta_{\rm tg}$, $\phi_{\rm tg}$) reconstruction (see Eq.2.3). The misalignment of the spectrometer was less than 0.2 mrad as shown in Table 2.3, however, the precision of the survey is reported as 0.6 mrad [9]. And a large portion of data were taken at angles without the survey. Furthermore, the angular resolution of the spectrometer is no better than 0.5 mrad (horizontal), 1.0 mrad (vertical). It is, however, too cruel to assign these resolutions as the uncertainty in the scattering angle. Instead, it is reasonable to calculate the uncertainty from the absolute positions of the eC/eP elastic peaks and from the absoulte value of the elastic cross sections. Especially, the elastic cross sections of ^{12}C is very sensitive to the scattering angle change; for example, 0.5 mrad's change of scattering angle results in 1-5% change of the cross sections. But the fluctuation of the measured ^{12}C form factors is about 1%, when the uncertainties from other sources were taken into account. Uncertainty of 0.2 mrad, which is slightly larger than the maximum misalignment of HRS, is enough to describe such fluctuation.

[¶] $q_{\rm eff} = q(1 + \frac{4}{3}Z\alpha/r_{\rm rms}E)$, where q is the magnitude of 4-momentum transfer [27].

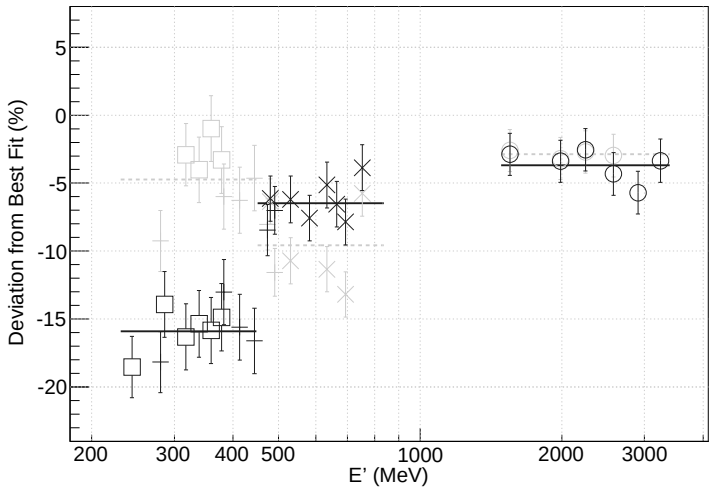

Figure 3.24: (Preliminary) Proton elastic form factor deviation from Simon's fit. Light gray symbol is for R-HRS result. The results can be split into three groups : 15 degrees' cross sections (circles) of which the whole length of target was in the spectrometer acceptance, the second group is of 60 (cross) and 90 (+) degrees' data where the high energy optics set was applied with length cut, and the last group is of 90 and 120 (rectangle) degrees data for which the low energy optics set is used. The relative deviation between the second and the third group is close to that of ^{12}C result.

3.3 Summary of Systematic Uncertainties

Uncertainties in the cross sections are summarized in Table 3.3. At 15°, relatively low tracking efficiency, caused by high trigger rate, is one of the main source. At the other angles at low scattered energy, where the pion contamination dominates the raw spectrum, uncertainty in background elimination is the one. At all angles, radiative corrections, acceptance and reltive normalization contribute high portion of uncertainty.

The total systematic uncertainty was calculated by quadratic sum of each constribution. The uncertainties at around quasi-elastic peaks are about 1.5% at 15° and about 2.5% at backward angle and low energy ($E' < 450$ MeV).

The uncertainty of the longitudinal and transverse response functions can be estimated when the Rosenbluth separation is performed only with two angle data [33]. But, in this work, four angle data were used and the separation was done with fitting. Therefore, the uncertainty of the response

functions with four angle separation became smaller than that with two angle separation, but it is not easily calculated by a simple formula.

Name of source	Uncertainty	Uncertainty in $d\sigma/d\Omega d\omega$ (%)			
		15°	60°	90°	120°
Incident energy	0.05-0.15 %	0.1	0.1-0.2	0.1-0.3	0.1-0.3
Scattering angle	0.2 mrad	0.31	0.08	0.06	0.06
Scattered energy	0.05-0.2 %	0.1	0.1-0.3	0.1-0.4	0.1-0.4
Beam charge	0.3 %		0.3		
Detector deadtime	10 %	0-0.1		0	
Computer deadtime	0.2 %		0.2		
Tracking inefficiency	5 %	<0.5		<0.1	
Cerenkov detector					
e^- detection efficiency	<0.05 %		<0.05		
π^- rejection inefficiency	0.3 %	<0.1		0-1.5	
Tail from elastic peak	10 %	0-1	0-0.5	0-0.3	0-0.3
Background from e^+e^- pair	5 %	0	<0.5	<1.5	<2.0
Center-of-bin correction		0.3	0.1	<0.1	<0.1
Acceptance	0.8-1.6 %	0.8		0.8-1.6	
Radiative corrections	1.0 %		1.0		
Normalization	0.9 %	0		0-0.9	
Fluid target density		<0.2		<0.5	
Fluid target length		<0.5		1.5	
Total relative uncertainty (solid target)		<1.8	<2.7	<3.0	<3.3

Table 3.3: Summary of systematic uncertainties in the differential cross sections

Chapter 4

ANALYSIS PART II

4.1 Interpolation

To derive the Coulomb Sum, as mentioned in the introduction, the longitudinal response function should be integrated along a constant $|\mathbf{q}_{\text{eff}}|$ value. However, the cross sections were measured with constant incident energies. In order to separate R_L and R_T at a constant $|\mathbf{q}_{\text{eff}}|$, interpolation in ($\omega$, $|\mathbf{q}_{\text{eff}}|$) plane is necessary. The interpolation to a specific $|\mathbf{q}_{\text{eff}}|$ and ω was done by follwing paths that passed through the corresponding features in each spectrum, i.e. peak to peak, dip to dip, for different incident energies. The paths can be chosen among several constants: ω/E, $\omega + Q^2/2M$, invariant mass W, and the quasi-elastic scaling variable y^* defined by:

$$\omega + M_A = \left(y^2 + 2y|\mathbf{q}| + M^2 + \mathbf{q}^2\right)^{1/2} + \left(y^2 + M_{A-1}^2\right)^{1/2} \tag{4.1}$$

where M_A is the mass of the target nucleus, M is the nucleon mass and M_{A-1} is the mass of the nucleus with $A-1$ nucleons. All these variables align the quasi-elastic peaks well. In this work, y was used up to around quasi-elastic peaks ($y = 0$). And for ω beyond quasi-elastic peak, $\omega - Q^2/2M$ was used (see Reference [30] and Figure 4.1. The choice of variables was also for the maximum use of measured data. The interpolation, resultingly, is two dimensional interpolation. Therefore, the result should be independent from the variables chosen. And actually, the differences in y and $\omega - Q^2/2M$ interpolated results were not considerable but were added to the systematic uncertainty.

*Scaling property is also of interest in quasi-elastic scattering study, as quoted in the introduction [2].

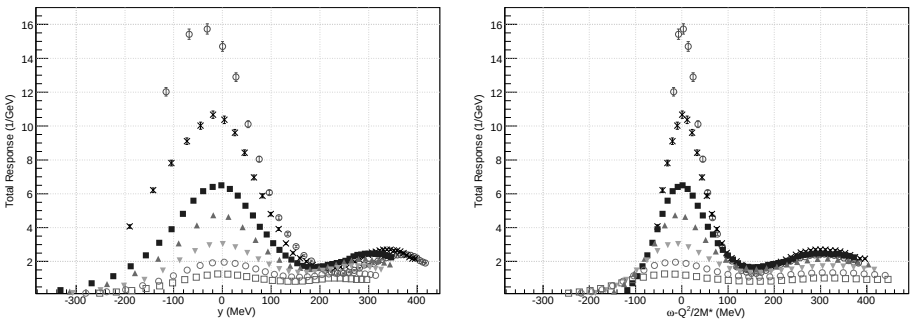

Figure 4.1: Total responses of ^{4}He at 15 degrees aligned in constant y (left) and in constant $\omega - Q^2/2M$ (right). Both variables align the quasi-elastic peak well; y is better below the peak, while $\omega - Q^2/2M$ aligns the dips and inelastic peaks better.

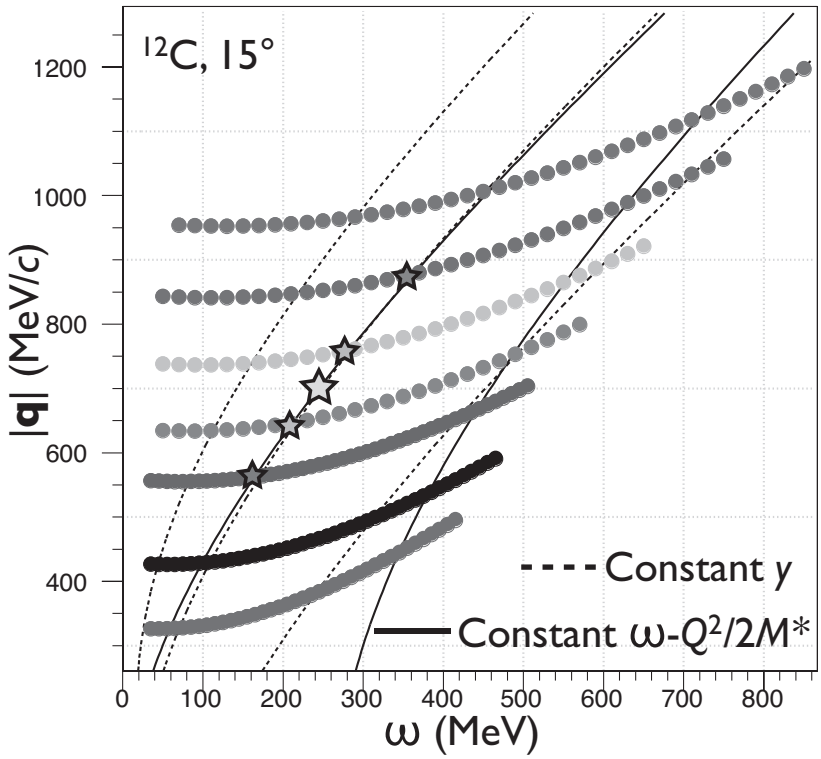

Figure 4.2: Measured (ω, $|\mathbf{q}|$) data points (filled circle), constant y lines (dashed), and constant $\omega - Q^2/2M$ lines (solid). For a given (ω, $|\mathbf{q}|$) (big star), y and $\omega - Q^2/2M$ are calculated. At the same y and $\omega - Q^2/2M$, the total responses are interpolated using cubic splines along ω in the neighboring spectra (small stars). Then the response function at the big star is interpolated using the second order polynomials of $|\mathbf{q}|$ consisting of three of those neighboring points.

The interpolation have been performed in the following order (Figure 4.2):

1. For a fixed (ω, $|\mathbf{q}|$) point, calculating y and $\omega - Q^2/2M$. (Let's say this point is X.)

2. Finding ω's with same y and same $\omega - Q^2/2M$ points in the neighboring measured spectra. (1-2-X-3-4, where 1, 2, 3 and 4 are the points in the neighboring measured spectra)

3. In a measured spectrum, the total response function is interpolated using cubic spline along ω.

4. The total response function at the given point is interpolated using three-point parabola of $|\mathbf{q}|$ lying on those neighboring measured points (1-2-X-3 or 2-3-X-4). The difference between the results from two parabola is taken as systematic uncertainty. Interpolation by higher order polynomials is excluded because they do not improve any result but amplify small fluctuations in the data. The typical uncertainty is at most 1%. For the point where only one neighboring measured spectrum is available at low or high $|\mathbf{q}|$ side, 1% of uncertainty is added.

The interpolated total response functions of ^{12}C in (ω, $|\mathbf{q}|$) plane are shown in Figure 4.3. The statistical and the systematic uncertainties are separately added to the central values and then interpolated using same method, to estimate the uncertainties in the interpolated spectra.

4.2 LT Separation

To separate R_L and R_T at a given (ω, $|\mathbf{q}|$), one can use the plot of εR versus ε. The data point for each angle should lie on a straight line, the slope and y-intercept of which are $(Q^4/\mathbf{q}^4)R_L$ and $(Q^2/2\mathbf{q}^2)R_T$ respectively, as mentioned in the introduction.

$$\varepsilon R = \varepsilon \frac{\sigma}{\sigma_{\mathrm{M}}} = \varepsilon \frac{Q^4}{\mathbf{q}^4} R_L + \frac{Q^2}{2\mathbf{q}^2} R_T \tag{4.2}$$

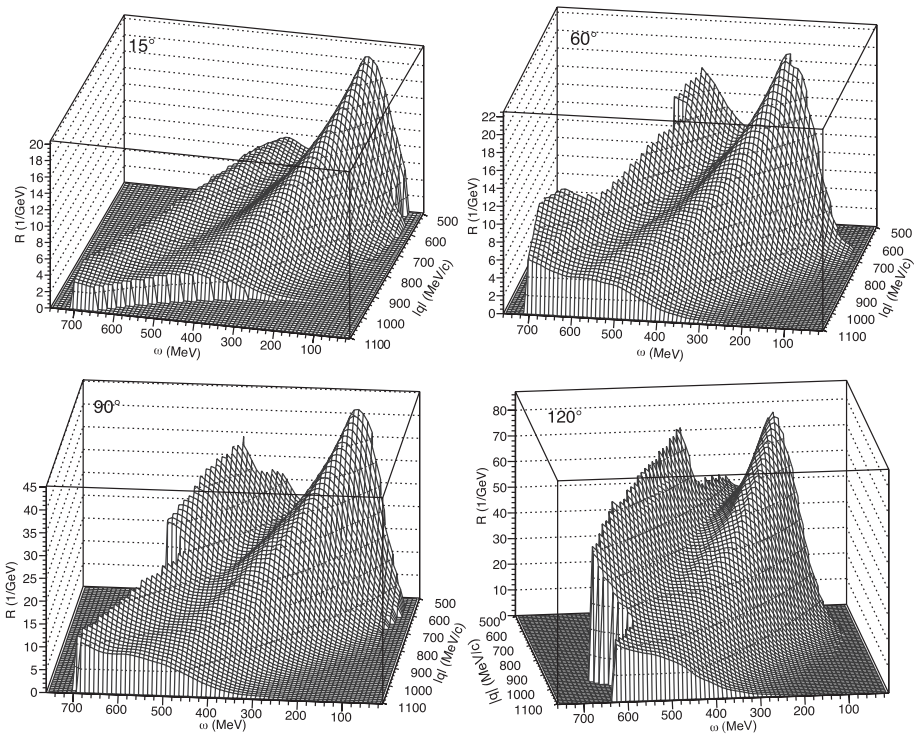

Figure 4.3: Interpolated total response functions of ^{12}C

Figure 4.4 shows a side view of the ^{12}C interpolated total response functions at 15°. It is interesting that while the height of the quasi-elasic peak smoothly decreases as $|\mathbf{q}|$ grows, the heights of the dip and of Δ-resonance peak show broad maxima at $|\mathbf{q}| \sim 550$ MeV/c then decrease. The similar behavior has been observed at all angles, and so for the other targets.

Figure 4.5 shows an example of the separation. First, it should be noted that since the separation is done by linear fitting of more than two data points, the size of an error bar of a point can change the result, which means that separated treatment of the statistical and systematic uncertainties is no more possible. Therefore, the total uncertainty of a data point was calculated by adding the statistical and systematic uncertainties in quadrature. The separation was performed for all the separable (ω, $|\mathbf{q}|$) data points, i.e. for the points where two or more angles' data existed. The errors in R_L and R_T were from the fitting results.

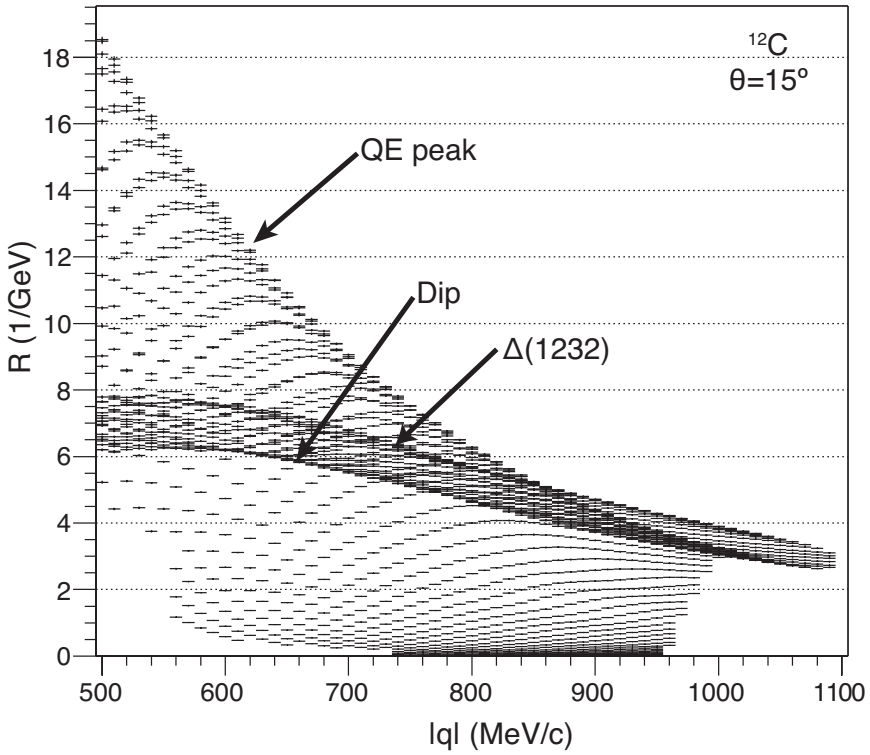

Figure 4.4: A side view of the interpolated total response functions of ^{12}C at $\theta = 15°$. For 3-dimensional view, see Figure 4.3.

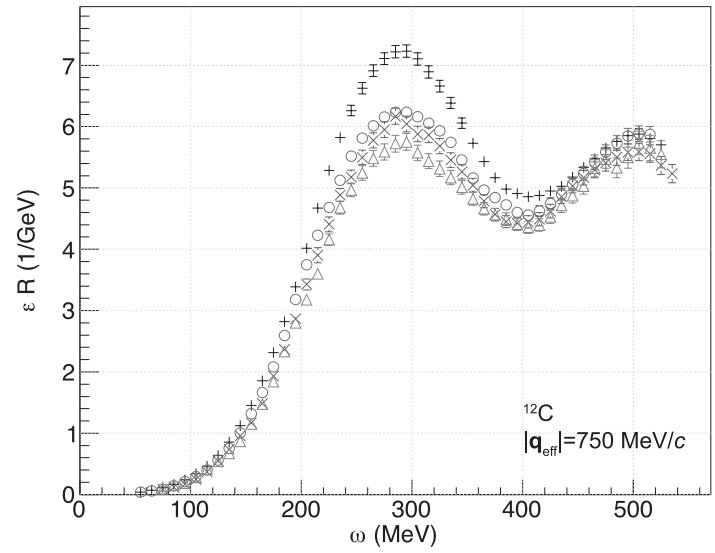

(a)

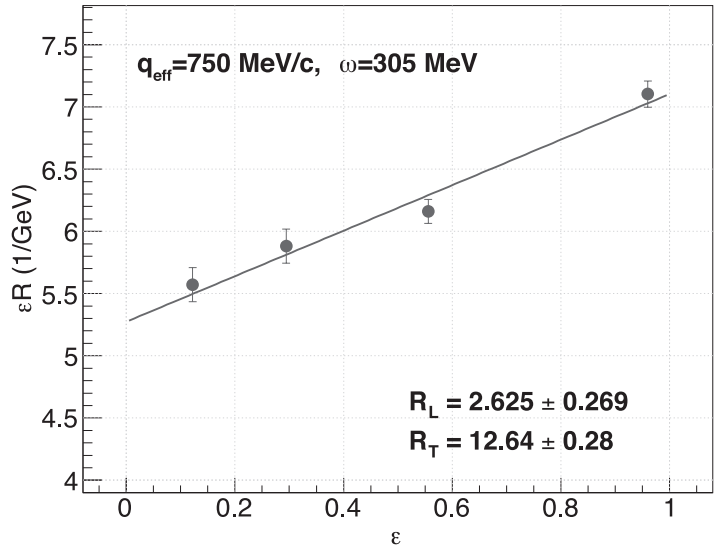

(b)

Figure 4.5: An example of L/T separation. (a) εR of ^{12}C at $|\mathbf{q}_{\rm eff}|$ = 750 MeV/c; right cross is for 15° data, circle 60°, cross 90°, and triangle 120°. The data are separable from ω =75 MeV to ω =525 MeV for this case. (b) An example of LT separation at ω=305 MeV. 4 points are fitted to a straight line; R_L is calculated from its slope and R_T from its y intercept. The error in each response function is the fitting result.

Coulomb correction

Correction for Coulomb distortion involves slight moving of the measured total response functions (R) from the measured kinematic points to the effective ones as described in the introduction:

$$R(|\mathbf{q}|, \omega) \longrightarrow R(|\mathbf{q}_{\rm eff}|, \omega) \tag{4.3}$$

without changing their amplitudes. The values of the average effective Coulomb potential ($\overline{V}_{\rm C}$) of ^{12}C and of ^{56}Fe are taken from Reference [5].

$$\overline{V}_{\rm C}(^{12}{\rm C}) \;=\; -3.1 \pm 0.25 \text{ MeV},\; \overline{V}_{\rm C}(^{56}{\rm Fe}) \;=\; -8.9 \pm 0.7 \text{ MeV} \tag{4.4}$$

As seen in Figure 4.6, the change from $|\mathbf{q}|$ to $|\mathbf{q}_{\rm eff}|$ is larger for the backward angle kinematics.

The resulting response functions distributed in (ω, $|\mathbf{q}_{\rm eff}|$) are different from the ones in (ω, $|\mathbf{q}|$). From Figure 4.4, one can imagine that the correction moves all the point slightly, by the amount calculated from Eq. 1.6, in $+|q|$ direction. Generally, the total response functions increase as $|\mathbf{q}|$ is corrected to $|\mathbf{q}_{\rm eff}|$. Exceptions are for the region around the dip and the inelastic peak at the lowest $|\mathbf{q}|$ range. Slight decrease after the correction was found for this region.

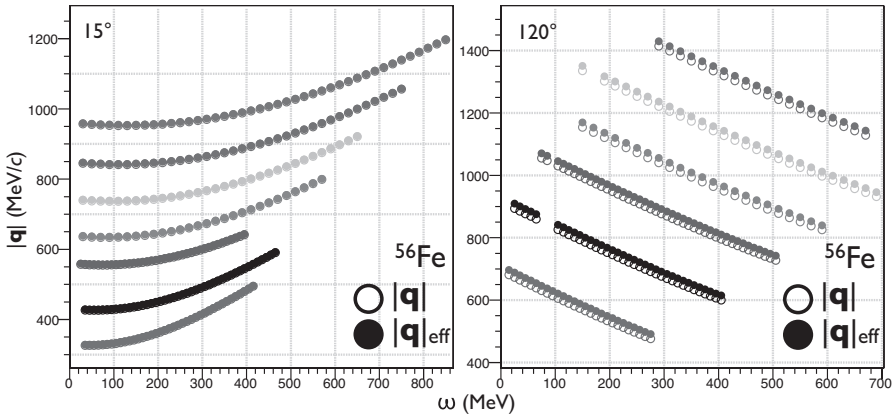

Figure 4.6: Coulomb correction for ^{56}Fe data at 15° (left) and at 120° (right). A response function at a measured kinematic point (ω, $|\mathbf{q}|$), denoted by open circle, should move to the effective kinematic point (ω, $|\mathbf{q}_{\rm eff}|$), filled circle. The difference between $|\mathbf{q}|$ and $|\mathbf{q}_{\rm eff}|$ is so small for 15° that it can hardly be seen in this figure, while for 120° the difference is noticeable.

Figures 4.7 and 4.8 show the comparison of the total response functions between at $|\mathbf{q}| = 750$ MeV/c and at $|\mathbf{q}_{\rm eff}|$=750 MeV/c. One can see that the correction affect more on the backward scattering angles: at 15 degrees the difference is about a few percent, while at 120 degrees, several tens of percent at low ω side, and a few to ten percent at high ω. At all angles, the difference between the two is large at the rise of quasi-elastic peak and decreases as ω approaches to the dip.

This different correction to each kinematic point affects the LT seperation result considerably. In Figure 4.7, it is clearly seen that the differences between the response functions of forward and of backward angles become smaller after the correction; and therefore, R_L becomes smaller while R_T becomes larger. Examples are shown in Figure 4.9. The corrected R_L at around the quasi-elastic peak is $\sim$10% smaller than the uncorrected one, while R_T increases $\sim$5% after the correction. At higher ω around inelastic peak, the correction for R_L is much larger, a few times ten percent, than the uncorrected, while increase in R_T is still as small as 6%.

Coulomb Sum, as well as R_L, is suppressed by the correction. The effect of correction gets larger as $|\mathbf{q}|$ grows.[†]

[†]From here, only the corrected result will be shown. And $\mathbf{q}$ is $\mathbf{q}_{\rm eff}$ without further notice.

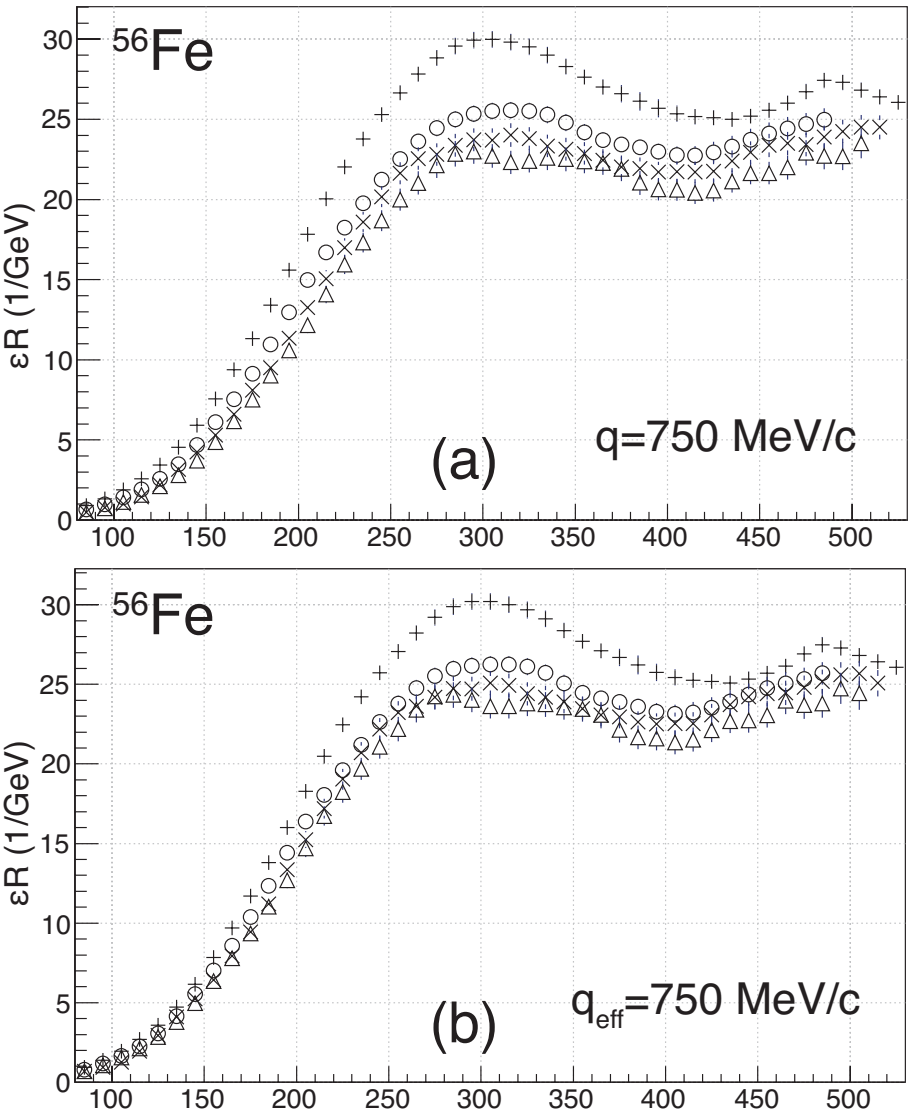

Figure 4.7: The total response functions multiplied by ε (a) without Coulomb correction, $R(|\mathbf{q}|, \omega)$, and with correction, $R(|\mathbf{q}_{\rm eff}|, \omega)$ at 750 MeV/c. Right cross is 15°, circle 60°, cross 90°, and triangle 120°.

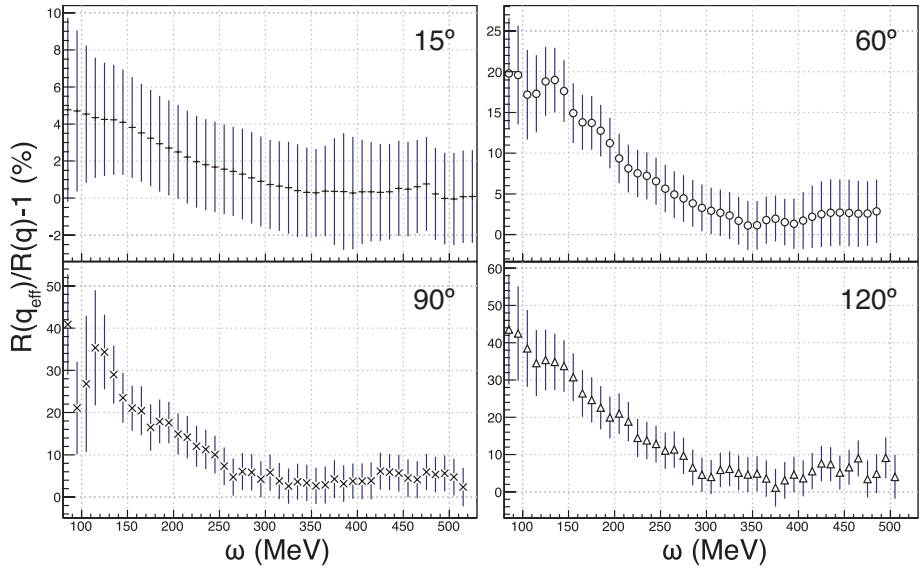

Figure 4.8: Difference between $R(|\mathbf{q}| = 750$ MeV/$c)$ and $R(|\mathbf{q}_{\rm eff}| = 750$ MeV/$c)$ of ^{56}Fe.

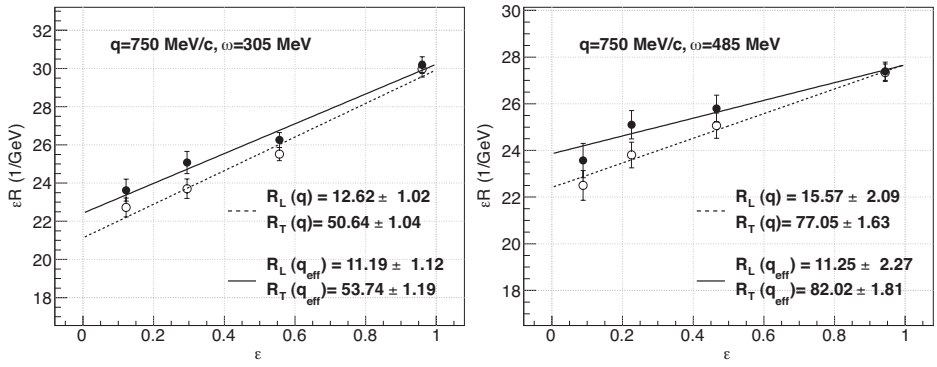

(a) (b)

Figure 4.9: Examples of LT separation of ^{56}Fe at $|\mathbf{q}|$=750 MeV/c (empty circle) $|\mathbf{q}_{\rm eff}|$=750 MeV/c (filled circle); (a) ω=305 MeV at the quasi-elastic peak, (b) ω=485 MeV around inelastic (Δ) peak.

Chapter 5

RESULTS

5.1 Cross Sections

The differential cross sections of ^{12}C and ^{56}Fe are shown in Figures 5.2-5.9. Error bars include both statistical and systematic errors presented in Table 3.3. Some error bars in high energy loss with high E at backward angles (90 and 120 degrees) are quite large due to statistics and large background contributions. But most of the points with those large error bars ($\sim 5\%$) are excluded in the LT separation because they are generally out of range in ($|\mathbf{q}|$, ω) plane in times of interpolation.

At 15°, spectra at the lowest two incident energies (1260, 1646 MeV) have some missing parts of risings of the quasi-elastic peaks. It is due to excluding peaks from elastic scattering and nuclear excited states. Since $|\mathbf{q}|$ of those points are at below 550 MeV/c, the LT separation in the desired range is not affected. For the other spectra, the elastic peaks and the peaks from exited states are barely observable. This is as expected as that the processes are almost free from Pauli blocking at $|\mathbf{q}| \gg 2k_f$.

One can also see that as the scattering angle becomes larger and as E grows, the spectra is dominated by inelastic process. The small contribution of quasi-elastic scattering makes it difficult to separate L/T in high $|\mathbf{q}|$.

Saclay data of ^{56}Fe [31] and of ^{4}He [30]* with $E = 400$ MeV, $\theta = 90°$ can be compared to the results of this work (Figure 5.1. Only these two sets have the same incident energy and scattering angle. For each target, the general shape–positions of the quasi-elastic peak and the dip– of the spectrum is in good agreement. However, while ^{4}He preliminary result is almost on top of the reference spectrum, ^{56}Fe result shows difference: Saclay cross sections

*The world quasi-elastic electron-nucleus scattering data are colleted in Ref. [32].

are lower by a few to ten percent, and even the error bars do not touch at high energy loss region.

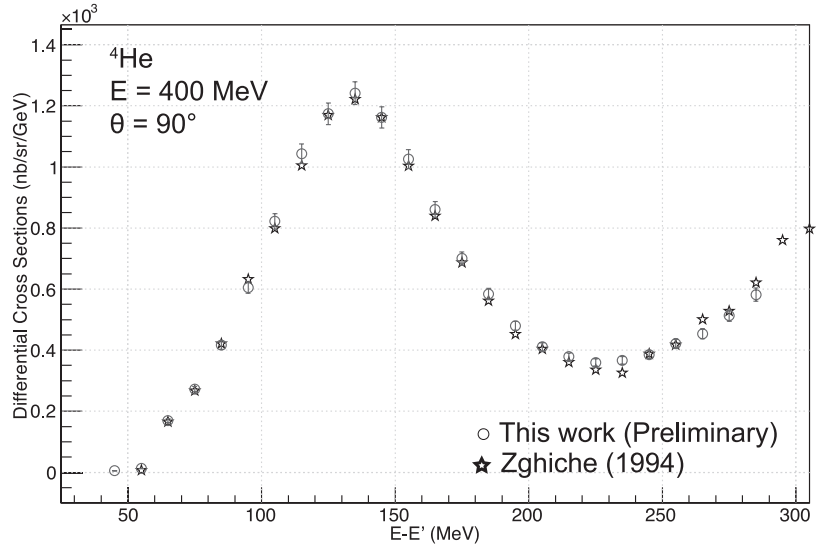

(a)

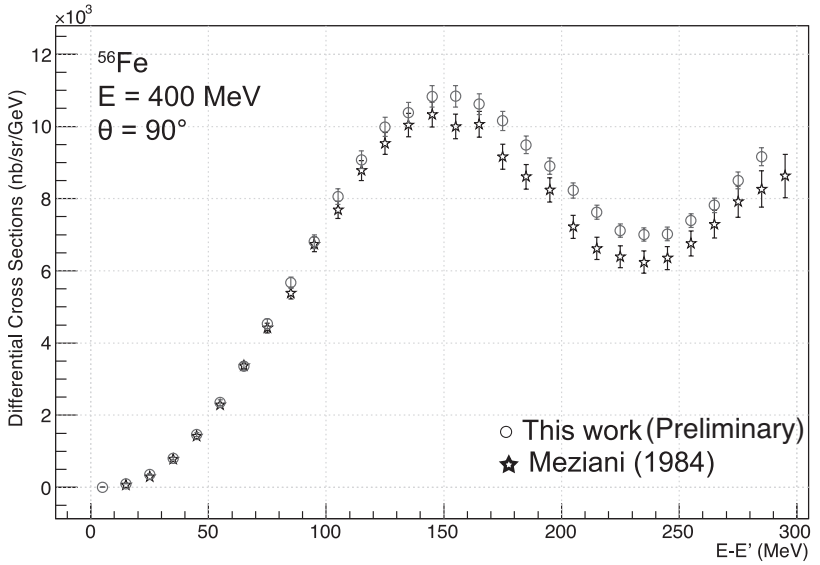

(b)

Figure 5.1: Differential cross sections of (a) ^{4}He and (b) ^{56}Fe, $E = 400$ MeV, $\theta = 90°$. Note that the two Saclay data were taken in separate experiments in different years.

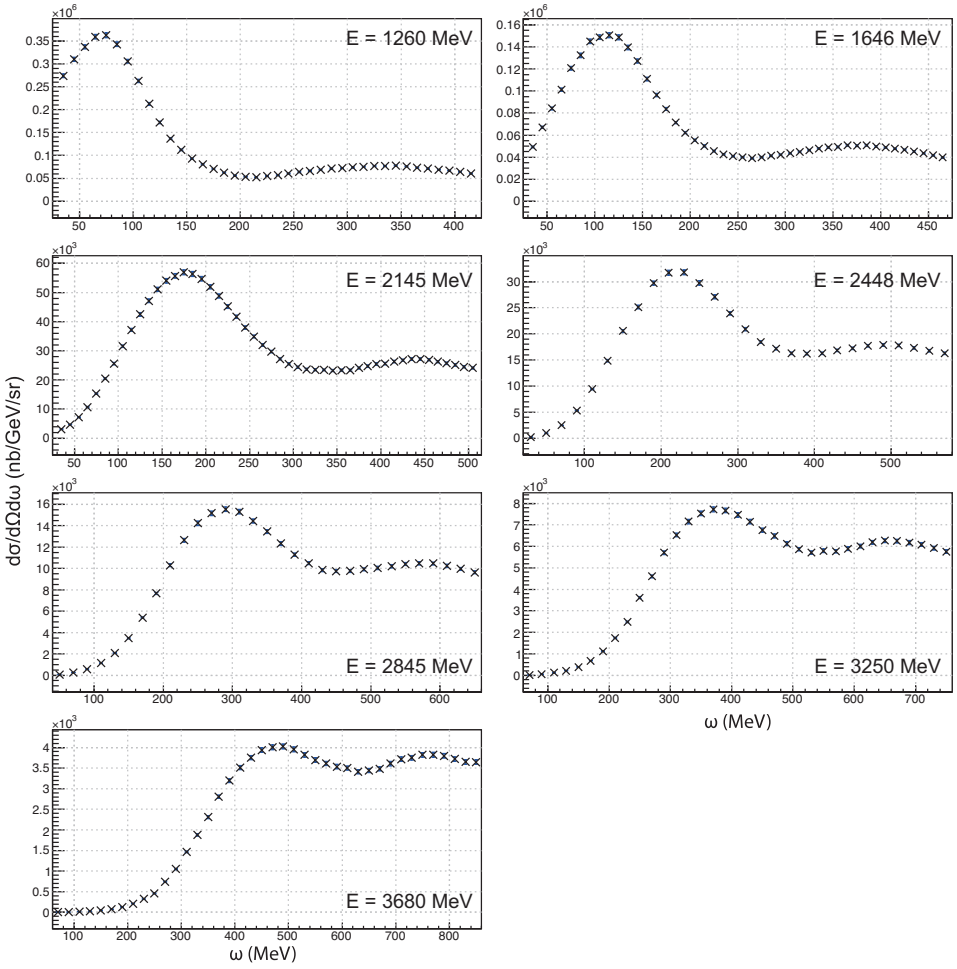

Figure 5.2: Differential cross sections of ^{12}C at $\theta = 15°$.

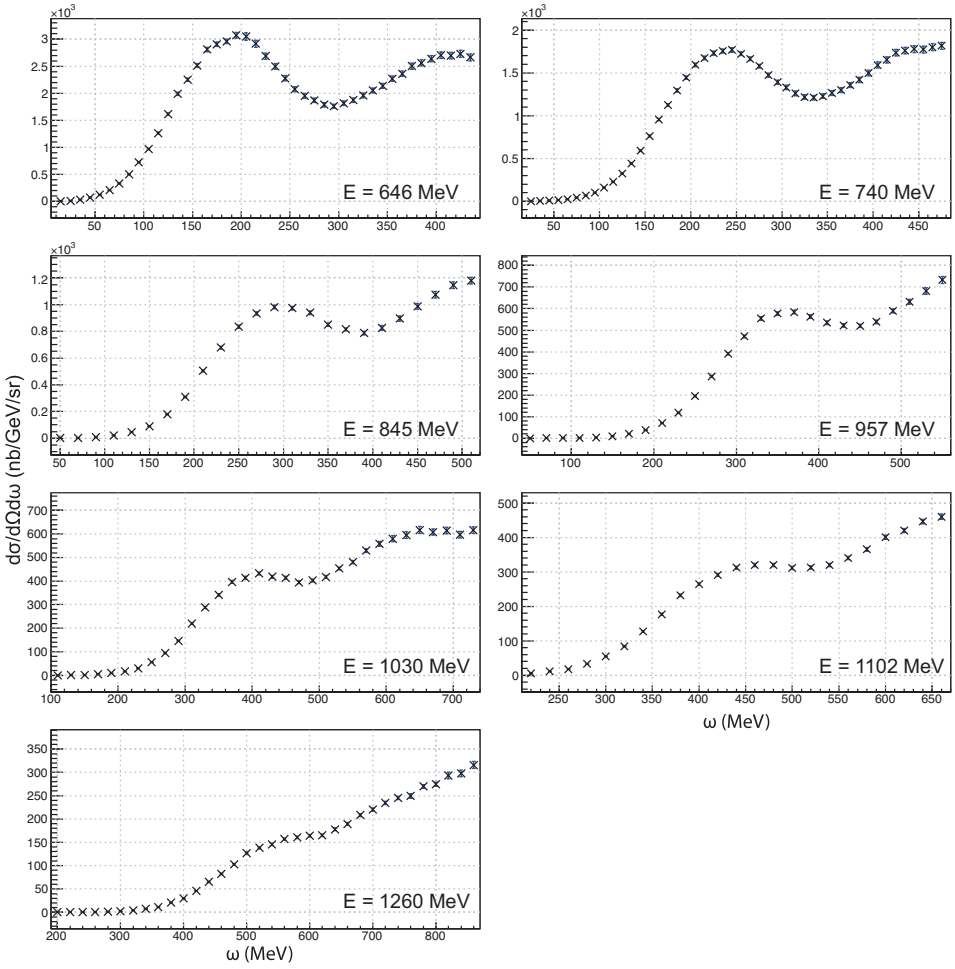

Figure 5.3: Differential cross sections of ^{12}C at $\theta = 60°$.

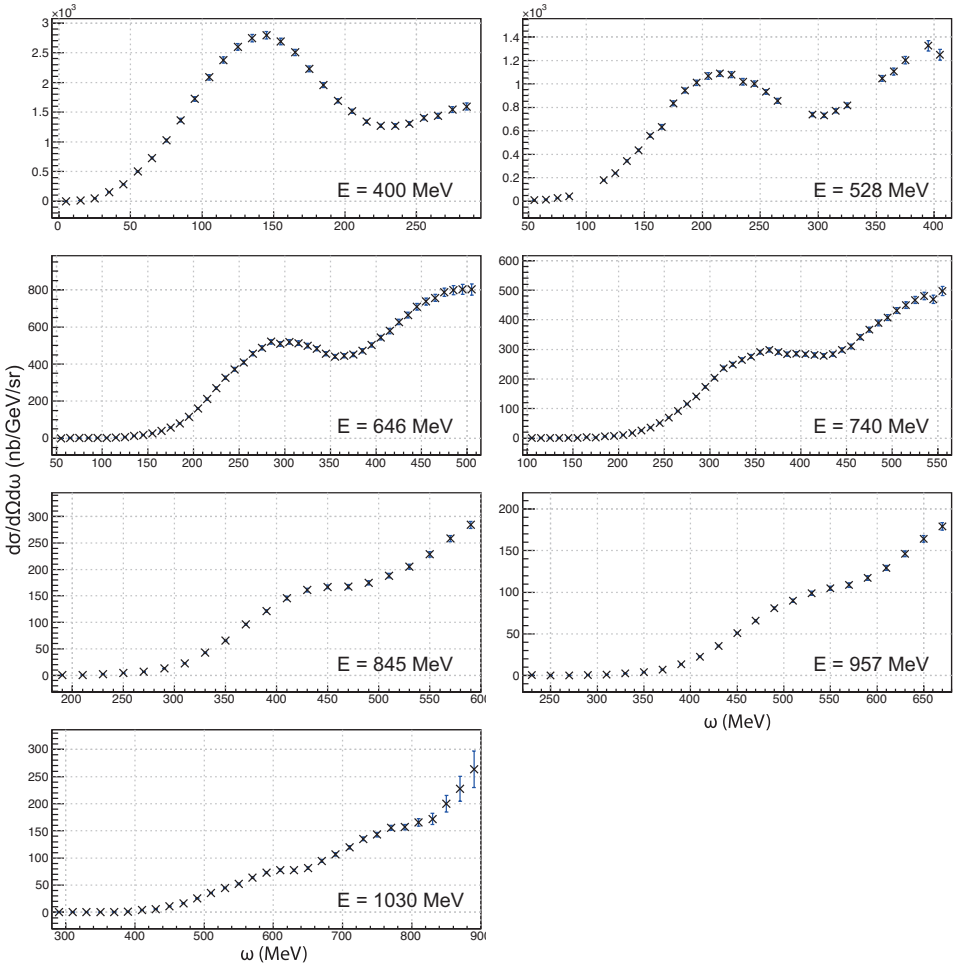

Figure 5.4: Differential cross sections of ^{12}C at $\theta = 90°$.

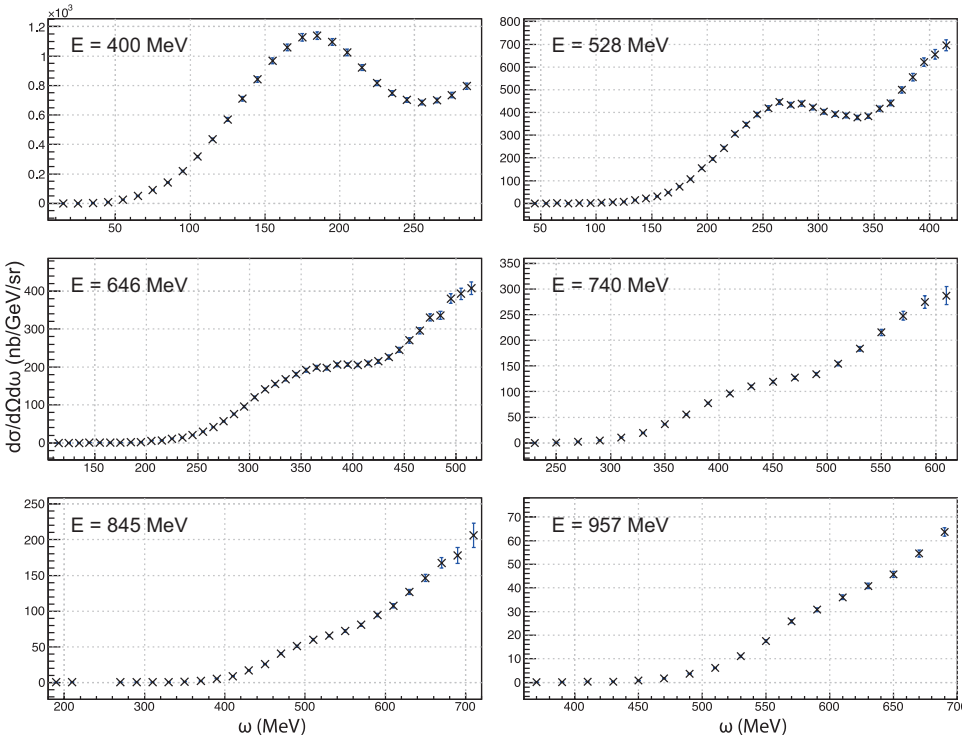

Figure 5.5: Differential cross sections of ^{12}C at $\theta = 120°$.

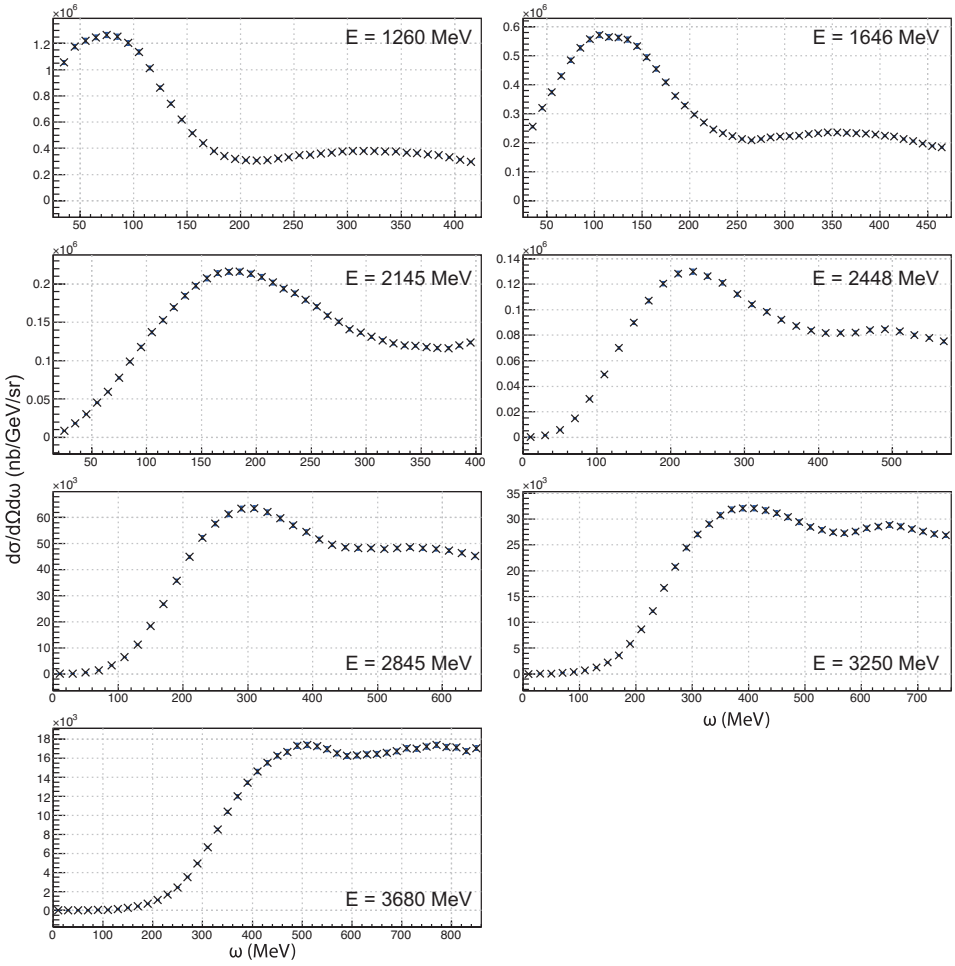

Figure 5.6: Differential cross sections of ^{56}Fe at $\theta = 15°$.

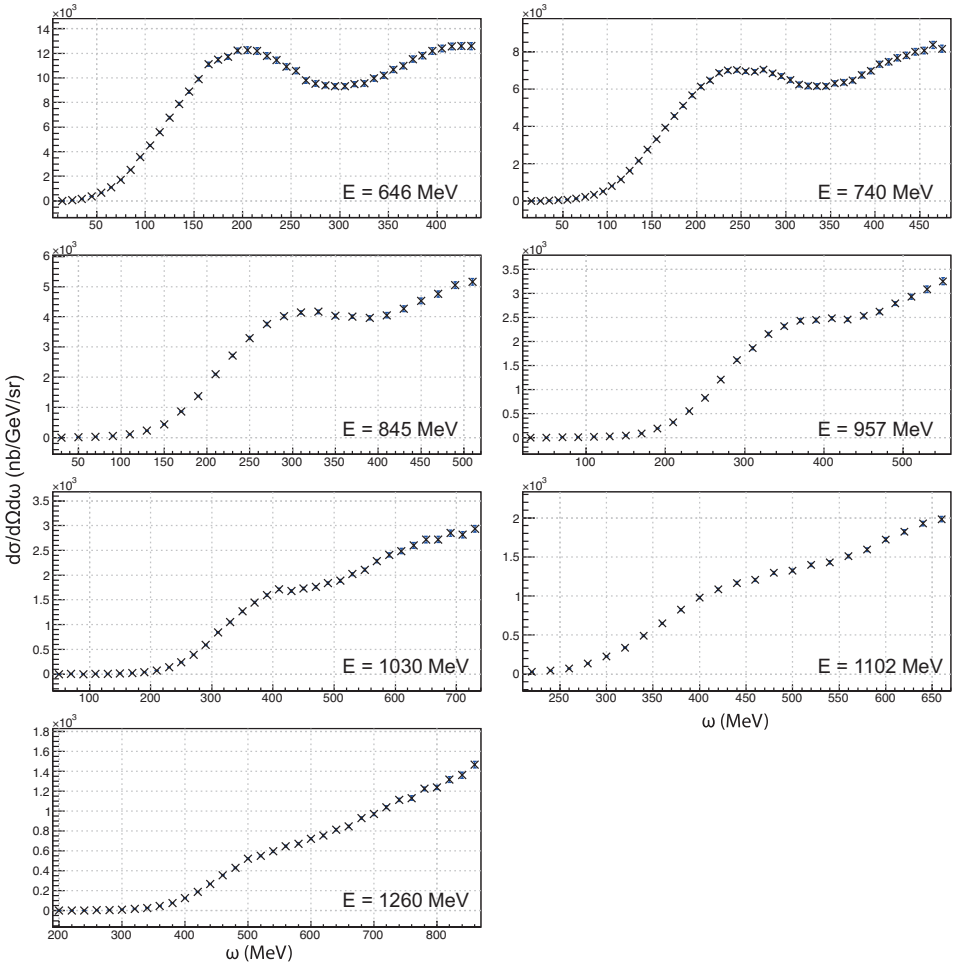

Figure 5.7: Differential cross sections of ^{56}Fe at $\theta = 60°$.

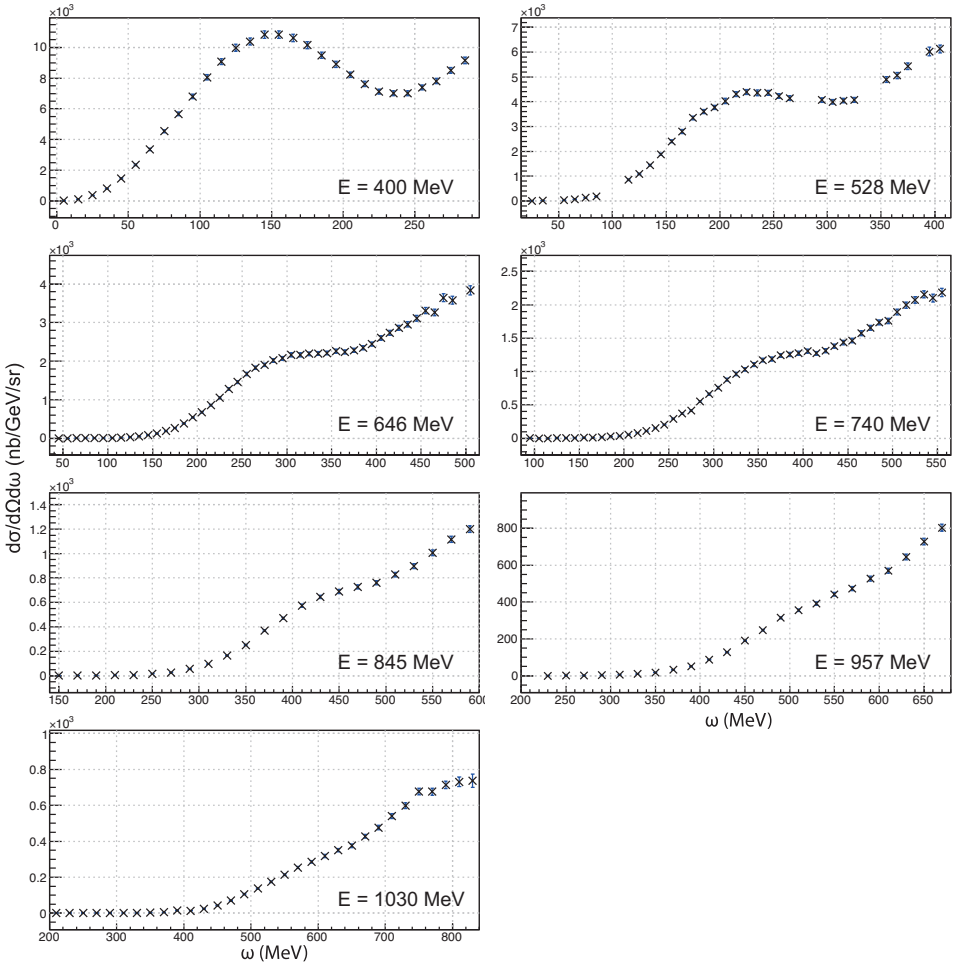

Figure 5.8: Differential cross sections of ^{56}Fe at $\theta = 90°$.

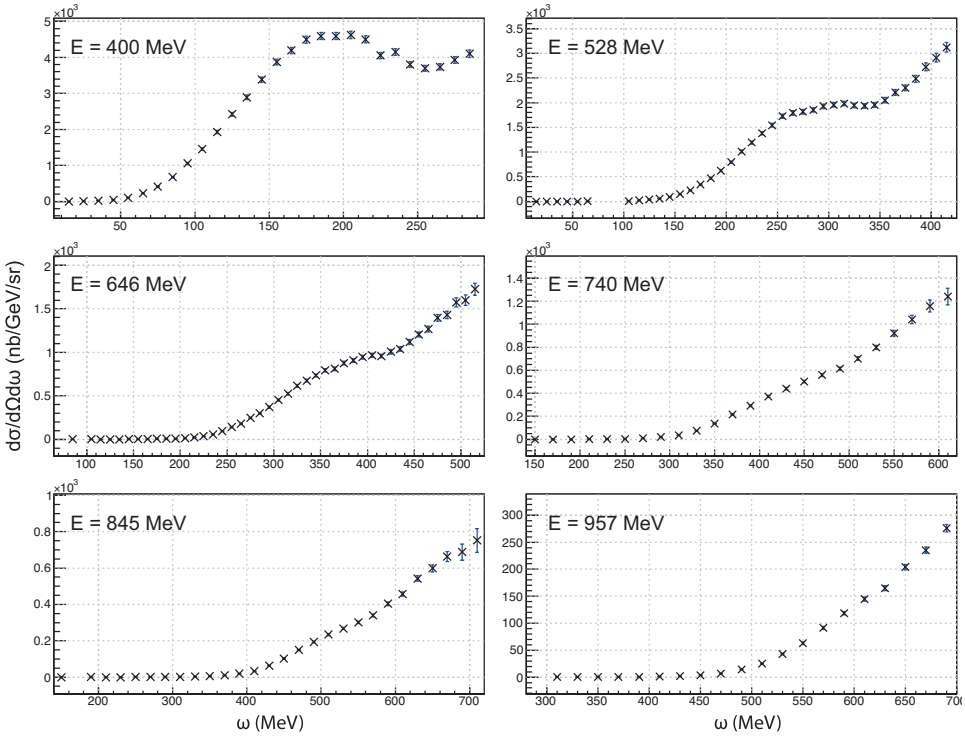

Figure 5.9: Differential cross sections of ^{56}Fe at $\theta = 120°$.

5.2 LT Separation

5.2.1 R_L and R_T

The separated response functions, R_L and R_T, of ^{12}C and ^{56}Fe are shown in Figures 5.10 and 5.11, respectively, followed by preliminary result of ^{4}He in Figure . As $|\mathbf{q}|$ grows, the differences between εR of forward and backward angles become smaller, and therefore the uncertainties of R_L and R_T get larger.

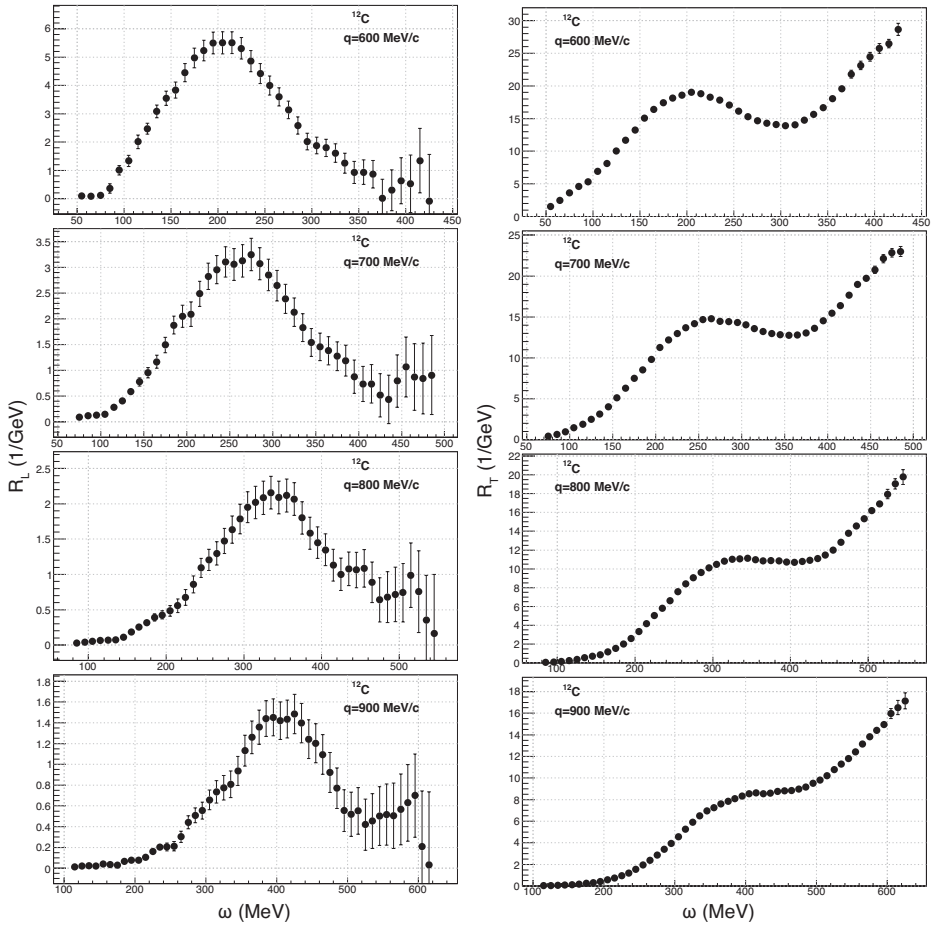

(a) (b)

Figure 5.10: (a) Longitudinal and (b) transverse responses of ^{12}C. Here, $|\mathbf{q}| = |\mathbf{q}_{\text{eff}}|$.

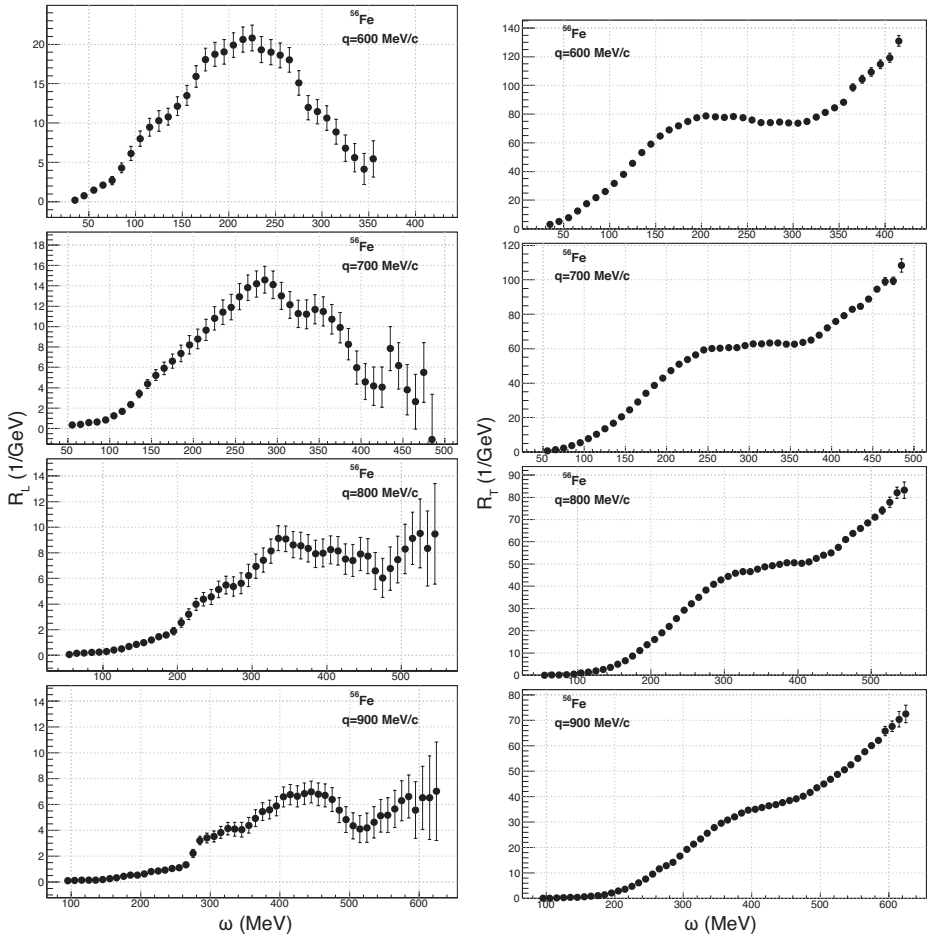

(a) (b)

Figure 5.11: (a) Longitudinal and (b) transverse responses of ^{56}Fe. $|\mathbf{q}|$ means $|\mathbf{q}_{\rm eff}|$.

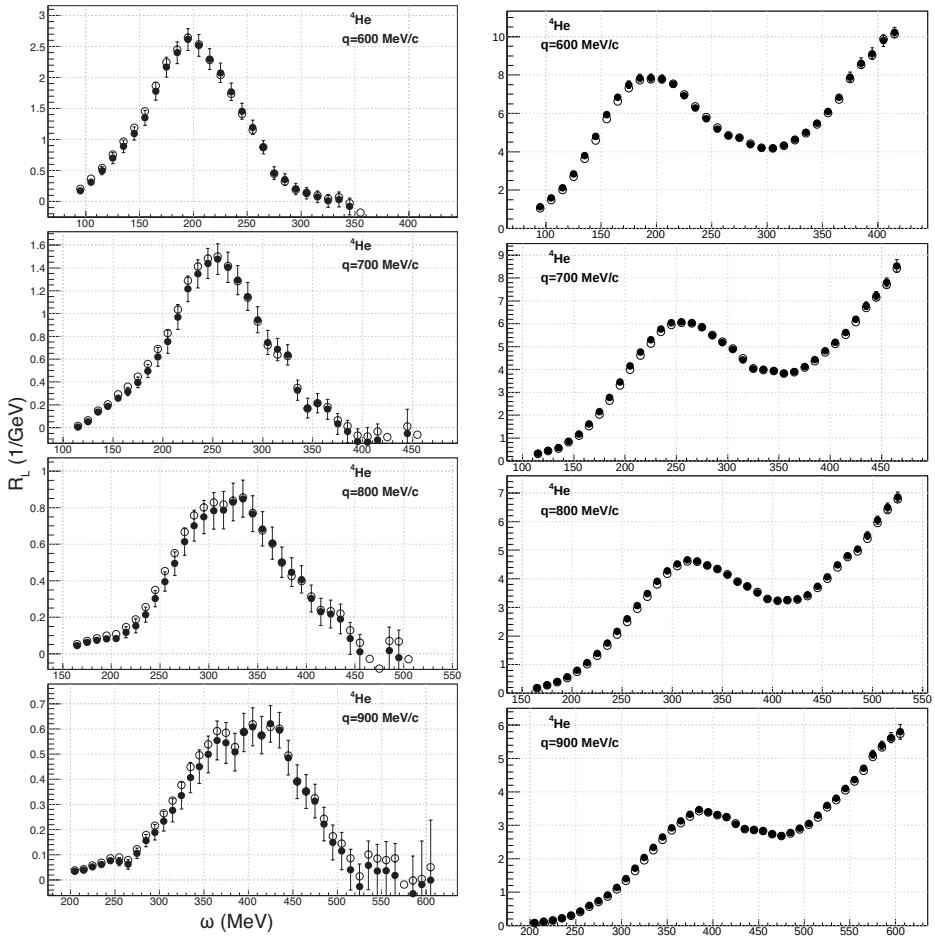

Figure 5.12: (a) Longitudinal and (b) transverse responses of ^{4}He (Preliminary)

5.2.2 Comparison of R_L among Targets

In Figure 5.13, R_L of ^{4}He, ^{12}C and ^{56}Fe are shown again, along with each other. One can directly see the differences in their widths, which represent the internal montion of nucleons inside the nucleus.

At low $|\mathbf{q}|$, all of R_L reach zero, or even go below 0 at high ω. However, while R_L of ^{4}He touches zero at high ω at all $|\mathbf{q}|$ range, R_L of ^{12}C barely touches zero with its large error bar at high $|\mathbf{q}|$. And R_L of ^{56}Fe does not reach 0 at all at high $|\mathbf{q}|$, and shows another rise of some structure. This

feature is quite interesting because SLAC NE9 data [33] showed vanishing of R_L at high ω, at $|\mathbf{q}| = 1.14$ GeV/c, even without the Coulomb correction. And it causes difficulty in calculation of Coulomb Sum which requires R_L up to infinite range of ω.

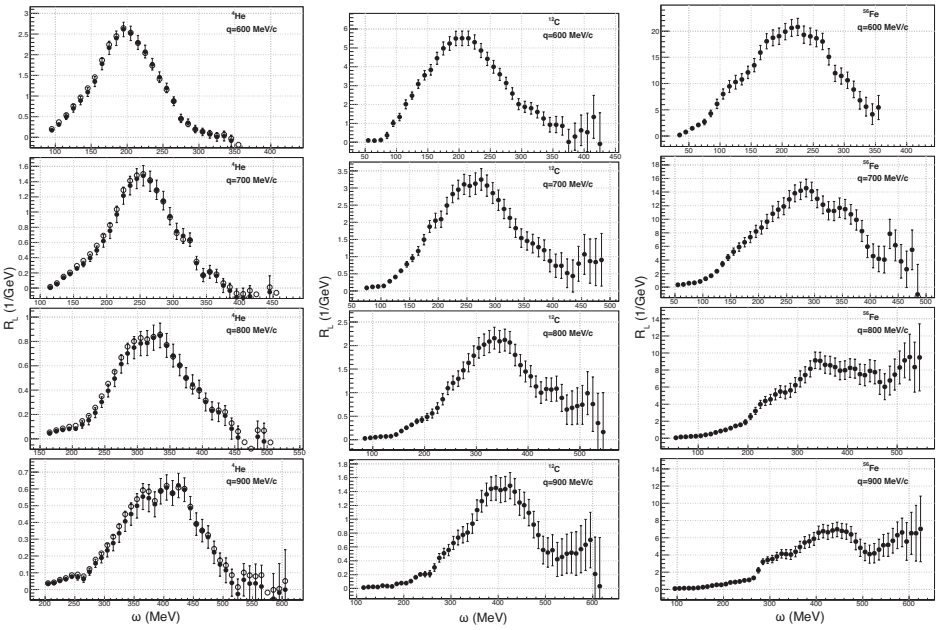

Figure 5.13: R_L of ^{4}He (left, preliminary), ^{12}C (middle), and ^{56}Fe (right).

5.2.3 Comparison with Existing Data

In Figure 5.14, R_L at low $|\mathbf{q}_{\rm eff}|$ for ^{12}C and ^{56}Fe are shown along with existing data from Ref.[34, 31]. For ^{12}C and ^{56}Fe, our data are in agreement with previous ones; the positions and widths of the peaks match, and most error bars are in touch. Although the existing data shown here were not corrected for Coulomb distortion, because the correction would not be so large at this $|\mathbf{q}|$, the agreements would still remain after the correction.

In Figure 5.15, R_L of ^{4}He (preliminary) at $|\mathbf{q}| = 600$ MeV/c and $|\mathbf{q}| = 640$ MeV/c are shown with existing Saclay data [30]. At 600 MeV/c, our data reproduced previous ones but with much smoother shape and with smaller error bars. Small differences are the broader peak top and the bumps at around $\omega = 300$ MeV in Saclay data, which are not observed in ours. They both show R_L drops below zero at $\omega \sim 350$ MeV. At 640 MeV/c, while our R_L is smaller than that of $|\mathbf{q}| = 600$ MeV/c, which is normal behavior,

Saclay data are similar to, or even larger than their 600 MeV/c data. One can imagine that the Coulomb Sum will be different at $|\mathbf{q}| = 640$ MeV/c; i. e., ours will produce smaller S_L. And it can be noted that our spectrum go through ω to quasi-elastic tail, Saclay data end at around $\omega = 300$ MeV, which was their experimental limit.

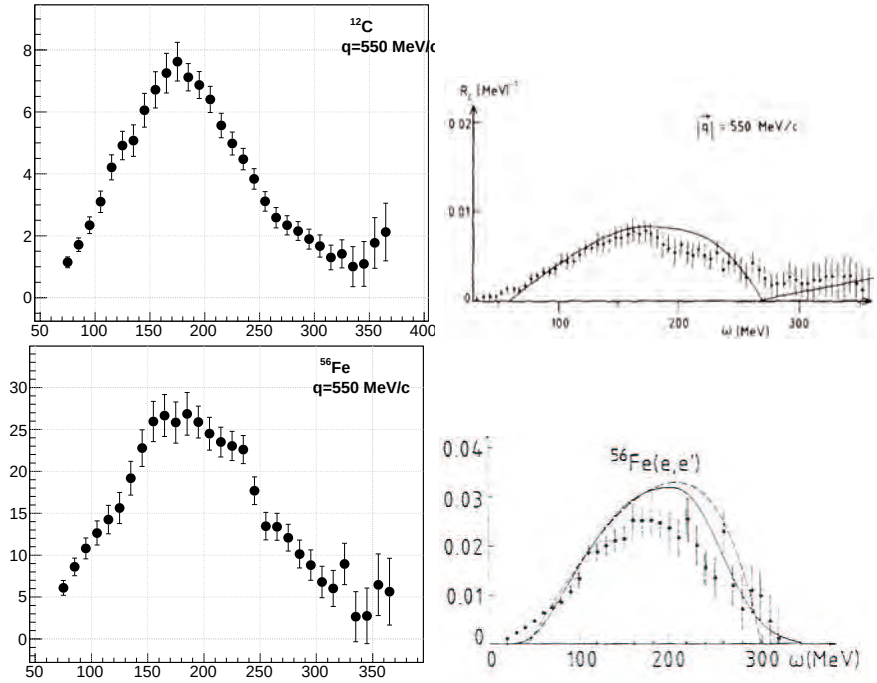

Figure 5.14: R_L of ^{12}C at $|\mathbf{q}| = 550$ MeV/c of this experiment (open circle, top left), and ^{56}Fe at same $|\mathbf{q}|$ (open circle, bottom left), and previous data (their right)[34, 31]. Note that reference data are not corrected for the Coulomb distortion.

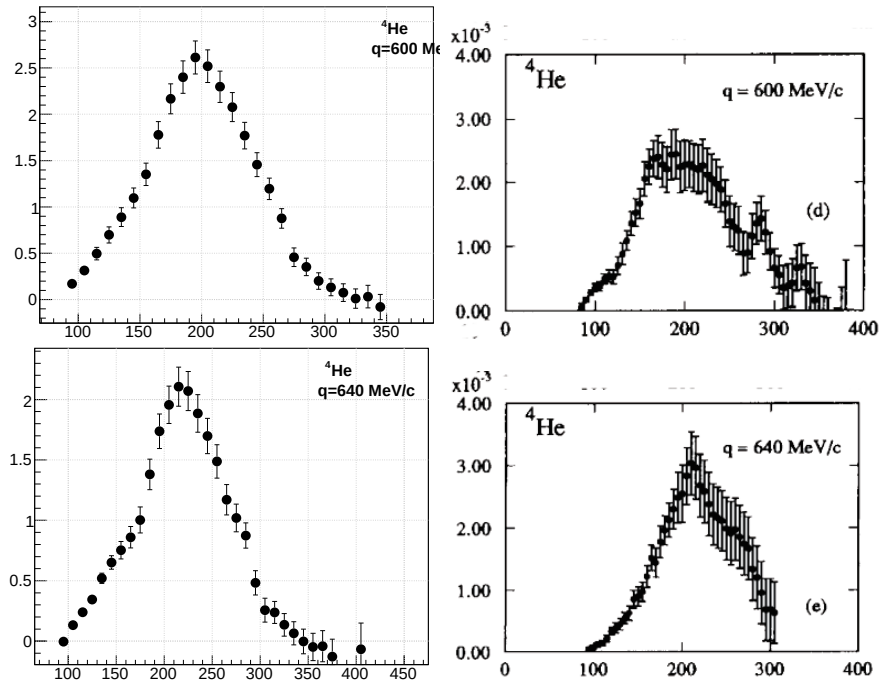

Figure 5.15: Preliminary results of ^{4}He R_L of this experiment (left), and Saclay data (right) [30].

5.3 Coulomb Sum

Coulomb Sum (S_L) defined in Eq. 1.4 requires an integral of R_L over all values of ω. However, it is impossible to measure $\omega > |\mathbf{q}|$ in real experiment. Furthermore, reliable experimental data cannot be obtained near the limit $\omega \sim |\mathbf{q}$ because of the presence of radiative corrections, falling detector efficiencies, and other technical considerations [34]. And due to $\mathbf{q}^4/Q^4$ term during separation of R_L, Coulomb Sum gathers only large useless errors in high ω. A traditional ways to deal with these obstacles is to evaluate the integral up to a limit $\omega_{\max}$. $\omega_{\max}$ can either be the experimental limit or be a theoretical value which is usually calculated from the nuclear spectral functions $S(\mathbf{k}, E)$.

The experimental limit of our ^{12}C data is, by chance, found to be almost same as $\omega_{\max}$ suggested by Barreau [34]. Hence, in this work, $\omega_{\max}$ has been chosen to be the data limit.

For the response functions at a constant $|\mathbf{q}|$, uncertainty of each data

point is not independent from others' because it is produced by interpolation. And as previously mentioned, the statistical and the systematic uncertainties are not separable. Therefore, an error bar of S_L shown here does not represent the quadratic or linear sum of the uncertainties of R_L, but represents the difference between the S_L calculated from the central value and the one calculated from lower (or upper) envelopes of R_L.

For the free proton (neutron) electric form factor in the denominator in Eq. 1.4, Simon [24]'s (Galster [35]'s) parametrizations have been used.

- Simon's proton form factor:

$$G_E^p(Q^2) = \sum_{n=1}^{\infty} \frac{a_n}{1 + Q^2/m_n^2} \tag{5.1}$$

- Galster's neutron electric form factor:

$$G_E^n(Q^2) = -\mu_n \frac{\tau}{1 + 5.6\tau} G_E^p(Q^2) \tag{5.2}$$

The parameters and explanations for them are in the references. The parametrizations have their own uncertainties but they are negligible compared to the uncertainty of R_L. The relativistic correction (ζ) is defined [3]:

$$\zeta = \frac{1 + Q^2/4M^2}{1 + Q^2/2M^2}. \tag{5.3}$$

The correction results in increment of S_L by a few percent at low $|\mathbf{q}|$ ($\sim$600 MeV/c) and by $\sim$10% at high $|\mathbf{q}|$ ($\sim$900 MeV/c).

The resulting experimental Coulomb Sum versus $|\mathbf{q}_{\text{eff}}|$ is shown in Figure 5.16. ^{4}He result, which is preliminary, shows a quenching of more than 30% at the lowest $|\mathbf{q}|$, more quenching than previously observed. This is mainly due to negative values of R_L at high ω, some of which are not shown in the figures.

S_L of all the target do not remain constant but increase with $|\mathbf{q}|$, which is not expected by theory shown in Figure 1.6. Especially for ^{56}Fe, S_L becomes larger than 1 at the highest $|\mathbf{q}|$. At this high $|\mathbf{q}|$, S_L will be much bigger than 1 if one consider that R_L does not vanish at high ω in the experimental limit. For ^{12}C, increment is smaller and S_L remains below 1 at all $|\mathbf{q}|$. And S_L touches unity with its large error bars at the highest $|\mathbf{q}|$. And for ^{4}He, S_L remains almost constant up to around 750 MeV/c, increases after that and it also touches 1 at $|\mathbf{q}| = 950$ MeV/c.

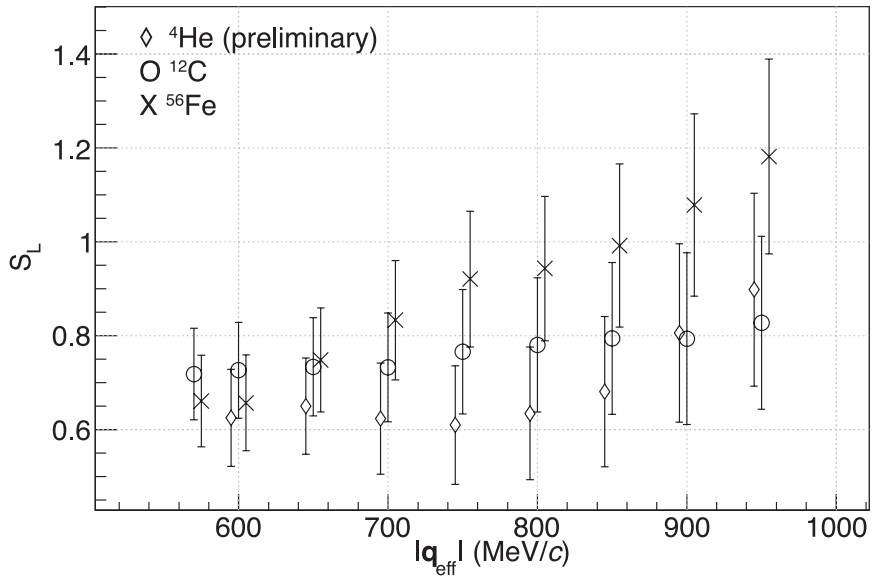

Figure 5.16: Experimental Coulomb Sum of ^{4}He (preliminary), ^{12}C and ^{56}Fe as a function of $|\mathbf{q}_{\rm eff}|$. Note that to avoid confusion, ^{4}He data are shifted by -5 MeV/c, and ^{56}Fe by +5 MeV/c in horizontal axis.

Chapter 6

SUMMARY AND CONCLUSION

Inclusive electron scattering off of ^{12}C and ^{56}Fe nuclei around the quasi-elastic region has been measured. Cross sections at four scattering angles of 15, 60, 90 and 120 degrees, and at incident energies ranging 0.4-3.7 GeV were measured. The scattered electron momenta span a wide range from 0.1 GeV/c to 3.7 GeV/c. Experimental apparatus such as the spectrometer performance, the detecter efficiencies and the target properties have been analyzed. After normalization using the carbon-12 and proton elastic scattering data, and after applying the radiative corrections, the measured cross sections were obtained with better than $\sim$1% statistical and 1-3% systematic uncertainties.

A Rosenbluth separation was performed at 550 MeV/c $\leq |\mathbf{q}_{\rm eff}| \leq$950 MeV/$c$. To separate the longitudinal (R_L) and the transverse (R_T) response functions, interpolation was performed. Because the separation involved a fitting process, the statistical and the systematic uncertainties became no more separable. The separated longitudinal response functions have much larger uncertainties than the cross sections because the longitudinal components are small. The uncertainties of R_L at the quasi-elastic peaks are $\sim$8% at low $|\mathbf{q}_{\rm eff}|$, and $\sim$15% at high $|\mathbf{q}_{\rm eff}|$. The uncertainties of R_T are small, 2-3% at the quasi-elastic peak.

To account for the Coulomb distortion, data were corrected using the Effective Momentum Approximation. At around quasi-elastic peaks, the change from $|\mathbf{q}|$ to $|\mathbf{q}_{\mathbf{eff}}|$ reduced R_L by $\sim$2% at 600 MeV/c, by $\sim$10% at 950 MeV/c for ^{12}C, and by $\sim$10%, $\sim$25% at same momentum transfers for ^{56}Fe. The effect became larger at higher momentum transfer and at around

inelastic peak. Therefore, the Coulomb Sum was affected significantly by the Coulomb correction. The transverse response functions were also corrected but the correction is small compared to the longitudinal part.

In contrast to the previous observation of SLAC NE9, at high $|\mathbf{q}|$ of this experiment, R_L of ^{56}Fe does not vanish at the highest energy loss in the data limit, even after application of the Coulomb correction. Comparison with the result of the other target nuclei ^{4}He and ^{12}C, showed that R_L at high $|\mathbf{q}|$ does not reach 0 as Z (or A) becomes larger.

The experimental Coulomb Sum (S_L) was calculated by integrating R_L up to the data limit of energy loss. Due to the large uncertainties of R_L at high energy transfer, and due to the dependence among uncertainty of each data point, the uncertainty of the Coulomb Sum becomes even larger. The uncertainty of the Coulomb Sum is $\sim$13% at $|\mathbf{q}_{\text{eff}}| = 570$ MeV/c, and $\sim$18% at $|\mathbf{q}_{\text{eff}}| = 950$ MeV/c. With these large uncertainties, S_L of ^{4}He, ^{12}C and ^{56}Fe are all at $\sim$30% below 1 at the lowest $|\mathbf{q}_{\text{eff}}|$. Although the quenching for ^{4}He is larger than the one from existing data, the result is in agreement with existing data with consideration of error bars. But at higher momentum transfer, where there is no existing data to be compared with, S_L does not remain constant but shows different behvior for different nuclei. Especially, S_L of ^{56}Fe reaches and goes higher than 1 as $|\mathbf{q}_{\text{eff}}|$ grows in the data range. And it would increase more at high $|\mathbf{q}_{\text{eff}}|$ if one account for the energy loss (ω) higher than the data limit because R_L does not vanish. S_L of ^{4}He and ^{12}C also grow with $|\mathbf{q}_{\text{eff}}|$ but remain below 1 in the data range, with the error bars touching 1 at the highest $|\mathbf{q}_{\text{eff}}|$. This may imply a roles of other constributions than quasi-elastic process, such as meson exchange current.

More theoretical and experimental study is required to verify the Coulomb Sum Rule. There is still a room to improve the uncertainty from the acceptance, especially for the fluid targets. And analysis of the data from the other spectrometer, HRS-R, will also improve the result. More careful treatment of the dependence among the uncertainties will lead to more precise S_L. And there remains ^{208}Pb data, the analysis of which will help to study the in-medium effect for higher Z or A nucleus. And at the same time, to understand and interprete current result, especially unexpected non-vanishing R_L of higher Z (A) nuclei at high ω and S_L higher than 1 at large $|\mathbf{q}_{\text{eff}}|$, an extensive theoretical approach will be necesssary.

Bibliography

[1] S. Choi, J.-P. Chen, Z.-E. Meziani, Experiment Proposal, PR-05-110, `http://hallaweb.jlab.org`, and the references therein.

[2] O. Benhar, D. Day, I. Sick, Rev. Mod. Phys. 80 (2008) 189

[3] T. de Forest, Jr., Nucl. Phys. A 414 (1984) 347

[4] M. Traini, Nucl. Phys. A 694 (2001) 325 and the references therein.

[5] P. Gueye *et al*, Phys. Rev. C 60 (1999) 044308

[6] Z.-E. Meziani *et al*, Phys. Rev. Lett. 52 (1984) 2130,
Z.-E. Meziani *et al*, Phys. Rev. Lett. 54 (1985) 1233, and the references therein.

[7] J. Morgensten, Z.-E. Meziani, Physics Letters B 515 (2001) 269 and the references therein.

[8] J. Carlson *et al*, Physics Letters B 553 (2003) 191

[9] J. Alcorn *et al*, Nucl. Instr. and Meth. A 522 (2004) 294

[10] Jefferson Lab Experimental Hall A webpage, `http://hallaweb.jlab.org`

[11] ROOT webpage, `http://root.cern.ch`

[12] Marat M. Rvachev, Ph. D. Thesis (2003), Massachusetts Institute of Technology

[13] Solvinon, Patricia H., Ph. D. Thesis (2006), Temple University

[14] X. Yan *et al*, Chinese Physics C, 35 (2011) 488

[15] H. Yao, Ph. D. Thesis (2011) Temple University

[16] X. Yan, private communication

[17] J.-P. Chen, private communication

[18] J. Beringer *et al.* (Particle Data Group), Phys. Rev. D86 (2012) 010001

[19] S. L. Wilson *et al*, Nucl. Instr. and Meth. A 264 (1988) 263

[20] Webpage of Aerospace Specification Metals (ASM) Inc., `http://asm.matweb.com`

[21] L.W. Mo, Y. S. Tsai, Rev. Mod. Phys., 41 (1969) 205
Y. S. Tsai, SLAC-PUB-0848 (1971), Stanford Linear Accelerator Center

[22] S. Stein *et al*, Phys. Rev. D, 12 (1975) 1884

[23] H. de Vries, C. W. de Jager, C. de Vries, At. Data Nucl. Data Tables 36 (1987) 495

[24] G. G. Simon *et al*, Nucl. Phys. A333 (1980) 381

[25] D. R. Yennie, D. G. Ravenshift, R. N. Wilson, Phys. Rev. 95 (1954) 500

[26] K. Slifer's webpage, `http://www.jlab.org/~slifer` (not public)

[27] I. Sick, J. S. McCarthy, Nucl. Phys. A150 (1970) 631

[28] W. Reuter *et al*, Phys. Rev. C 26 (1982) 806

[29] I. Sick, D. Day, J. S. McCarthy, Phys. Rev. Lett. 45 (1980) 871

[30] A. Zghiche *et al*, Nucl. Phys. A572 (1994) 513

[31] Z.-E. Meziani, Ph. D. Thesis (1984), University of Paris, Orsay

[32] O. Benhar *et al*, nucl-ex/0603032

[33] J.-P. Chen, Ph. D. Thesis (1990), University of Virginia

[34] P. Barreau *et al*, Nucl. Phys. A402 (1983) 515

[35] S. Galster *et al*, Nucl. Phys. B32 (1971) 221

[36] Bjorken, James D., Sidney D. Drell, "Relativistic Quantum Mechanics", McGraw Hill, 1964

Appendix A

Rosenbluth Formula

A short derivation of the Rosenbluth formula is given here. [36]

In the plane wave Born approximation, an inclusive unpolarized electron scattering process occurs through the exchange of a single virtual photon as shown in the Feynman diagram in Fig.1.1. Using the Feynman rules, the cross section can be written as[36]:

$$d\sigma = 2Z^2\alpha^2 \frac{d\mathbf{k}_f}{2E_f}\frac{1}{Q^4} W_{\mu\nu}\eta_{\mu\nu}\frac{1}{[(k_i\cdot P_i)^2 - m_e^2M^2]^{1/2}} \tag{A.1}$$

where the leptonic tensor is

$$\eta_{\mu\nu} = -\frac{1}{2}\sum_{s_i}\sum_{s_f} E_iE_f\bar{\mu}(k_i)\gamma_\nu\mu(k_f)\bar{\mu}(k_f)\gamma_\mu\mu(k_i), \tag{A.2}$$

the hadronic tensor is

$$W_{\mu\nu} = \frac{(2\pi)^3\Omega}{Z^2}\bar{\sum_{S_i}}\sum_{S_f} E_t\gamma^{(4)}(P_i - P_f - q)\langle i|J_\nu(0)|f\rangle\langle f|J_\mu(0)|i\rangle, \tag{A.3}$$

m_e is the electron mass, $\mu(k_i)$ and $\mu(k_f)$ are the initial and final electron plane wave functions, and $J_\mu(0)$ is the electromagnetic current operator of the nucleous at the space-time point $x_\mu = 0$. $|i\rangle$, $|f\rangle$ are the initial and final nuclear states, Ω is the normalization volume, E_t is the initial target energy. The average over the initial leptonic spin states, s_i, gives a factor $1/2$ and the average over the initial target spin states, S_i, is indicated by $\bar{\sum}$. the final spin states of the lepton, s_f, are to be summed over, as are the final spin states of the nucleous, S_f.

The leptonic tensor is easily eavaluated as

$$\eta_{\mu\nu} = -\frac{1}{2}\mathrm{Tr}\ \gamma_\mu(m_e - i\gamma\cdot k_i)\gamma_\nu(m_e - i\gamma\cdot k_f) \tag{A.4}$$

Neglecting the electron mass, one obtains:

$$\eta_{\mu\nu} = -\frac{1}{2}\left[(k_1)_\mu(k_2)_\nu + (k_2)_\mu(k_1)_\nu - (k_1\cdot k_2)g_{\mu\nu}\right]. \tag{A.5}$$

The hadronic tensor $W_{\mu\nu}$ is a second order tensor built out of the two independent 4-vectors P and q(where P is P_i and the subscript is omitted for convenience). With the target mass being known, there are only two independent Lorentz scalers, Q^2 and $q\cdot P$. The most general tensor we can make out of P and q, satisfying the parity conservation, is

$$\begin{aligned} W_{\mu\nu} =& W_1(Q^2,\, q\cdot P)g_{\mu\nu} + W_2(Q^2,\, q\cdot P)\frac{P_\mu P_\nu}{M^2} \\ &+ A\frac{q_\mu q_\nu}{M^2} + B\frac{1}{M^2}(P_\mu q_\nu + P_\nu q_\mu) + C\frac{1}{M^2}(P_\mu q_\nu - P_\nu q_\mu). \end{aligned} \tag{A.6}$$

Using current conservation:

$$q_\mu W_{\mu\nu} = W_{\mu\nu}q_\nu = 0, \tag{A.7}$$

the hadronic retains only two independent terms

$$\begin{aligned} W_{\mu\nu} =& W_1(Q^2,\, q\cdot P)\left(g_{\mu\nu} - \frac{q_\mu q_\nu}{Q^2}\right) \\ &+ W_2(Q^2,\, q\cdot P)\frac{1}{M^2}\left(P_\mu - \frac{P\cdot q}{Q^2}q_\mu\right)(P_\nu - \frac{P\cdot q}{Q^2}q_\nu). \end{aligned} \tag{A.8}$$

In the laboratory frame, where $P\cdot q = \omega M$, one then obtain the cross section:

$$\frac{d^2\sigma}{d\Omega d\omega} = \frac{Z^2\sigma_M}{M}\left[W_2(Q^2,\omega) + 2W_1(Q^2,\omega)\tan^2\frac{\theta}{2}\right] \tag{A.9}$$

where W_1 and W_2 are the structure functions of the target nucleus and are related to the longitudinal and transverse response functions:

$$R_T(Q^2,\omega) = \frac{2Z^2}{M}W_1(Q^2,\omega) \tag{A.10}$$

$$R_L(Q^2,\omega) = \frac{Z^2}{M}\left[\left(\frac{|\mathbf{q}|^4}{Q^4}\right)W_2(Q^2,\omega) - \left(\frac{|\mathbf{q}|^2}{Q^2}\right)W_1(Q^2,\omega)\right]. \tag{A.11}$$

One then obtains the Rosenbluth formula (Eq. 1.1).

요약(국문초록)

미국 제퍼슨 연구소에서 실시된 쿨롱 합 법칙 실험 데이터를 분석하였다. 이 실험은 0.4에서 4 기가볼트까지 다양한 에너지로 가속시킨 전자를 정지해 있는 핵에 충돌시킨 후 튀어나오는 전자를 15, 60, 90, 120도의 네 가지 각도에서 측정한 실험이다. 각각의 에너지와 각도별로, 준탄성충돌 영역에 해당하는 데이터를 측정하였다. 이를 통해 이전에는 보지 못했던 3차원 운동량 전이 영역인 0.55에서 0.95 GeV/c 에서의 데이터를 얻을 수 있었다. 이 영역에서의 로젠블러스 분리를 거쳐 얻은 핵의 종횡 반응 함수를 통해, 핵 안에 있는 핵자의 성질이 변하는지를 가늠해볼 수 있는 쿨롱 합 법칙의 성립 여부를 판단할 수 있다. 무거운 핵자에서 나타나는 전자기장 뒤틀림은 유효 운동량 근사 방법을 이용하여 보정하였다. 실험에 이용된 표적 핵들 가운데, 탄소-12와 철-56의 자세한 분석 과정과 결과를 비교 가능한 이전 실험 데이터와 함께 실었다. 실험 결과 가운데 낮은 운동량 전이 영역 부근에서는, 쿨롱 합이 1보다 작아지는, 이른바 쿨롱 합 법칙 위반이 일어날 수 있다는 것을 확인하였다. 이외의 높은 운동량 전이 영역에서의 결과에 대해서는 보다 깊은 연구가 필요하다.

주요어 : 준탄성 충돌, 로젠블러스 분리, 핵의 반응함수, 쿨롱 합 법칙, 제퍼슨 연구소
학　번 : 2007-30114

Acknowledgement

I would like to express my gratitude to the collaborators;
To Doctor Huan Yao and Doctor Xinhu, this work would never have been done without their great preceding devotions.
To Professor Zein-Eddine Meziani and Doctor Jian-Ping Chen, two of the spokespeople of the experiment, for their kind hospitality in Jefferson Lab and for their great advice.
To Doctor Alexandre Camsonne, the Superman of Hall A, for his kind help and advice, and also for his great journey to Seoul for being a member of the review committee.
To Doctor Vincent Sulkosky, for his kind help and advice during and after the experiment.
To Doctor Elaine Schulte, for her great effort on the CSR collaboration.

And I would like to acknowledge all the individuals who worked for this experiment:
Kalyan Allada, Konrad Aniol, John Arrington, Todd Averett, Herat Bandara, Werner Boeglin, Mustafa Canan, Wei Chen, Khem Chirapatpimol, Eugene Chudakov, Evaristo Cisbani, Francesco Cusanno, Raffaele De Leo, Chiranjib Dutta, Cesar Fernandez-Ramirez, Salvatore Frullani, Haiyan Gao, Franco Garibaldi, Ronald Gilman, Oleksandr Glamazdin, Brian Hahn, Ole Hansen, Douglas Higinbotham, Tim Holmstrom, Bitao Hu, Jin Huang, Florian Itard, Liyang Jiang, Xiaodong Jiang, Hoyoung Kang, Joe Katich, Mina Katramatou, Aidan Kelleher, Elena Khrosinkova,Gerfried Kumbartzki, John LeRose, Byungwuek Lee, Xiaomei Li, Richard Lindgren,Nilanga Liyanage, Joaquin Lopez Herraiz, Lagamba Luigi, Alexandre Lukhanin, Maria Martinez Perez, Dustin McNulty, Robert Michaels,Miha Mihovilovic, Joseph Morgenstern, Blaine Norum, Michael Olson,Makis Petratos, Milan Potokar, Xin Qian, Yi Qiang, Arun Saha, Brad Sawatzky, Elaine Schulte,Mitra Shabestari, Simon Sirca, Patricia Solvignon, Nikolaos Sparveris, Ramesh Subedi, Jose Udias, Javier Vignote, Eric Voutier, Youcai Wang, John Watson, Yunxiu Ye, Zhihong Ye,Xiaohui Zhan, Yi Zhang, Xiaochao Zheng, Lingyan Zhu

and

Jefferson Lab Hall-A Collaboration

감사의 글

짧지 않은 대학원 생활을 부끄러운 논문 한 편과 함께 마무리할 수 있게 되기까지 많은 분들의 도움이 있었습니다. 먼저 여러모로 부족한 저를 지금까지 지켜봐주시고 지도해 주신 최선호 교수님께 감사드립니다. 그리고 논문의 심사를 맡아 아낌없는 조언을 해 주신 김형도 교수님, 방형찬 교수님, 사토 교수님께도 감사의 말씀을 올립니다. 제퍼슨 연구소에서 실험할 수 있도록 재정적으로 지원해 준 BK21 사업단과 WCU 사업단에도 감사드립니다.

처음 물리를 하겠다고 마음 먹은 것은 고등학교 3학년 때의 물리 선생님이신 김진우 선생님 덕분이었습니다. 이 자리를 빌어 감사의 말씀 전합니다.

연구 뿐 아니라 대학원 생활 내내 연구실 선배님들과 동료들로부터 크고 작은 조언과 도움을 받았습니다. 임희중 박사님, 이병욱 박사님, 추경호 박사님, 김도균 박사님, 김미정 박사님, 김은희 박사님, 혜구 형, 호영, 정석, 명진, 성배, 융희, 종원, 현우, 한울, 상현 등 모두에게 감사의 마음 전하고 싶습니다. 학부 때부터 함께 한 친구들, 광우, 재성, 호준이와 배규정 박사님에게도 고마움을 전합니다. 특히 컴퓨터와 관련하여 광우에게 많은 도움을 받았습니다.

여러 차례 제퍼슨 연구소에 머무르는 동안 신일경 선배님께 많은 신세를 졌습니다. 박기준 박사님과 이정한 박사님께도 감사드립니다. 미국에서 먼 길을 달려와 맞아준 원열, 하나 부부에게도 고마움을 전합니다.

언제나 힘이 되어 주는 오랜 친구들, 순오, 영찬, 자영, 정윤, 인호, 영수, 승권, 형근에게도 이 자리를 빌어 고마움을 표현하고 싶습니다.

못난 조카를 자랑스러워하시며 물심양면으로 도와주신 작은 아버지와 고모, 친지 분들께도 감사드립니다.

마지막으로 사랑하는 가족들에게 감사의 인사를 전합니다. 철부지 자식 스물다섯 해 동안 학교 보내시느라 고생하신 사랑하는 아버지와 어머니, 일 년 전부터 식구가 된 사랑하는 아내 임유경 님, 부족한 사위를 가까이에서 아껴주시는 장인, 장모님, 타지에서 고생하고 있는 형과 형수님, 선재, 은재 모두 큰 힘이 되어 주었습니다.

두 달 남짓 지나면 마주하게 될 첫아이에게 이 논문을 전합니다.